Project Report
ATC-419

The 2013 Buffalo Area Icing and Radar Study (BAIRS)

E.R. Williams
M.F. Donovan
D.J. Smalley
R.G. Hallowell
E. Griffin
K.T. Hood
B.J. Bennett

6 March 2015

Lincoln Laboratory
MASSACHUSETTS INSTITUTE OF TECHNOLOGY
LEXINGTON, MASSACHUSETTS

Prepared for the Federal Aviation Administration,
Washington, D.C. 20591

TECHNICAL REPORT STANDARD TITLE PAGE

1. Report No.	2. Government Accession No.	3. Recipient's Catalog No.
ATC-419		

4. Title and Subtitle	5. Report Date
The 2013 Buffalo Area Icing and Radar Study (BAIRS)	6 March 2015
	6. Performing Organization Code

7. Author(s)	8. Performing Organization Report No.
E.R. Williams, M.F. Donovan, D.J. Smalley, R.G. Hallowell, E. Griffin, K.T. Hood, and B.J. Bennett, MIT Lincoln Laboratory	ATC-419

9. Performing Organization Name and Address	10. Work Unit No. (TRAIS)
MIT Lincoln Laboratory 244 Wood Street Lexington, MA 02420-9108	11. Contract or Grant No. FA8721-05-C-0002

12. Sponsoring Agency Name and Address	13. Type of Report and Period Covered
Department of Transportation Federal Aviation Administration 800 Independence Ave., S.W. Washington, DC 20591	Project Report
	14. Sponsoring Agency Code

15. Supplementary Notes

This report is based on studies performed at Lincoln Laboratory, a federally funded research and development center operated by Massachusetts Institute of Technology, under Air Force Contract FA8721-05-C-0002.

16. Abstract

The Next Generation Weather Radar (NEXRAD) network completed a dual polarization upgrade in 2013. The radars now can be used to sense the type of scatterers that cause the radar returns. The scatterers can be hydrometeors, biologicals, or earth-sourced. The ability to reliably interpret the radar-sensed thermodynamic phase of the hydrometeors (solid, liquid, mix) in the context of cloud microphysics and precipitation physics makes it possible to assess the icing hazard potential to aviation. That assessment for Federal Aviation Administration (FAA) purposes would necessarily be performed by automated algorithms based in hydrometeor classification terms. The truth as to the icing hazard aloft (where the radar scans) is required to ascertain the value of such algorithms.

The Buffalo Area Icing and Radar Study (BAIRS) of 2013 was a partnership between MIT Lincoln Laboratory (LL) and the National Research Council of Canada (NRC) to perform in situ icing missions within the surveillance range of the dual polarization NEXRAD in Buffalo, NY. The goal of these 2013 missions, and the subject of this report, was to target specific winter weather scenarios known to exhibit an aviation icing hazard for the purpose of quantifying the microphysical properties of the target zones and verifying the presence of supercooled liquid water (SLW) to support validation of hydrometeor classification algorithms. These are the first such missions to execute in situ measurements within a NEXRAD's surveillance range running with the fielded, operational NEXRAD hydrometeor classifier.

NRC's Convair-580 instrumented research plane was used for three icing missions covering 14 hours. Three distinctly different winter weather scenarios were encountered. This document details the analysis of in situ data such as particle type and liquid water content (LWC) with NEXRAD dual polarization parameters for the three missions. The BAIRS analysis identified these key findings:

- NEXRAD radar returns are prevalent in conditions of supercooled water,
- NEXRAD classification shows positive results based on particle imagery,
- NEXRAD 'dry snow' class masks the presence of mixed phase potential icing hazard,
- NEXRAD 'unknown' class contains diverse regions of icing hazard potential, and there are methods to classify some of these regions, and
- In situ aircraft observations are an important tool to both verify algorithm performance and guide further development.

17. Key Words	18. Distribution Statement
	This document is available to the public through the National Technical Information Service, Springfield, VA 22161.

19. Security Classif. (of this report)	20. Security Classif. (of this page)	21. No. of Pages	22. Price
Unclassified	Unclassified	154	

This page intentionally left blank.

ABSTRACT

The Next Generation Weather Radar (NEXRAD) network completed a dual polarization upgrade in 2013. The radars now can be used to sense the type of scatterers that cause the radar returns. The scatterers can be hydrometeors, biologicals, or earth-sourced. The ability to reliably interpret the radar-sensed thermodynamic phase of the hydrometeors (solid, liquid, mix) in the context of cloud microphysics and precipitation physics makes it possible to assess the icing hazard potential to aviation. That assessment for Federal Aviation Administration (FAA) purposes would necessarily be performed by automated algorithms based in hydrometeor classification terms. The truth as to the icing hazard aloft (where the radar scans) is required to ascertain the value of such algorithms.

The Buffalo Area Icing and Radar Study (BAIRS) of 2013 was a partnership between MIT Lincoln Laboratory (LL) and the National Research Council of Canada (NRC) to perform in situ icing missions within the surveillance range of the dual polarization NEXRAD in Buffalo, NY. The goal of these 2013 missions, and the subject of this report, was to target specific winter weather scenarios known to exhibit an aviation icing hazard for the purpose of quantifying the microphysical properties of the target zones and verifying the presence of supercooled liquid water (SLW) to support validation of hydrometeor classification algorithms. These are the first such missions to execute in situ measurements within a NEXRAD's surveillance range running with the fielded, operational NEXRAD hydrometeor classifier.

NRC's Convair-580 instrumented research plane was used for three icing missions covering 14 hours. Three distinctly different winter weather scenarios were encountered. This document details the analysis of in situ data such as particle type and liquid water content (LWC) with NEXRAD dual polarization parameters for the three missions. The BAIRS analysis identified these key findings:

- NEXRAD radar returns are prevalent in conditions of supercooled water,
- NEXRAD classification shows positive results based on particle imagery,
- NEXRAD 'dry snow' class masks the presence of mixed phase potential icing hazard,
- NEXRAD 'unknown' class contains diverse regions of icing hazard potential, and there are methods to classify some of these regions, and
- In situ aircraft observations are an important tool to both verify algorithm performance and guide further development.

This page intentionally left blank.

ACKNOWLEDGMENTS

This study would not have been possible without the full cooperation of the National Research Council of Canada Convair staff (pilots, navigator, instruments people, flight crew) in the coordination of all aspects that led to the three successful missions. Of particular importance here are the chief scientists for all missions, Dr.'s Mengistu Wolde and Alexei Korolev. They have provided key assistance and discussion in working through the massive data sets that accumulate on every flight, and with the physical interpretation of the observations.

MIT Lincoln Laboratory also thanks Tim Crum (NOAA ROC) who facilitated the arrangements for radar and air traffic operations requests with Bob LaPlante (WFO Cleveland), David Zaff (WFO Buffalo), Mark McKinley (ARTCC Oberlin, OH), and Jeff Waldsteicher (Eastern Region Headquarters, NWS). Their responsiveness to LL radar operation requests particularly was critical to the icing missions.

We are also indebted to Thomas Webster at the Federal Aviation Administration (FAA) for alerting the authorship of this report to the icing incident in Madison, Wisconsin, whose analysis is now part of the document. This led to direct communication with Dan Spangler and Grant Goetsch, who provided critical information to the analysis in this report.

Final acknowledgment goes to Steve Kim at the FAA who was able to support the icing missions understanding the merit of and need for in situ measurements to verify and validate.

This page intentionally left blank.

TABLE OF CONTENTS

TABLE OF CONTENTS
(Continued)

LIST OF ILLUSTRATIONS

LIST OF ILLUSTRATIONS
(Continued)

LIST OF ILLUSTRATIONS
(Continued)

LIST OF ILLUSTRATIONS
(Continued)

LIST OF ILLUSTRATIONS
(Continued)

LIST OF ILLUSTRATIONS
(Continued)

LIST OF ILLUSTRATIONS
(Continued)

LIST OF ILLUSTRATIONS
(Continued)

LIST OF ILLUSTRATIONS
(Continued)

LIST OF ILLUSTRATIONS
(Continued)

LIST OF TABLES

This page intentionally left blank.

1. INTRODUCTION

1.1 GENERAL GOALS

The Federal Aviation Administration (FAA), as a triagency member, provided for the dual polarization upgrade of the U.S. Next Generation Weather Radar (NEXRAD) network. Products from the network are used by multiple FAA weather systems. The so-called dual pol upgrade adds the capability to sense the type of scatterers that cause the radar returns. The scatterers can be in liquid or solid water form (hydrometeors), as well as biological (birds, insects) or earth-sourced (dust, field/land debris). With a focus on the detection of water substance, the dual pol capability has the potential to reveal the radar-detectable portion of an icing hazard that would benefit the FAA. The veracity of any dual pol-based NEXRAD hydrometeor classifier or icing hazard algorithm is determined from a truth measurement. For these algorithms, there is no substitute for in situ measurements to verify the presence of supercooled liquid water (SLW) that provides a means to validate the merits of hydrometeor classification and icing hazard identification.

Despite the presence of a clear seasonal variation in icing pilot reports (PIREP) for the continental United States (CONUS) with maximum in winter months, winter storms have received far less radar/aircraft study than summertime convection. However, important work on this problem has been published by Hudak et al., (2002), Plummer et al., (2010), Kennedy and Rutledge, (2011), Ryzhkov et al., (2011), Hubbert et al., (2012), Bechini et al., (2013), and Thompson et al., (2014), among others.

MIT Lincoln Laboratory (LL) first partnered with the National Research Council of Canada (NRC) in February 2012 to perform in situ icing missions within range of the Cleveland, OH, dual pol NEXRAD. This first mission demonstrated the ability to use dual pol NEXRAD radar returns to guide the flight track of an icing mission to explore specific regions of a winter storm system and quantify the microphysical properties for interpretation of the correct hydrometeor classification (ice crystals in this instance). The LL-NRC partnership was renewed for a much more ambitious set of three, radar-directed in situ icing missions performed in February 2013 within range of the Buffalo, NY, dual pol NEXRAD (KBUF). The goal of these 2013 missions, and the subject of this report, was to target missions to specific winter weather scenarios known to exhibit an aviation icing hazard for the purposes of quantifying the microphysical properties of the target zones as a basis for the verification of the presence of SLW that would support validation of hydrometeor classification algorithms.

1.2 NEXRAD DUAL POL CAPABILITY AND HCA CLASSIFICATION

The dual polarization NEXRADs generate three new parameters pertaining to the type of scatterers sensed. These parameters are based in the differing returns off scatterers from the simultaneous transmission of orthogonal horizontal (H) and vertical (V) beams essentially in response to the ratio of the major/minor axes of scatterers. Differential reflectivity (ZDR) is a measure of the reflectivity response

from the H and V transmission. ZDR is zero for equal major/minor axes, negative when the major axis is vertical, and positive when the major axis is horizontal. Cross-correlation coefficient (CC) is the second new dual pol parameter. It is a measure within a pulse resolution volume of how dissimilar a set of scatterers are – the more uniform, the closer to 1. The third parameter is the specific differential phase shift (KDP). It is a measure of how many water scatterers are encountered with more shift evident in heavier precipitation. The response of specific differential phase shift for frozen water scatterers is lesser in magnitude. These three parameters form the basis for the fuzzy logic used in the NEXRAD Hydrometeor Classification Algorithm (HCA) (Park et al., 2009) that separates the identification of the hydrometeors from the biological and the earth-based scatterers. HCA is introduced further in Section 2.

For the interested reader, this document is divided into sections to report on the BAIRS analysis and findings. Section 2 (and companion material in the Appendices) provides general background context pertinent to further discussions in the report. Section 3 continues with information about the NRC Convair-580 instruments and the flight procedures used for the icing missions. Section 4 describes aligning the Convair instrument data with the concurrent NEXRAD data. Section 5 discusses general findings. Section 6 documents in detail the three icing missions. Section 7 provides a comprehensive discussion relating specific findings to the icing hazard concern. Section 8 is focused on the main conclusions. The report concludes with a discussion of future work and recommendations in Section 9.

2. GENERAL CONSIDERATIONS AND BACKGROUND INFORMATION

2.1 DUAL POL MEASUREMENTS TO IDENTIFY PARTICLE TYPES IN WINTER STORMS

The main promise of dual pol capability in winter storms pertains to hydrometeor shape, with secondary importance from water phase (liquid versus solid). Ice microphysics, modulated by cloud condensation nuclei and ice nuclei, provides an amazing variety of hydrometeor shapes that depart measurably from spherical symmetry. For this reason, the main focus in this report is on differential reflectivity, which is linked directly with geometrical asymmetry and consequent backscattering anisotropy. The preferential orientation of the hydrometeor in the gravity field is vital to the dual pol response. The main hydrometeors and their microphysical origins are described briefly below, in order of decreasing anisotropy (directional dependence).

2.1.1 Pristine Vapor Grown Ice Crystals

For reasons still not understood, ice crystals tend to grow preferentially along certain axes of the ice lattice (Hobbs, 1974), and those directions are empirically dependent on humidity and temperature. That tendency leads to marked departures from spherical symmetry. The strongest asymmetries are associated with the hexagonal flat plate (HFP) crystals which can show NEXRAD-maximum ZDR values of +8 dB.

2.1.2 Supercooled Raindrops

Oblate raindrops are the most widely recognized anisotropic hydrometeor to dual pol radar (Seliga and Bringi, 1976). The ZDR (Differential Reflectivity) values from the largest flattened raindrops can reach values of +6 to +7 dB.

2.1.3 Aggregated Snow

Individual ice crystals can join in collisional encounters to form larger aggregates — otherwise known as snowflakes. This process is often dominated by dendritic crystals whose delicate branches can interlock in the aggregation process and which are often the largest crystals in mixed phase conditions because they are the fastest growing ones. Temperatures closer to 0° C are more favorable for aggregation, and the most organized aggregation occurs in the melting layer in stratiform conditions. Large snowflakes can attain diameters of several centimeters and exhibit enhanced oblateness in non-turbulent conditions. Large snowflakes may also show positive differential reflectivity as large as +1 dB, but in general, aggregation of crystals causes a large dilution of anisotropy in comparison to that present with the pristine crystals that formed the aggregate.

2.1.4 Graupel

This hydrometeor, the product of the accretion of SLW, is more prevalent in air mass convection in summertime conditions than in winter snowstorms. Quasi-spherical 'lump' graupel appears in the more strongly convective snowstorm episodes and is often identified in the 'spheres' category in the SNDI algorithm (see Section 3.1.5). Theoretical calculations in Evaristo et al. (2013) show that negative values of ZDR can be produced for conical graupel if the apex angle of the graupel 'cone' top is sufficiently small. NEXRAD measurements in New England (Evaristo et al.) show values of ZDR distributed around 0 dB, in marked contrast to oblate raindrops with similar reflectivity values.

2.1.5 Freezing Drops

Alexander Ryzhkov and his colleagues have studied the behavior of rain drops falling into a sub-freezing layer (classical regime) (Kumjian et al., 2013). LL has found examples of freezing rain in one of the BAIRS winter storm flights.

2.1.6 Supercooled Drizzle

This hydrometeor with droplet diameters in the range of a few hundred microns is expected to conform closely to isotropic scattering more than any other natural shape. Indeed, if the location of supercooled drizzle in the atmosphere were well known, these targets would be well-suited for use in calibration of NEXRAD differential reflectivity.

2.2 ICE CRYSTAL SHAPES VERSUS HUMIDITY AND TEMPERATURE

The anisotropy of hydrometeors can be an important distinguishing characteristic for the ice phase. Anisotropy is particularly important in winter storms in which large liquid drops (i.e., raindrops) are often absent and so this distinguishing dual pol characteristic of the liquid phase (Seliga and Bringi, 1976) is lost. Common crystal shapes in winter storms include needles (columns), dendrites, and HFP crystals. Such crystals can grow by water vapor diffusion from microns to millimeters and serve as the predominant radar targets in many situations. In the absence of strong electric fields, all of these shapes align with their long dimensions perpendicular to gravity. Calculations of their differential reflectivity can be accurately handled with analytic results for prolate/oblate ellipsoidal shapes (Hogan et al., 2002), as shown in Figure 2-1.

Beginning with Williams et al. (2011), reliance has been made on laboratory diffusion chamber measurements to define the thermodynamic conditions linked with specific crystal habits, and to use this information in interpreting dual pol radar measurements in snowstorms (Kennedy and Rutledge, 2011), as well as warm season stratiform systems (Williams et al., 2014). The large ZDR values associated with crystals set them apart from the much more isotropic response of 'irregular' ice particles that often dominates in the 'Dry Snow' category of HCA, as will be shown in the analysis of the February 19, 2013 storm in this study (Section 6.1). The value of the laboratory measurements is that the humidity and

temperature parameters can be very stringently controlled, far more precisely than they can be measured within a snowstorm, and fortuitously distinct crystal shapes are linked with specific temperature-humidity regimes. One of the best illustrations of this claim is found in the pictorial results of Bailey and Hallett (2009), shown in Figure 2-2. A conspicuous feature of this figure is the presence of dendrites and needles, and to a lesser extent, HFP crystals in a water-super-saturated condition (to the upper right of the red curve). The interesting implication is that these crystals should coexist with supercooled water, in which case their radar signature will serve as an important fingerprint for icing conditions. Similar ideas have appeared before (e.g., Field et al., 2004). This interpretation is also behind the +ZDR 'bright band' of Category A conditions in Williams et al. (2014) in which supercooled water is linked with a highly prevalent ring feature in radar PPI (Plan Position Indicator) scans in winter storms in which gentle warm frontal lifting on a synoptic scale is promoting the growth of dendritic crystals in a temperature range (-10^{o} to -15^{o} C) where they are also prevalent in Figure 2-2.

One puzzlement with the assertion that supercooled liquid water (SLW) is linked with crystal shapes is that often one has the impression that crystals are pristine and unrimed. This was an important reason for developing optical methods in our ground-based studies to distinguish rimed from unrimed particles (see Section A.3). Generally speaking, the Particle Measuring System (PMS) for crystal particle imagery described in Section 3.1.2 is not sufficiently resolved to establish rimed crystals, though in the case of the hexagonal flat plates, sometimes the existence of rime can be discerned. Still another reason for lack of riming may be the smallness of the surrounding cloud droplets that prevent their collisional contact with the larger crystals. It is also possible for dendritic crystals to form near the base of a layer of SLW and then descend into the clear air beneath to escape any riming. Evidence for this behavior was found in an early flight with the Convair-580 over Lake Erie in February 2012.

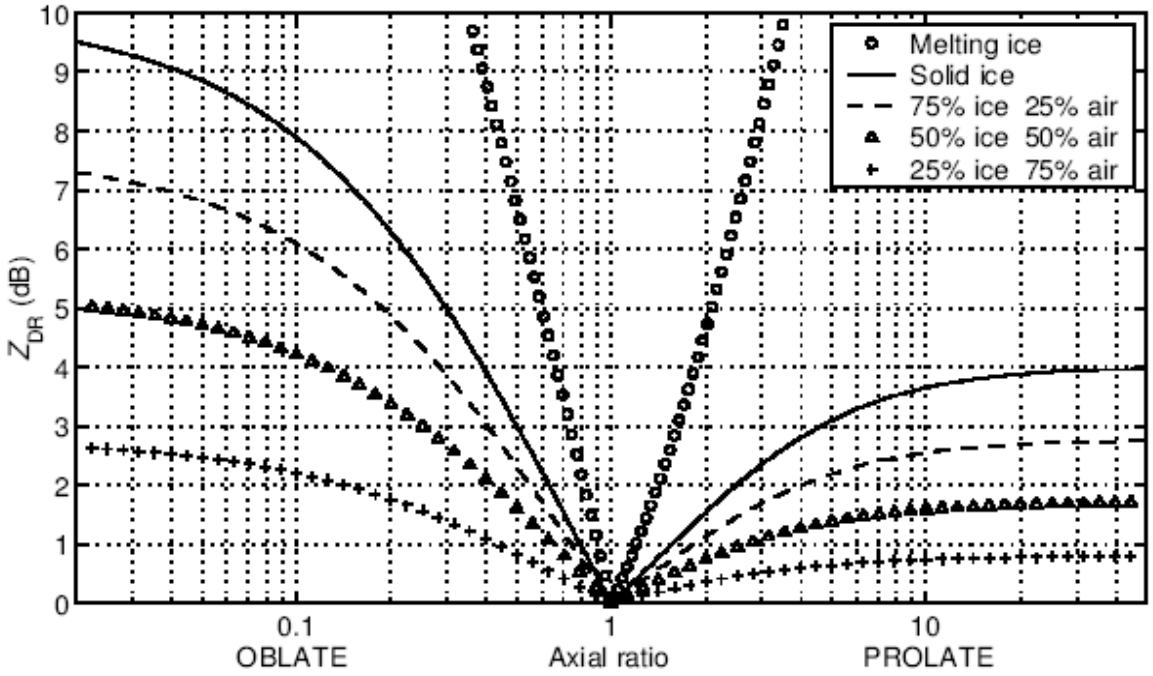

Figure 2-1. Calculations for radar differential reflectivity for needles (prolate ellipsoids) and for dendrites and hexagonal flat plates (oblate ellipsoids), following Hogan et al. (2002). The most anisotropic hydrometeor target to dual pol radar is the hexagonal flat plate crystal, here reaching values of +9 dB.

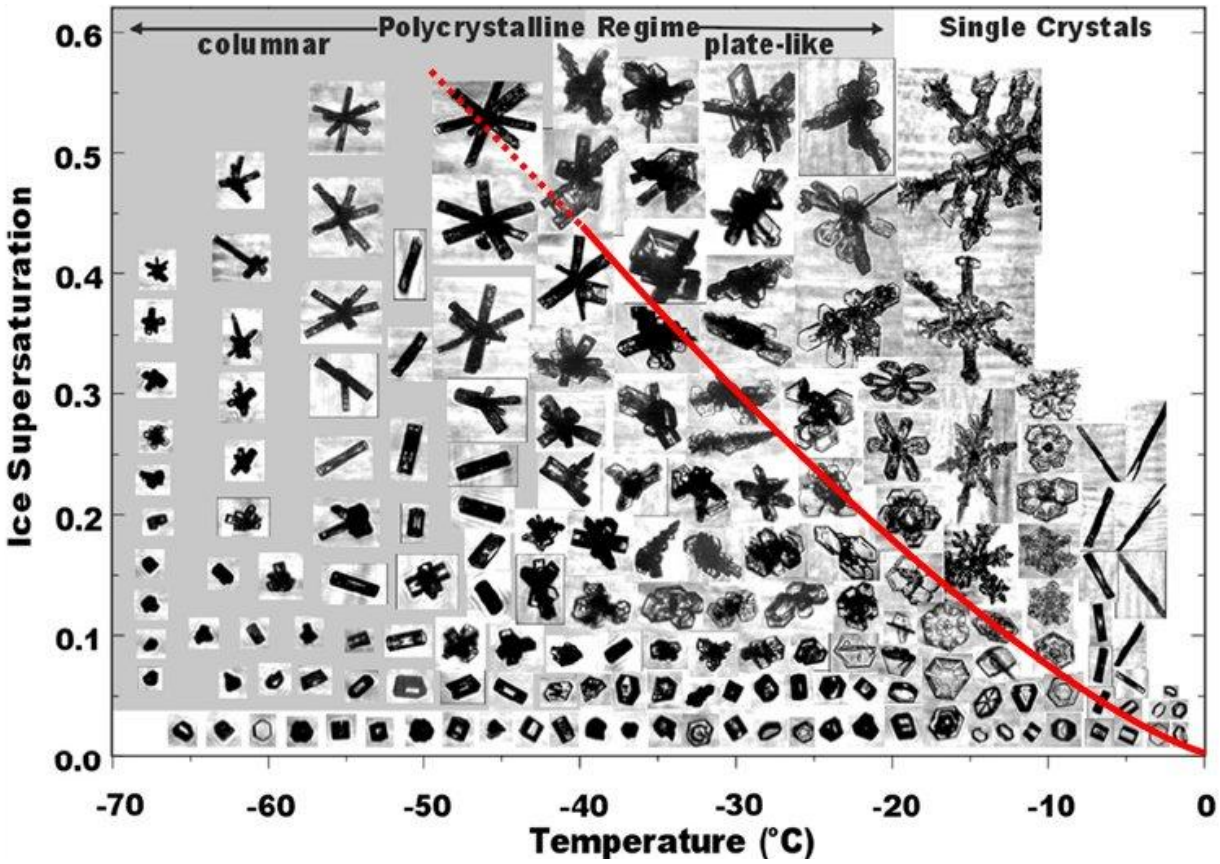

Figure 2-2. Ice crystal habits in the dual parameter space of humidity and temperature. The red boundary defines the water-saturation condition. Dendritic, needle, and (to a lesser extent) hexagonal flat plate shapes are all evident above water saturation.

2.3 NEXRAD HYDROMETEOR CLASSIFICATION ALGORITHM OVERVIEW

The NEXRAD HCA utilizes dual pol radar parameters and melting layer information gathered from radar bright band measurement and numerical weather prediction models to classify the types of liquid or frozen particles at each range and azimuth of the radar beam. The current NEXRAD HCA (Park et al., 2009) classifies the particles found in a particular range-azimuth bin into one of 12 categories. Those categories are listed and described in Table 2-1.

TABLE 2-1

HCA Category Names and Descriptions

Type	Category	ID	Description
Liquid	Heavy Rain	HR	Heavy rain (0.3 mm/hr)
	Big Drops	BD	Large drops of rain (large enough to elongate the drop)
	Light/Mod Rain	RA	Light to moderate rain (0.1–0.29 mm/hr)
Frozen	Rain and Hail	RH	Hail (spheres of ice) of all sizes (a secondary algorithm classifies hail size) possibly mixed with rain
	Wet Snow	WS	Snow that is very dense with liquid
	Graupel	GR	Ice-covered snow particles formed from instantaneous freezing on the snow of SLW droplets encountered
	Dry Snow	DS	Ice crystal aggregates (snowflakes) with irregular shapes
	Ice Crystals	IC	Individual ice crystals shaped as plates, dendrites, or needles
Unknown	No Echo	NE	Radar measurements are below signal-to-noise thresholds*
	Unknown	UK	The algorithm was unable to find an alternative category that had sufficient confidence levels
Clutter	Ground Clutter	GC	Radar beam intersected the ground or objects at the ground (mountains, bridges, trees, wind turbines, etc.)
	Biological	BI	Birds, bats, insects, etc.

* 'No Echo' does not mean that very small ice particles or water droplets (such as SLW) do not exist in this region, but merely that the weak back-scattering from particles is below the radar's sensitivity.

The categorization is restricted based on the relative location of the radar bin to the estimated melting layer (well above the melting layer only frozen categories are allowed, well below only liquids, with a range in between). Figure 2-3 illustrates the allowed HCA categories (in green) for the current HCA. While this restriction is physically based, it is also a way for the algorithm to limit the potential for choosing an unlikely, but possible, category. For example, light/moderate rain is not allowed within or above the melting layer, yet an area of intense SLW might be present in this region. Unfortunately, the radar parameters used for weighting the various categories do not adequately discriminate between SLW and frozen categories.

The strength of the HCA is that it is relatively robust at detecting uniform classes of precipitation in non-complex situations. A weakness is that it was primarily derived for quantifying precipitation by radar

during the warm, convective season. Therefore, it is not necessarily optimized for winter weather complexities. The icing missions to be discussed in this report will describe in detail situations that document the non-optimized nature of some of the HCA frozen type categories and potential paths to improvement.

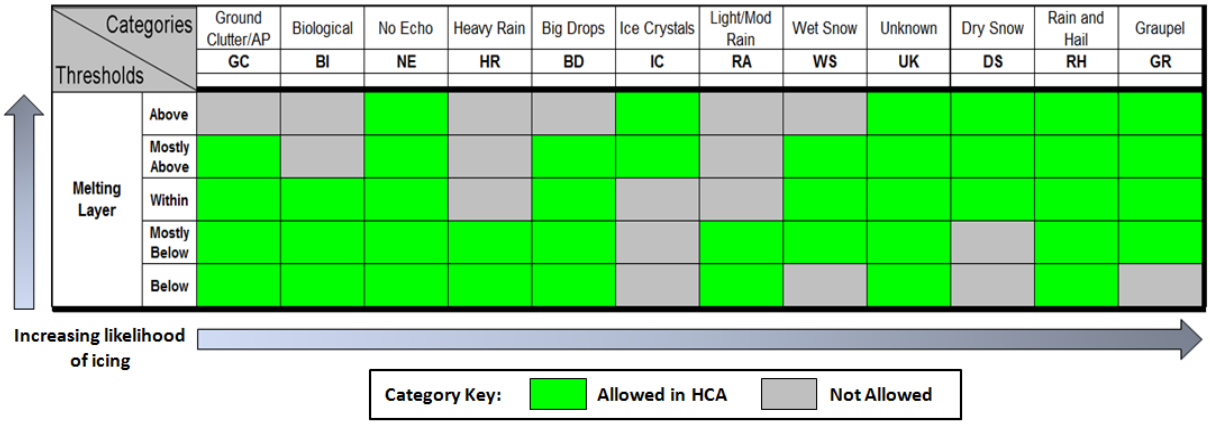

Figure 2-3. Enabled categories within the NEXRAD HCA based on position relative to the melting level.

2.4 LAYERS OF SUPERCOOLED WATER BY ADIABATIC LIFTING

Supercooled water in laterally extensive layers within the atmosphere is widely recognized, and is one dominant morphology for aircraft icing hazard. Quantitative predictions on supercooled water concentration (SLC) in such layers can be obtained by an assumed adiabatic ascent of air from the 0° C level of the atmosphere. If a parcel is assumed saturated with water vapor at 0° C and is then raised moist adiabatically to some new height, and the air is free of ice nuclei, the supercooled water condensate (cloud) is just the difference between the saturation water vapor concentration at 0° C and at the new (colder) altitude. The greater the vertical displacement, the thicker the supercooled layer will be, and the greater will be the SLC. The quantitative results are shown in Figure 2-4, where the adiabatic SLC in g/m^3 (the same units used for the Convair aircraft measurements with the Nevzorov probe) is plotted as a function of the vertical displacement, or cloud layer thickness. Because of interest in a wide dynamic range in both SLC and cloud layer thickness, a log-log plot is used, but it can be seen that the SLC is roughly linear with the layer thickness. Also included on this plot are the icing severity levels currently employed in aircraft PIREPs. These levels are documented in Table A-1. The SLC is less than 0.1 g/m^3 for layer thicknesses less than 50 meters, all in the least severe category 1 icing. Layer thicknesses up to about 300 meters are needed to account for the full range of SLC values obtained in the Convair flights during winter 2013, and this range spans icing categories 2 to 6 and SLC values up to about 0.5 g/m^3. Deeper ascent is needed for SLCs in the two severe categories 7 and 8. For ascents in the kilometer range

and higher, one departs from the winter storm scenario and enters the thunderstorm category for which SLC values as large as several g/m^3 are possible. No values this large were encountered in any of the flights into winter storms.

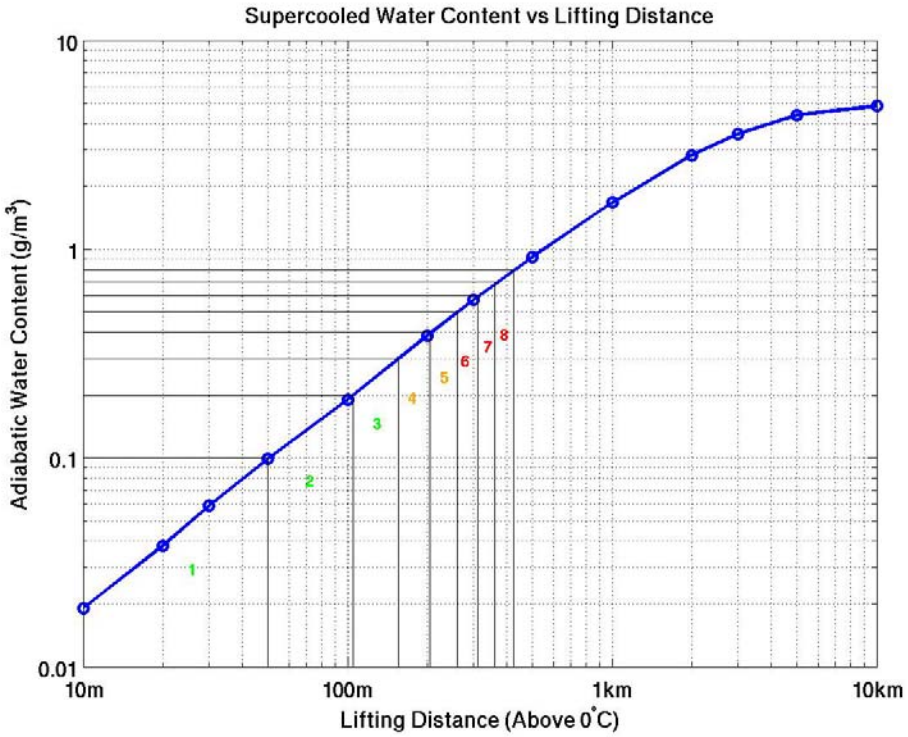

Figure 2-4. Supercooled cloud water content (g/m^3) versus the vertical displacement from (assumed) 0° C level. The calculations are based on the standard Clausius-Clapeyron relation, as quantified in the Smithsonian Meteorological Tables. The icing severity levels (1–8) in PIREPS are also shown.

2.5 DOCUMENTATION OF SUPERCOOLED CLOUD LAYERS IN THREE FLIGHTS OF THE CONVAIR

The adoption of a 'porpoising' strategy in the control of the Convair, in which uniform increases in altitude are alternated with uniform decreases in altitude along an otherwise straight flight path, enabled the documentation of laterally extensive layers of supercooled water with both the Nevzorov and the King hot wire probes. One example of the history of the supercooled water as the plane changed from low to high altitude is shown in Figure 2-5, showing excellent agreement between the two probes. The shape of the liquid water profile is qualitatively consistent with a steady increase of cloud water content from the bottom to the top of the layer, with a rather abrupt decrease near the top.

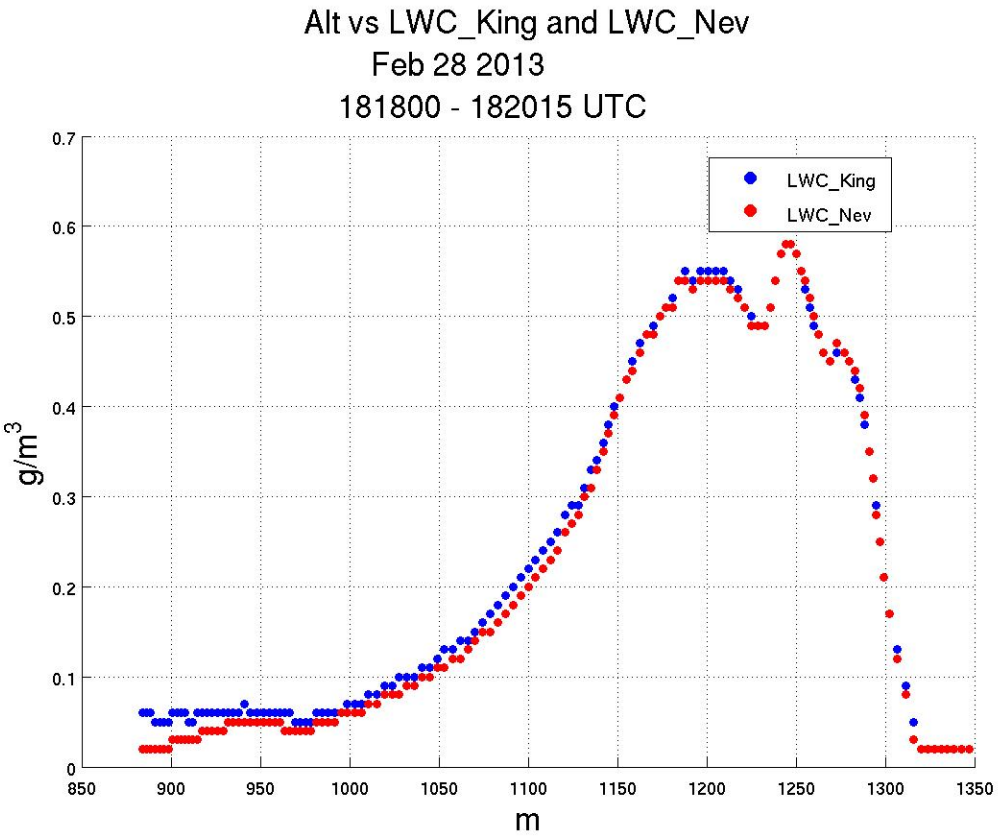

Figure 2-5. Example of supercooled layer in aircraft observation on February 28, 2013.

All aircraft traverses of significant supercooled layers for all three flights have been collected and examined for the maximum value of supercooled water content, and then paired with the measured thickness of the layer in question. All these pairs of points were then plotted against the earlier adiabatic predictions (Figure 2-4) in a new Figure 2-6. These results show that the great majority of measured water contents are sub-adiabatic. Since these layers have been shown to be laterally extensive by virtue of the porpoising evidence, it is not likely that entrainment of drier environmental air is responsible for the sub-adiabaticity. A more likely explanation is that condensate is lost from the layer by precipitation formation and descent. This explanation is consistent with the existence of detectable radar echo from many of these supercooled cloud layers.

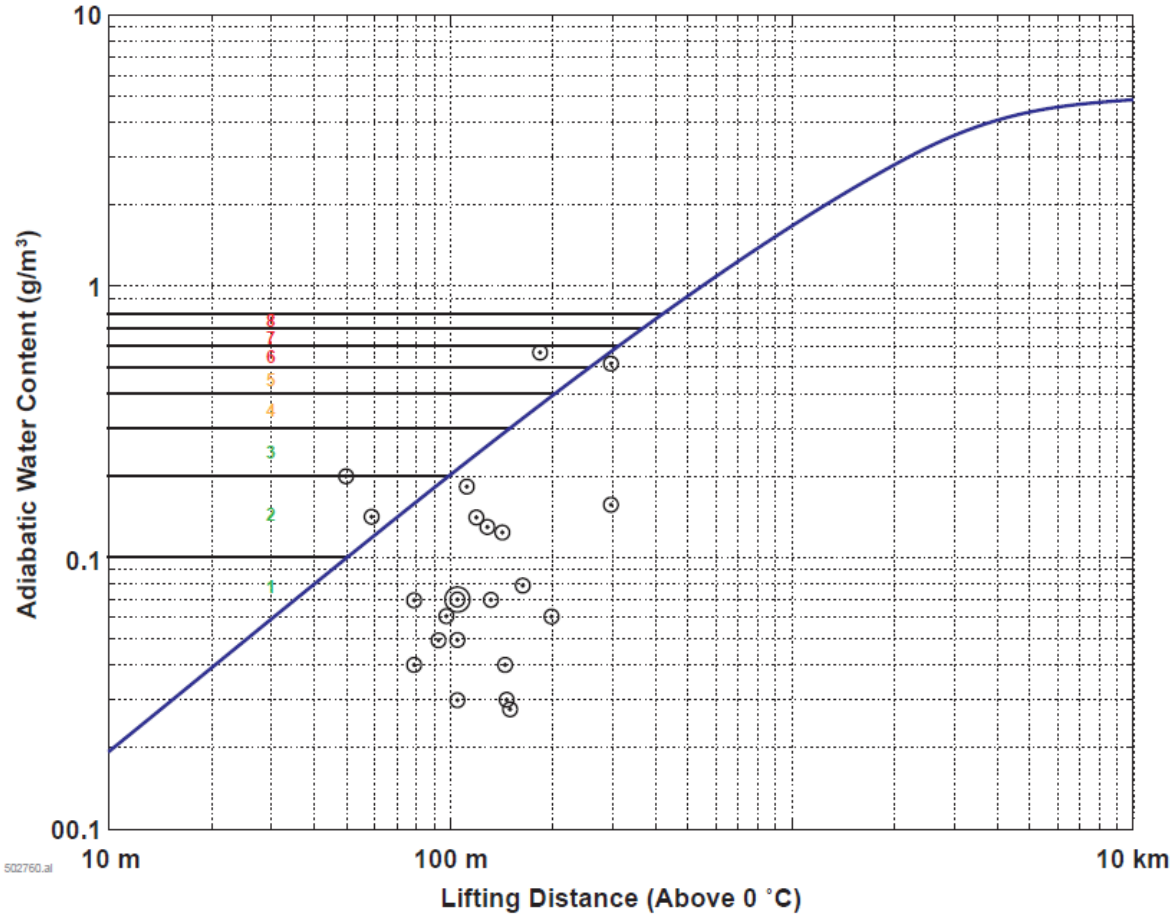

Figure 2-6. Maximum supercooled water contents in g/m^3 from the Nevzorov probe and the associated layer thicknesses obtained by aircraft ascent and descent through layers of various thicknesses. The colored numbers represent the reporting categories of PIREPS summarized in Table A-1.

2.6 RIME ACCRETION RATE ON AIRCRAFT SURFACES

Values of SLW content arising in layers on the basis of adiabatic lifting were made earlier in Section 2.5. An aircraft PIREP scale for the severity of icing hazard in the same units was also considered there, and also figures into the radar comparisons with the PIREP reports discussed in Appendix B. Toward making these numbers for SLW a little more tangible as an aircraft hazard, a simple theoretical estimate for the rime accretion rate experienced by the continuous sweep-out of the SLW is made. If any flat surface sweeps through a continuum of cloud water at speed V, and the cloud water occupies a (dimensionless) volume fraction of the air, which is simply liquid water content (LWC) (in g/m^3)/density

ρ of liquid water in g/m^3, and that water is deposited on the surface as rime ice, then the rate at which the rime thickness (T) changes with time t (also a speed) is simply

$$dT/dt = (LWC/\rho)\, V \qquad (1)$$

If the speed V is expressed in m/s, then the rime thickening rate is also in m/s, but for practical purposes it is convenient to express dT/dt in units of mm per 100 seconds. (For example, 100 seconds might be a typical time between the initial encounter of rime on a windshield or a wing and the time a report (PIREP) is issued.) Figure 2-7 shows the rime accretion rate dT/dt in the latter units for various aircraft speeds ranging from 50 m/s to 200 m/s.

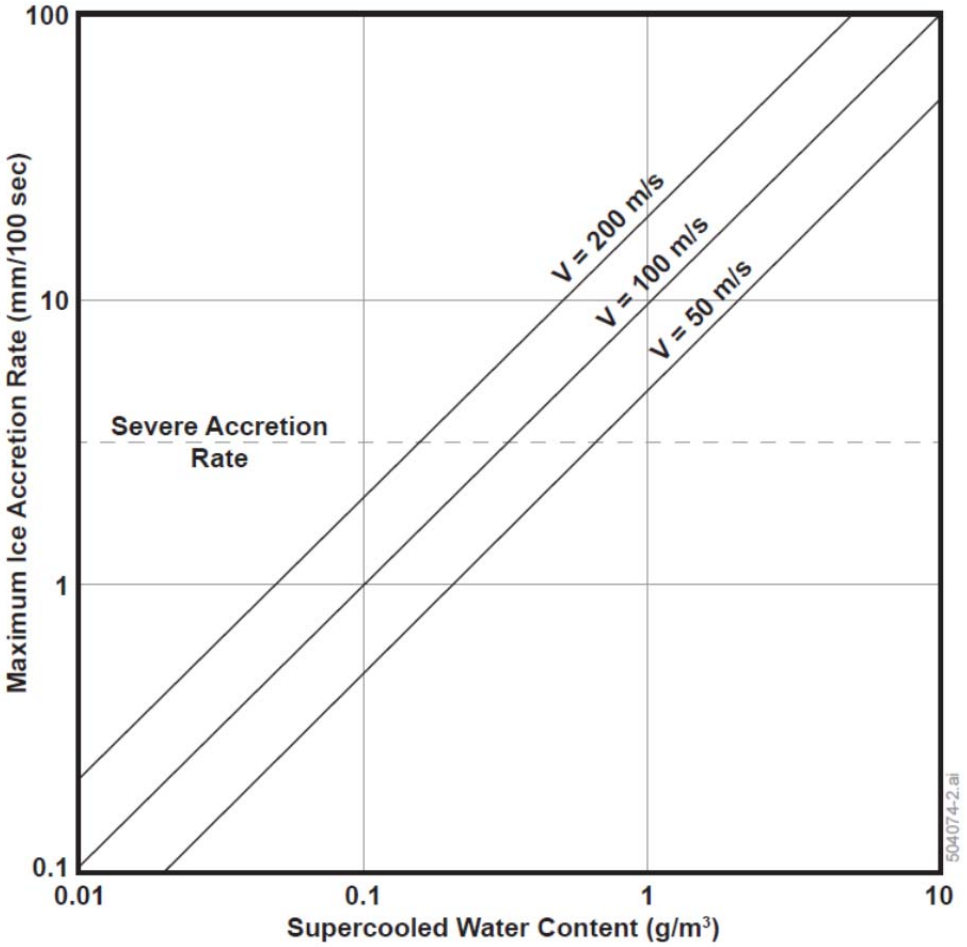

Figure 2-7. Calculations of the rime accretion rate (in units of mm/100 s) based on equation (1), for three different aircraft speeds V.

In reality, equation (1) represents an upper bound on the rime accretion rate, since it is assumed here that every supercooled droplet/drop in the airstream is deposited on the advecting surface to contribute to the rime thickening. If droplets approaching any real surface in the free airstream are sufficiently small, their inertia will be insufficient to carry them into the surface to freeze and contribute to the rime deposit, and instead they will be carried around in the airflow without interception. Fortunately, I. Langmuir and his colleagues have studied the theoretical problem in considerable detail, with application to interpreting rime accretion on cylinders exposed to supercooled cloud on the summit of Mt. Washington in the 1940s (Langmuir and Blodgett, 1960). Their quantity 'rime deposition efficiency' provides a measure of the departure in the rime thickness at the stagnation point of flow (where the rime thickness is maximum) from the simple theoretical estimate in equation (1) above. The parameters of Langmuir and Blodgett that influence the rime deposition efficiency are the droplet radius a, the size of the object experiencing riming, and the speed V of advection through the cloud. As a sample calculation representative of rime accretion in the Wisconsin icing incident treated later in this report (Section 7.2), if we take D = 20 microns, V = 50 m/s and the radius of the rimed antenna 0.47 cm, the rime deposition efficiency is 0.85, indicating that the rime thickness at the stagnation point will be within 15% of the prediction in equation (1). This is an acceptable 'error' for the rime accretion conditions interpreted in Section 7.2. Figure 2-8 reprises Figure 2-7 with a 15% error bar added.

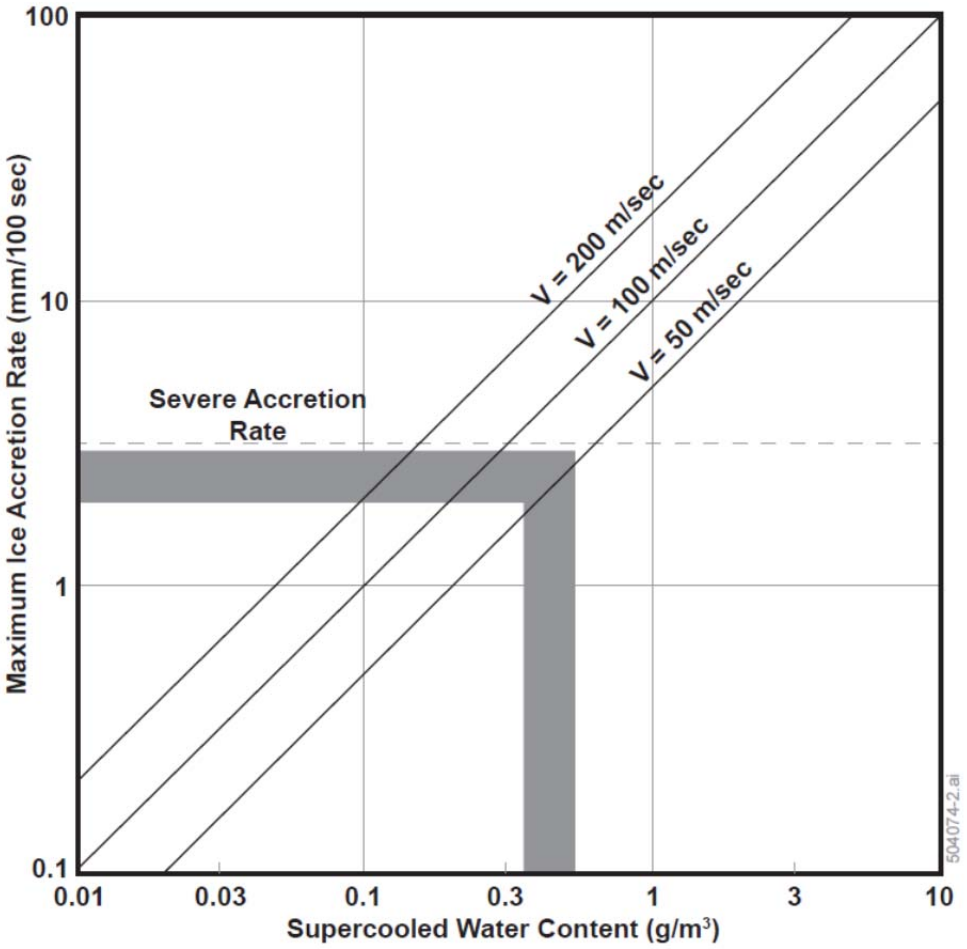

Figure 2-8. Comparison of estimated rime accretion rate with the theoretical predictions shown earlier in Figure 2-7. The gray region provides best estimates (and attendant uncertainty) for the icing incident with the Piper Archer aircraft on February 21, 2013.

2.7 ALTERNATIVE ICING MEASUREMENTS

In situ measurements provide the optimum means to verify the presence of icing. In lieu of that, other secondary methods can be utilized. See Appendix A for more details.

2.8 S-BAND RADAR DETECTABILITY OF SUPERCOOLED WATER IN CLOUD DROPLET FORM

The general consensus is that S-band radars do not have sufficient sensitivity to detect SLW in cloud droplet form. For a realistic calculation of the radar reflectivity from cloud droplets initiated on cloud condensation nuclei (CCN), see Appendix C for additional details.

2.9 TREATMENT OF AIRBORNE X-BAND RADAR OBSERVATIONS

The onboard X-band radar on the Convair provided an opportunity to quantify the radar reflectivity in regions of aircraft-measured SLW. For analysis of these observations, see Appendix D.

3. AIRCRAFT PLATFORM AND FLIGHT PROCEDURE

3.1 AIRCRAFT MEASUREMENTS

Lincoln Laboratory elected in 2012 to engage the NRC and the Convair-580 research aircraft for BAIRS, an in situ validation of ground-based NEXRAD dual pol radar. This decision was made for a number of reasons. In initial considerations of validation, we became aware that the director of Convair research (Dr. Mengistu Wolde) had published earlier work on dual pol measurements of ice particles (Wolde and Vali, 2001) that had immediate relevance to the radar validation effort for the FAA. Secondly, the home base for NRC and the Convair in Ottawa, Canada, was in convenient proximity to NEXRAD radar sites KCLE (Cleveland, Ohio) and KBUF (Buffalo, New York). Thirdly, and most importantly, the NRC Convair team has earned an international reputation for high quality research work on winter storms and on the aircraft icing issues that are of primary concern here. Previous field engagement by this same aircraft, well-equipped with instruments described in greater detail below, include the Canadian Atlantic Storms Program (CASP), the First Canadian Freezing Drizzle experiment (CFDE), the First International Satellite Cloud Climatology Project (ISSCP) Regional Experiment Arctic Cloud Experiment (FIRE.ACE), the Alliance Icing Research Study (AIRS), and the Supercooled Liquid Drop Flight Research Study. During winter 2013, BAIRS took full advantage of this previous experience and expertise, but added one innovation of its own: the provision of real-time NEXRAD dual pol observations to the pilot, navigator, and radar operator of the Convair to aid in the decision making for flight tracks through regions of particular interest.

3.1.1 Characterization of Supercooled Liquid Water

Liquid water content (LWC) at sub-freezing temperatures, the so-called supercooled liquid water (SLW), is the root of the aircraft icing problem, and so is arguably the most important quantity measured by the aircraft in this validation campaign. The principal instrument for that purpose is the Nevzorov probe (Korolev et al., 1998). This instrument performs exceptionally well when the SLW is in cloud droplet form, with a low-end sensitivity in the range 0.003–0.005 g/m^3. This notable sensitivity provides a more effective means than the temperature and humidity measurements in assessing the presence/absence of a water saturation condition in situ. As a backup measurement for SLW, a King hot-wire probe (King et al., 1978) is also available. Though somewhat less sensitive than the Nevzorov probe, this instrument showed excellent agreement with the primary one in regions of appreciable SLW (>0.1 g/m^3). Detailed comparisons of these two instruments in previous missions with the Convair may be found in Cober et al. (2001).

A Rosemount icing detector was also available to assist in the detection of supercooled water and proved useful in distinguishing glaciated and unglaciated cloud conditions. Cober et al. (2001) has estimated a LWC threshold of 0.002 g/m^3 for this instrument.

3.1.2 Characterization of Radar-Detectable Hydrometeors

The validation of ground-based NEXRAD dual pol methods with the in situ aircraft measurements requires the characterization of the hydrometeor shapes and sizes that influence the radar returns. This characterization of the larger hydrometeors is achieved in the Convair measurements with the 2D Optical Array Probes (OAP) manufactured by Particle Measuring Systems (PMS), Inc. The output files of the OAP consist of strips with prescribed widths on which black and white projections of particles are shown, fortuitously in the direction of the gravity vector. This scenario is best suited to characterize the projections most important for dual pol radar interpretation. Three separate probes were available to access different size ranges for hydrometeors. Table 3-1 summarizes the characteristics of the various PMS probes.

TABLE 3-1

Key Characteristics of Separate PMS Probes on the Convair-580 Aircraft

Probe Name	Width of Optical Array	Pixel Resolution	Prime Size Region
2DC	800 μm	25 μm	cloud droplet
2DG	1600 μm	50 μm	transition
2DP	6400 μm	50 μm	precipitation

The smallest particle dimension quantified with this set of probes is ~125 μm, and so all drizzle-size drops are captured within the dynamic range of the PMS imagery. For smaller cloud droplets, the Forward Scattering Spectrometer Probe (FSSP) optical particle counter is used, as described in the next section.

3.1.3 Characterization of Supercooled Cloud Droplets

The most frequent manifestation of SLW in the atmosphere is in the form of cloud droplets. (A convenient physical cutoff diameter for cloud droplets is the size needed for rapid coalescence in collision, requiring a diameter <28 μm.) This size range is below the pixel resolution of the Optical Array Probes (see Table 3-1), thereby requiring a separate instrument for their documentation. The Convair is equipped with two separate FSSP instruments (002 and 146) for this purpose. The output of the FSSP-002 provides the cloud droplet size distribution from 3 to 45 μm in 3 μm intervals. The mean volume diameter (MVD) of the cloud droplet population at 1-second intervals is also a standard output from both the FSSP probes. Previous work by Cober et al. (2001) on the Convair showed good agreement between FSSP instrument pairs.

3.1.4 Thermodynamic Measurements

The in situ verification of sub-freezing conditions in winter storms is a critical aspect of the aircraft validation studies. The ambient static temperature is measured on the Convair with two de-iced Rosemount temperature probes and a reverse flow temperature probe shown in previous campaigns to agree to within ±1° C (Cober et al., 2001). For BAIRS, the temperature and dew point probes were accurate to 0.5° C. Humidity measurements were carried out with an EdgeTech dew point hygrometer. Temperature-humidity measurements on aircraft are generally insufficiently accurate to establish the water-saturation conditions that dictate the habits of ice crystals, and so greater reliance was placed on the Nevzorov probe to establish this condition. Temperature measured to the stated accuracy here are useful for identifying sub-freezing conditions.

3.1.5 SNDI Algorithm for Aircraft Hydrometeor Classification

The characterization of the hydrometeors, which are NEXRAD radar targets, is vital to the in situ validation of the radar-based Hydrometeor Classification Algorithm (HCA) in this study. A principal tool for the characterization of the Convair-580 is the SNDI algorithm (Korolev and Sussman, 2000). Based on automated analysis of the black and white particle images from the PMS OAP, this algorithm identifies four categories of particles: Spheres, Needles, Dendrites, and Irregulars (SNDI) (read as "Cindy"). The 'Spheres' category is aimed at liquid drops, but quasi-spherical ice particles like lump graupel and quasi-circular hexagonal flat plates can also enter this category (Cober et al., 2001). The 'Needles' category includes elongated shapes with aspect ratio >3. Columnar ice crystals are the main contributor. The 'Dendrites' category includes dendritic crystals, stellar crystals, and aggregates of dendritic crystals (i.e., snowflakes). The 'Irregular' category includes all particles having an irregular or random shape. Every five seconds of flight time, the automated SNDI Algorithm produces estimates for the relative prevalence of hydrometeors in these four categories.

The SNDI difficulty with verifying rime on ice particles and with finding a more specific category than 'Irregular' is reminiscent of our efforts to characterize hydrometeors on the ground in snowstorms (see Appendix A.3).

3.2 WHY IN SITU ICING MISSIONS?

The purpose of the in situ icing missions is to verify the presence of supercooled liquid water, determine if the amount of (any) supercooled liquid water should be considered an icing hazard, and validate the performance of the NEXRAD HCA especially focused on classifications associated with the diagnosis of icing potential for use with the NEXRAD Icing Hazard Levels (IHL) algorithm. The in situ icing missions performed by NRC with LL are clearly superior to either icing pilot reports (PIREPs) or ground observations of winter precipitation. The instrumentation on-board provide the ability to confidently characterize (and even quantify) the icing conditions encountered and relate them to the dual pol radar observables from the KBUF NEXRAD.

3.2.1 Flight Planning

A critical distinction of these in situ icing missions is that their flight tracks were determined in real time based on dual pol radar observations from KBUF. Cober et al. (2009) developed proposed icing hazard envelopes for freezing drizzle and freezing rain conditions based on multiple, prior in situ icing mission studies including past missions with the same Convair-580 used in the LL-NRC missions. Without exception, all of those missions relied primarily on meteorological model forecasts of icing conditions to target mission zones. The LL-NRC in situ icing missions required coordination with Buffalo air traffic control and the KBUF National Weather Service (NWS) Forecast office. During flights, communications were established between on-board scientists and LL scientists to coordinate the KBUF radar-indicated flight paths amongst each other and with air traffic control.

3.2.1.1 Overall Targeted Weather Objectives

The NRC Convair-580 home base is at Ottawa International Airport. This is within approximately 90 minutes of the radar volume space of the KBUF NEXRAD (located at Buffalo International Airport). This Great Lakes region (Erie and Ontario) notes Bernstein et al. (2007) is a climatologically favored region for both icing potential and supercooled large drop (SLD) icing potential. The seasonal peaks are mid-late autumn and early spring, but the active winter of February 2013 provided a sufficient variety of winter weather events. The overall plan was to execute three icing missions allowing approximately 90-120 minutes of observations within the KBUF radar volume air space. Additional ferrying time between the KBUF area and Ottawa had to be factored in as well. Three missions were executed and of such interest that the observation times were extended to the maximum possible (up to double the planned time).

Lincoln Laboratory intended to target winter weather that included the dual pol radar positive differential reflectivity (+ZDR) 'bright band' signature at altitudes with temperatures between about –10° C and –15° C. This familiar dual pol radar signature has been observed in both C-band and S-band data in stratiform winter, convective summer, and tropical cyclone environments (Williams et al., 2015, in press). In situ intercept of this feature would verify the presence of supercooled liquid water that is suggested by laboratory cold-box observations and microphysics. This signature was evident in the KBUF data during the first two icing missions but was fleeting and not often sampled by the Convair due to air traffic control restrictions. This dual pol radar feature should be a priority for in situ intercept for any future icing mission program.

In addition to the +ZDR objective, the concurrent objective was to target high-value winter weather icing scenarios as partly informed by icing PIREP frequency. Bernstein et al. (1997) has a convenient cyclone sector mapping guide that relates to icing potential vis-à-vis synoptic system structure for North America. Figure 3-1 includes the guide. The guide assigns numbers to areas that reflect spatial distances ahead of, behind, within, or along the synoptic features: low and occluded low pressure centers, warm front, occluded front, cold front, and Arctic front. There is an inherent icing potential climatology for each

area that dual pol radars across the U.S. now monitor possibly leading to association with dual pol radar features. The three in situ icing missions were able to sample three different sectors.

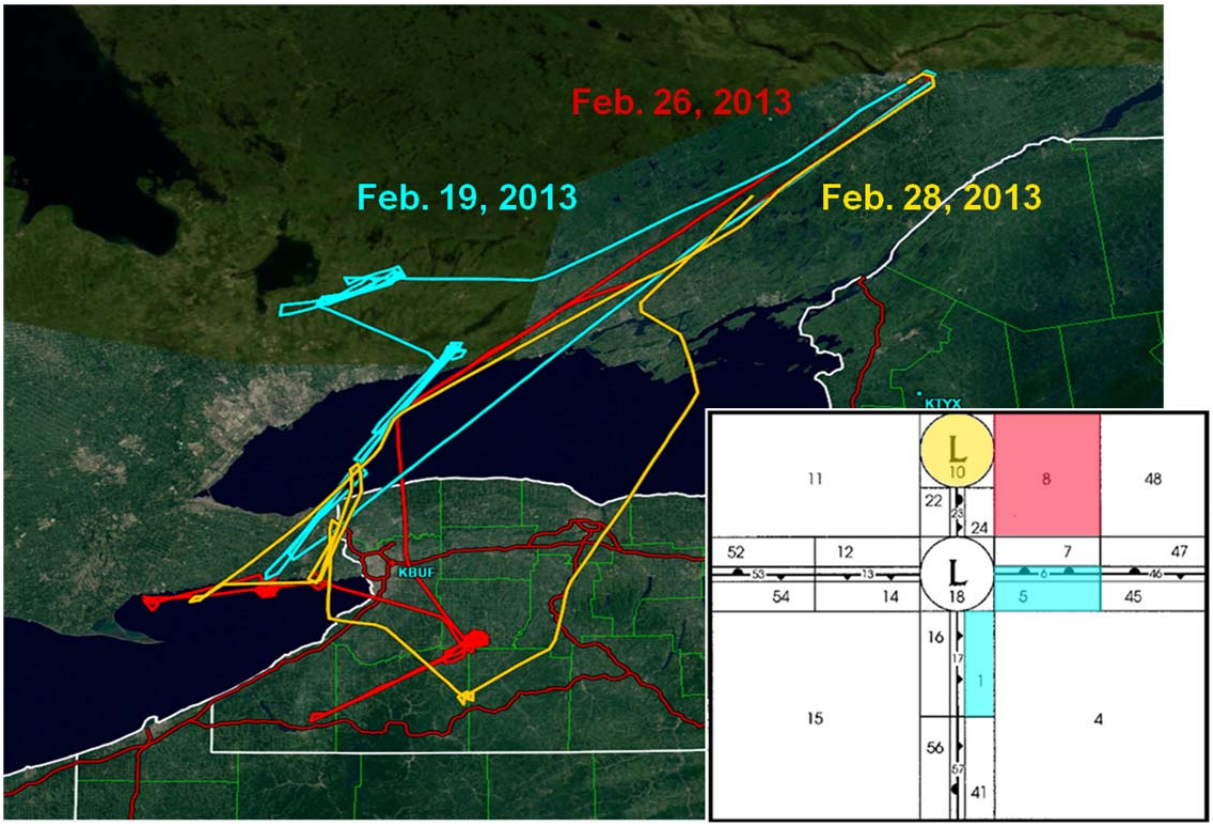

Figure 3-1. An overview of the flight tracks is shown. The Bernstein cyclone sector mapping guide is included on the lower right. Color-highlighted areas are associated with like-colored flight tracks.

3.2.2 Preflight and Flight Procedures

The preflight and flight procedures were handled by LL staff meteorologists through daily briefings, day-of-mission briefings, and in-mission briefings. An overview of the 2013 missions follows. Three in situ icing missions were executed – on February 19, 26, and 28 – that totaled 14 flight hours with 8 hours of weather probing in the target areas. Figure 3-1 shows flight tracks of the February 19 (cyan), 26 (red), and 28 (yellow) missions. The Bernstein guide is also included. It shows that the February 19 mission focused on the area at and near an approaching warm front (and eventual cold front). The February 26 mission was ahead of a warm front and low pressure system. The February 28 mission was in the area of a days-old occluded low pressure center. The area east of KBUF, especially over Lake

Ontario, is restricted military air space not available for probing, but it was open to transit. Spiral probing through a deep layer is seen as concentrated swirls in the tracks. Areas of back and forth transects are evident also. The flight altitudes ranged from a few thousand feet up to cloud top around 20–25 thousand feet.

Daily briefings were held once and sometimes twice per day during the mission window. The briefing included a discussion of the synoptic situation anticipated for the following five days with a yes-no-maybe verdict regarding worthiness for an icing mission. A briefing document was provided that included a marked-up Bernstein cyclone sector mapping guide. For a "go" mission verdict, LL also produced a flight plan document that included a target box in the KBUF radar range. The briefings also included discussion of issues or problems about plane staffing and plane maintenance as well as performance and calibration issues regarding the onboard sensors and radars. Early on there was a time-of-day issue that was resolved part way through the campaign when all pilots were night-flight certified. Once a flight was a "go" for the next day, LL notified KBUF and KCLE NEXRAD radar operators to make a special volume coverage pattern (VCP) request to scan with 12 or 212 (most frequent updating scanning) or 31 (high sensitivity clear air scan used in winter). LL also notified the Cleveland ARTCC (Air Route Traffic Control Center) who supported each mission with requests for extra pilot reports of icing.

Day-of-mission briefings began after LL staff meteorologists fine-tuned their target area forecast and convened a briefing with the on-board pilots and scientists about one hour prior to leaving the home base at the Ottawa International Airport. In addition to the usual weather forecasting challenges, LL also planned for timing uncertainty regarding leaving the Ottawa base due to considerations for deicing, crew availability, and time of day. Once in transit to the initial target area, communication was established between the Convair-580 and LL to begin the correspondence about KBUF radar-guided target area evolution and relayed air traffic control concern.

The during-mission briefing experience from the February 2012 LL-NRC icing mission with an intermittent satellite phone hook-up made improved communications a priority for the 2013 missions. LL needed reliable real-time Convair position data. The on-board scientists and pilots needed real-time KBUF data with a marking of the Convair position. Everyone needed real-time communication for live flight track determination based on evolving KBUF dual pol radar guidance and air traffic control interactions. For the final flight, all criteria were worked out sufficiently to have an invigorating experience. With the first two flights, communication via a satellite link on the plane was occasionally sporadic. This link was the lifeline for real-time guidance via a chat mechanism, position data, and for real-time NEXRAD KBUF and KCLE radar data products to the on-board scientists. The radar product imagery was made accessible through LL's ftp server. Gibson Ridge GR3 software was used to create images of NEXRAD Level 3 products with LL adding the plane position and/or proposed transects. With communications established with the plane, the crew had access to KBUF and KCLE data through 3.5° elevation angle scans of reflectivity, differential reflectivity, and hydrometeor classification. This data exchange allowed LL scientists to explain to on-board scientists the reasoning for a targeted heading (and

on-board scientists could inform pilots). A chief challenge for the during-mission briefings was to give a lead time to the Convair pilots to enable successful intercept of the desired radar-determined target area based on projection of the radar feature advection.

This page intentionally left blank.

4. SPACE-TIME COMPARISON OF IN SITU AIRCRAFT AND GROUND-BASED RADAR MEASUREMENTS

For each in situ icing mission, flight track position data are provided at one second frequency. The data include the Convair-580's latitude, longitude, and altitude. Those three values need to be reconstructed in terms of the range and azimuth angle and elevation scan angle as viewed from the KBUF NEXRAD for comparison of the in situ measurements against the radar's data. The Buffalo radar location obviously has fixed values for latitude, longitude, and altitude. Using Microsoft Excel, the Haversine method (Sinnott, 1984) was used to determine the separation distance between KBUF and the Convair. The Haversine method (equation 1 series) requires the latitude and longitude of two points to compute the shortest distance between them. It has been shown to be at least as accurate as a law of cosines especially for small distances. It is also of a form convenient for spreadsheet calculations.

$$a = \sin^2(\Delta\varphi/2) + (\cos(\varphi_{KBUF}) * \cos(\varphi_{CONVAIR}) * \sin^2(\Delta\lambda/2))$$

$$c = 2 * \text{atan2}(\sqrt{(1-a)}, \sqrt{(a)}), \text{ as used in Excel}$$

$$\text{separation distance} = R \times c \qquad (2)$$

where R is earth's mean radius

φ_{KBUF} is KBUF latitude,

$\varphi_{CONVAIR}$ is Convair latitude,

$\Delta\varphi$ is delta of the latitudes (Buffalo – Convair), and

$\Delta\lambda$ is delta of the longitudes (Buffalo – Convair).

Using the separation distance and altitude difference between KBUF and the Convair results in the range and elevation angle associations being determined. An arctangent formula (equation 3) was used to determine bearing, which translated into a KBUF azimuth angle. This overall approach for separation distance and bearing was compared to those described in the Appendix of Plummer et al. (2010) that performed similar computations based in the law of cosines and found comparable results.

$$\text{bearing} = \text{atan2}((\cos(\varphi_{KBUF}) * \sin(\varphi_{CONVAIR}) - \sin(\varphi_{KBUF}) *$$

$$\cos(\varphi_{CONVAIR}) * \cos(\Delta\lambda)), \sin(\Delta\lambda) * \cos(\varphi_{CONVAIR})), \qquad (3)$$

as used in EXCEL.

For the NEXRAD elevation angle, the center of the beam altitude was determined based on the NEXRAD beam propagation model for a well-mixed atmosphere. With the Convair's position mapped to the KBUF radar volume space, a determination is made as to which elevation angle beam center is closest

to the Convair as well as how many elevation angle scans intersect with the Convair's position. For the first two icing missions, VCP 12 was the primary scan strategy employed. During an early portion of one mission, VCP 21 was used. For the third icing mission, VCP 31 was used. Figure 4-1 shows the available elevation scan angles for these three VCPs. Depending on the Convair's position and scan strategy, often multiple elevation angle scans would intersect with the plane's position. Assuming uniform beam filling of scatterers, the "best" elevation angle associated with the Convair would be that with minimum distance from the beam center. There were instances, however, when the Convair position was not mapped to any NEXRAD beam and for which no direct comparison between the in situ measurements and ground-based radar are possible. These include positions at a distance beyond the KBUF coverage area during en route and departure and positions not within any elevation angle.

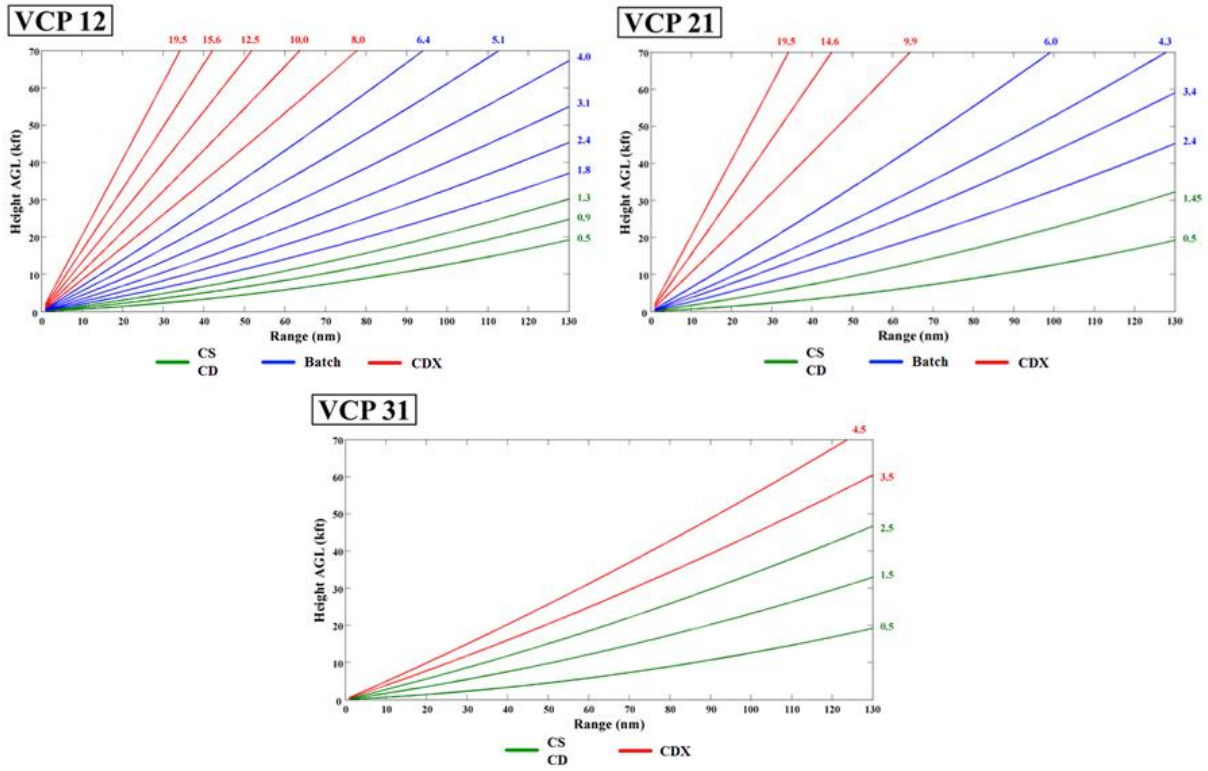

Figure 4-1. The elevation scan angles are depicted for the volume coverage patterns (VCP) 12, 21, and 31 used in the NEXRAD network. The VCPs typically complete their entire scan angle sequences in about 4.1, 6, and 10 minutes, respectively. Color-coding indicates the type of scanning: CS (constant surveillance), CD (constant Doppler), Batch (a blend of CS and CD), and CDX (a faster rate Doppler).

The spatial matching of the aircraft position to the best-matched NEXRAD elevation and azimuth angle was performed using the high frequency one-second data. However, the temporal matching of the aircraft to NEXRAD azimuth angle time was performed using the time stamps contained in the Convair five-second data. These data represent an average of the one-second data and are deemed sufficient for comparison. The five-second data contain valuable crystal particle type frequencies determined by the Korolev SNDI particle identification technique described in Section 3.1.5 and are necessary for comparison with other in situ data but are not available in the one-second data. As noted by the VCP definitions above, the duration to complete a VCP varies. As such, the radar volume closest in time to the Convair-NEXRAD best match spatially could occur before or after the Convair arrived at that location.

The time for the best match azimuth is necessary to determine the best match temporally. The start time of each NEXRAD azimuth angle is not provided explicitly in the Level 3 product header, but it can be calculated since the product header does provide the volume start time and the first azimuth angle of each elevation angle scan. That, with the well-known time duration for the VCP in operation, is all that is needed to determine the best match azimuth time. The time difference between the aircraft five-second time stamp and the best match azimuth angle's time associated with the Convair position was computed for all applicable radar volumes and the minimum time difference determines the radar volume to use. That minimum time difference could be up to ½ the VCP time duration, but in many instances, it is much less.

Once the spatial and temporal association of each Convair five-second observation to the NEXRAD volume, elevation scan angle, azimuth angle, and range distance from KBUF was determined, statistical analysis of the dual pol products within a small 15 range bin spatial window (5 range bins by 3 azimuth angles) centered on the Convair position was performed. The size of each NEXRAD range bin is 250 m. The window size used for matching is intended to be sufficient to encompass the aircraft flight track travelled in five seconds at its nominal speed of 100 m/s, yet is small enough of an area to prevent loss of any signal in the polarimetric products from too large a window area. Dual pol products studied include smoothed reflectivity (SMZ), differential reflectivity (ZDR), correlation coefficient (CC), specific differential phase (KDP), and hydrometeor classification (HC) produced by the NEXRAD HCA. Statistical metrics computed among all valid range bin values within the window include the 5^{th} percentile, 95^{th} percentile, mean, median, and standard deviation of the first four products listed above and the mode and top three dominant hydrometeor classifications.

Time series plots containing some of the Convair in situ measurements and the matched NEXRAD dual pol data were created for each 10-minute period extending throughout each flight mission. Figure 4-2 shows an example of time series data for the time period 1420–1430 UT on February 19, 2013. Each time series plot contains three panels. The top panel shows a frequency breakdown of all particle categories observed by the PMS 2DC imager and as determined by the SNDI algorithm for each five-second observation. The particle categories include spheres (burnt red), irregulars (gold), needles (cyan), and dendrites (blue). This example illustrates a period when the Convair flew through a regime dominated by

irregulars and needle crystals, transitioned to a mix of spheres and irregulars, to dendrite crystals and irregulars, and then to mainly irregulars.

The center plot in Figure 4-2 contains line plots of the Convair measured temperature (blue) and Nevzorov liquid water content (red). The solid line at the top represents the mode of the NEXRAD HC detected within the spatial matching window and color-coded by class. Classes include 'Biological' (BI), 'Ground Clutter' (GC), 'Ice Crystals' (IC), 'Dry Snow' (DS), 'Wet Snow' (WS), 'Rain' (RA), 'Heavy Rain' (HR), 'Big Drops' (BD), 'Graupel' (GR), 'Hail-rain' mix (HA), and 'Unknown' (UK). The measured temperature was near constant at –2° C for much of the period and began to lower at 1427 UT. LWC was substantial for the first 3.5 minutes of the period with a peak value of 0.25 g/m^3 and at a time when irregulars, needle crystals, and spheres were the dominate particle types. Note how the LWC diminishes to near 0 at the time dendrite crystals begin to dominate from higher values during needles.

The bottom plot within Figure 4-2 shows the NEXRAD mean SMZ (magenta), the mean NEXRAD ZDR (black), and the mean reflectivity measured from the horizontally pointed Convair X-band radar (green). The X-band reflectivity does not match the S-band NEXRAD SMZ magnitude, but it generally mirrors the trends observed by NEXRAD. A significant increase in reflectivity is observed by both radars during the time when the dendrite crystal frequency increases. Solid lines of the NEXRAD SMZ and ZDR indicate the Convair time and NEXRAD azimuth angle time are matched within 120 seconds from each other. Dashed lines indicate the data are outside the window.

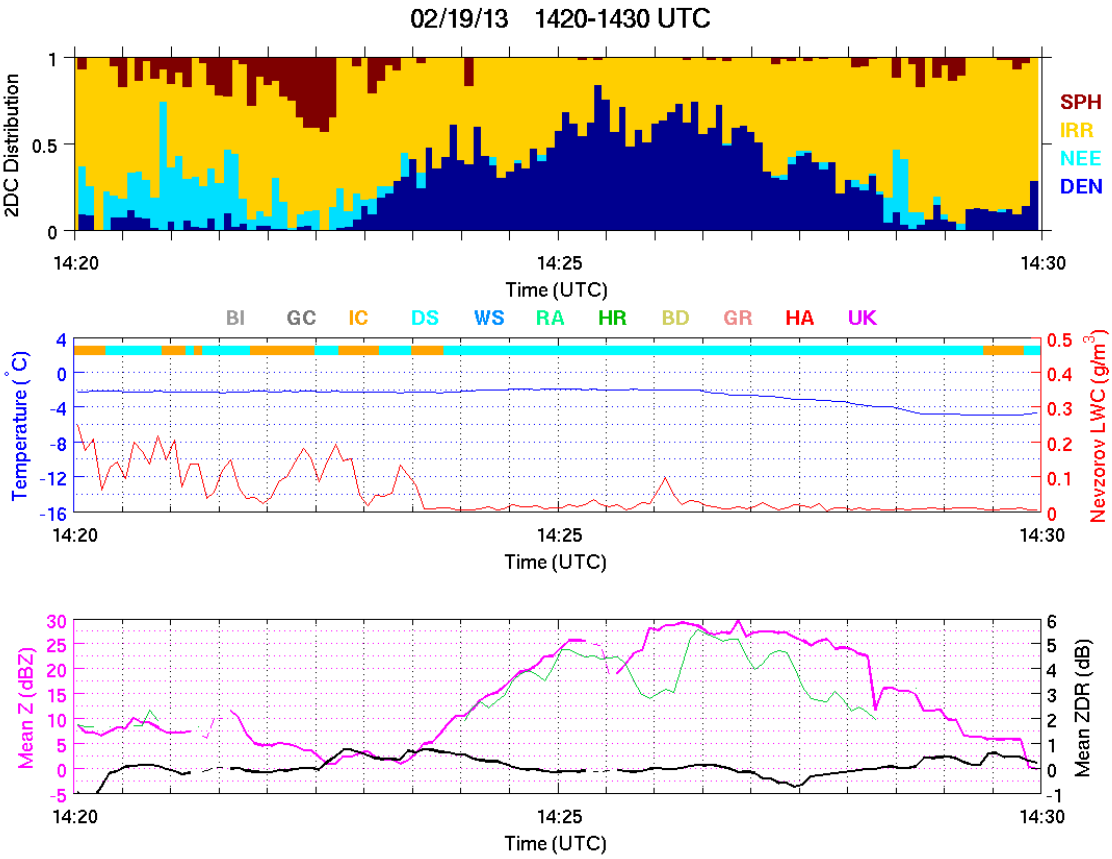

Figure 4-2. Three-panel sample of five-second time series plots for the 10-minute period 1420–1430 UT on February 19, 2013. The top panel shows the particle frequency distribution produced by the SNDI algorithm and color-coded by particle type. The middle panel contains records of the temperature (blue) and Nevzorov LWC (red) measurements with the color-coded mode of the NEXRAD HCA-detected class displayed at the top of the panel. The bottom panel shows records of the NEXRAD mean SMZ (magenta) and mean ZDR (black) values among radar bins most closely matched to the Convair position in space and time. The green line in the bottom panel represents the Convair X-band mean reflectivity in the horizontal beam.

This page intentionally left blank.

5. GENERAL FINDINGS – THREE FLIGHT INTER-COMPARISON AND INTEGRATION

Detailed highlights of each of three flights focusing mainly on the periods of conspicuous SLW and attendant icing hazard are found in Section 6. But as preface to these details, it is useful to make some gross inter-comparisons of radar variables including mean SMZ, mean ZDR, and the prevalence of SLW and the HC mode for the three flights. The meteorological conditions on each day were markedly different, and this fact is reflected in the four variables chosen for inter-comparison.

Figure 5-1 shows the complete distributions of radar smoothed mean reflectivity, mean differential reflectivity, and supercooled water for each of three flights, in chronological order from top to bottom. The two radar variables were organized by values measured for the KBUF NEXRAD within close proximity of the aircraft throughout the individual flights.

The mean SMZ distributions in Figure 5-1 alone are good indicators of the marked contrast in convective intensity from case to case. For the most strongly convective storm (February 26–27) in which graupel particles were found in abundance and which also produced supercooled drizzle and freezing rain, the maximum reflectivities exceeded 50 dBZ, more typical of summertime weather. In contrast for the weakest case on February 28, a delicate snowstorm whose documentation was facilitated by the clear air scanning mode adopted by KBUF for that day, the majority of radar echoes are in the negative range of dBZ and extending down to –20 dBZ. For the snowband ‘Dry Snow’ case of February 19, more moderate limits of reflectivity are apparent on both ends of the distribution.

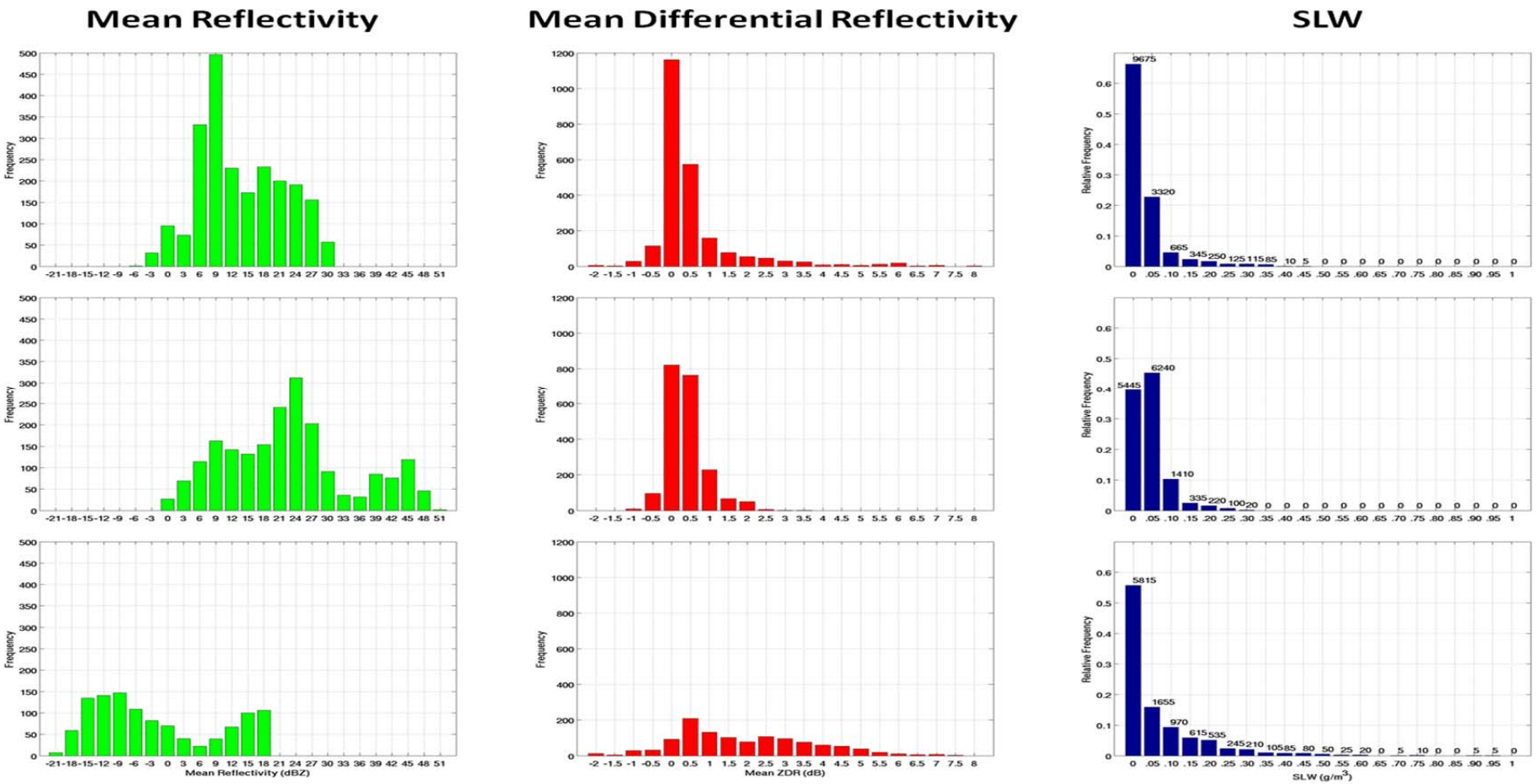

Figure 5-1. Distribution of KBUF mean SMZ (left), mean ZDR(middle) and SLW(right) values over the duration of each of three flights on February 19 (top), February 26–27 (middle), and February 28 (bottom).

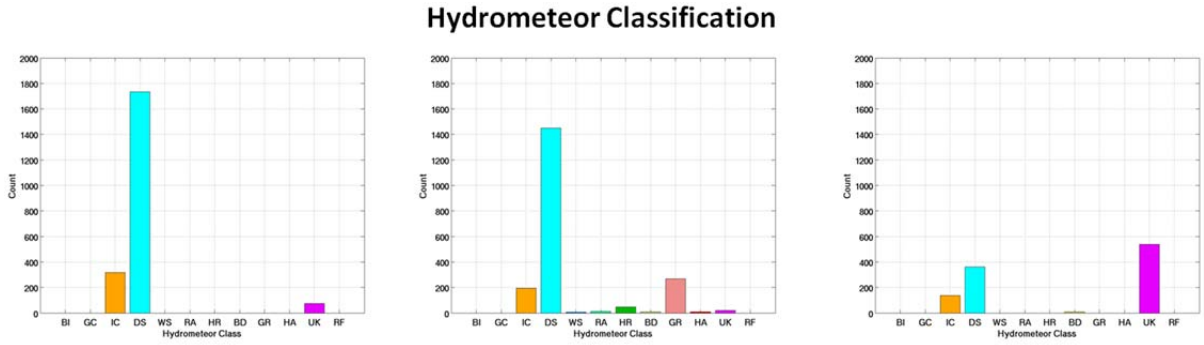

Figure 5-2. Distribution of NEXRAD HCA categories (described in Section 4) for each of three flights on February 19 (left), February 26–27 (middle), and February 28 (right).

The distributions of mean ZDR also reflect differences in convective intensity. The ice crystal targets that are most strongly anisotropic to dual pol radar are most prevalent in conditions of weak ascent with minimal turbulent mixing, riming, and aggregation, all of which often promote more isotropic response. The ZDR histogram for the delicate snowstorm on February 28 (bottom, middle Figure 5-1) shows the most pronounced tail in positive ZDR values (out to values of +8 dB), indicative of quasi-uniform populations of single ice crystal types verified in the PMS imagery, and including appreciable numbers of the most anisotropic crystals – the hexagonal flat plates. In contrast, the most strongly convective case, February 26–27, shows the tightest distribution of ZDR values around zero – the isotropic radar response. 'Dry Snow,' a prevalent verified category of hydrometeor on February 19 and often associated with 'irregular' shapes in the SNDI algorithm, was also commonly a near-zero ZDR target.

The probability distributions of SLW measured with the Nevzorov probe all include a count at the top of each bar for the total time (in seconds) during the flight the LWC intervals were registered. The probability distributions show more similarities than differences, flight to flight, and what differences do exist are more difficult to interpret than the radar parameters just discussed. All distributions show monotonic and strongly declining probabilities of SLW over the measurement range from the assumed instrument sensitivity of 0.005 g/m^3 (Korolev et al., 1998) to the largest values encountered (~1 g/m^3). The probability that SLW will exceed 0.3 g/m^3 varies greatly from flight to flight with values of 6% of the time on February 28 to a value as low as 0.1% on February 26–27. This spread may have as much to do with aircraft sampling strategy as intrinsic storm microphysics. For example, on February 28, the 'porpoising' maneuver of the aircraft kept the plane in and out of layers of SLW rather than on a track of long traverses in glaciated conditions (as on February 19). The February 26–27 case showed the largest probability of the super-threshold SLW, and in that case the Convair remained for long periods within conditions of mesoscale ascent, where maintained SLW was more likely.

Figure 5-2 (HCA distributions) highlights the different traits of each mission. The ‘Dry Snow’ class dominates the first two missions. However, on February 26–27, there is a notable inclusion of additional classes other than snow as the aircraft traversed near and within the melting layer. This mission is the only mission that can provide a glimpse into performance of non-snow classes. The mission of February 28 distinguishes itself with the notable registering of the ‘Unknown’ class. Additional aspects of each mission follow in Section 6.

6. FINDINGS BY FLIGHT

In this section, greater 'case study' detail is provided for some of the more conspicuous periods of SLW during each flight. Graphics utilized to illustrate aspects of the case studies include the following:

1. A 3-panel time history of the output of the SNDI algorithm (top), the evolution of SLW from the Nevzorov probe and the in situ temperature (middle panel) along with the HCA classification, and the KBUF and Convair X-band measurements within a specified time window (±120 seconds – solid line; >±120 seconds – dashed line) of the aircraft measurements,
2. A 6-panel plot showing the space-time ('4D') evolution of the KBUF radar observations (mean SMZ and mean ZDR) in the vicinity of the aircraft,
3. Selected sequences of image strips from the PMS 2DC probe to disclose particle shapes, and
4. Occasional photographs taken from the window of the Convair-580.

6.1 FEBRUARY 19, 2013 ('DRY SNOW' FLIGHT)

This day flight originated in Ottawa at 8:07 a.m. (1307 UT) and was completed almost exactly five hours later at 13:08 p.m. (1808 UT). The plan view of the entire flight is shown in Figure 6-1. The main meteorological objectives were eastward moving snow bands in the northern sector of the KBUF radar. The predominant HCA classification was 'Dry Snow,' from which the flight was given its name. The predominant SNDI designation was 'irregulars' exhibiting mostly isotropic behavior in KBUF differential reflectivity. This flight has highlighted more than any other the ambiguity of the 'Dry Snow' category in the context of aviation icing hazard, since 'Dry Snow' was identified with and without the presence of supercooled water. The original HCA formulation by Park et al. (2009) does not provide for this distinction.

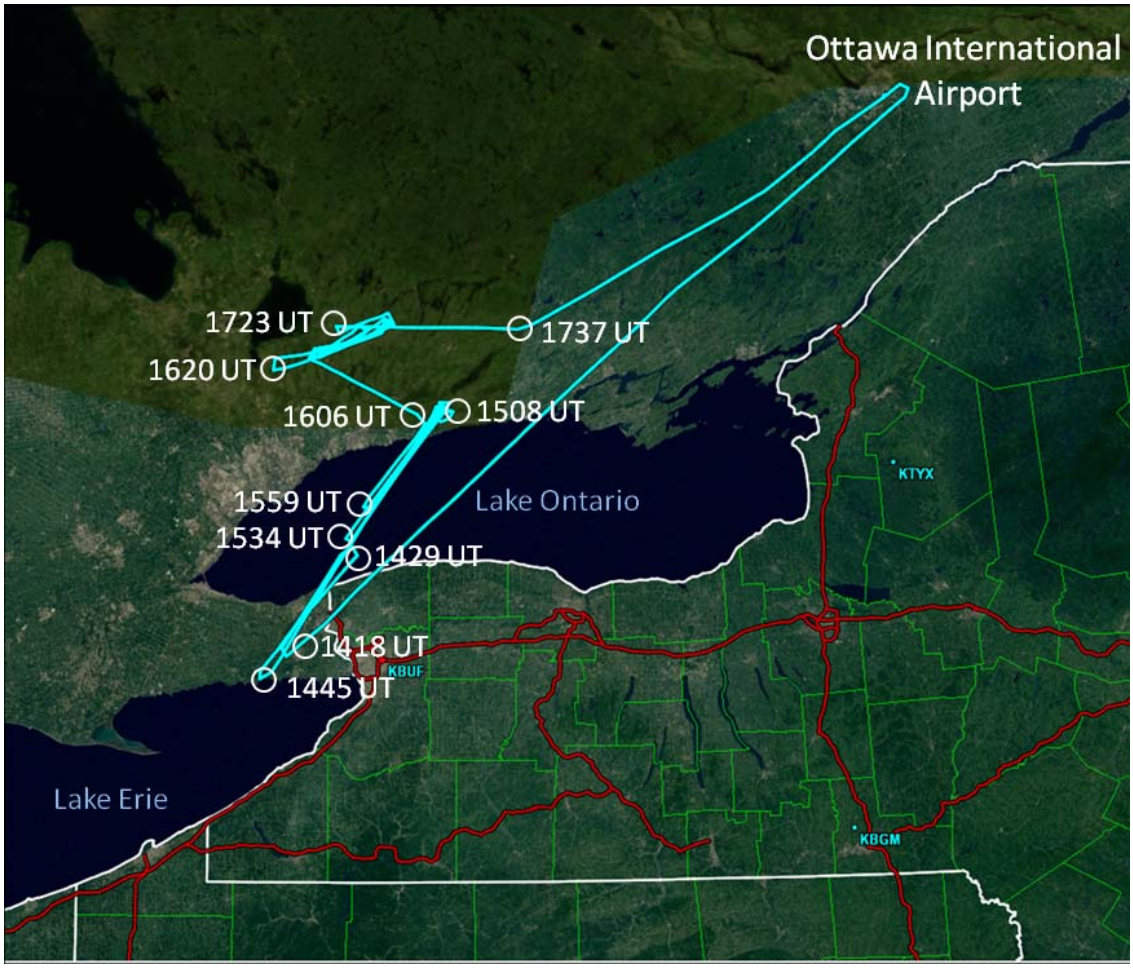

Figure 6-1. Plan view of the entire flight track on February 19, 2013 originating and ending in Ottawa.

The aircraft altitude variations for this flight are compactly illustrated in Figure 6-2. The strategy on this day for many fixed altitude flight segments was well-suited for investigating horizontal variations in SLW. (That strategy was changed in later flights (notably February 28) with the objective of investigating vertical variations linked with laterally extensive layers of SLW.)

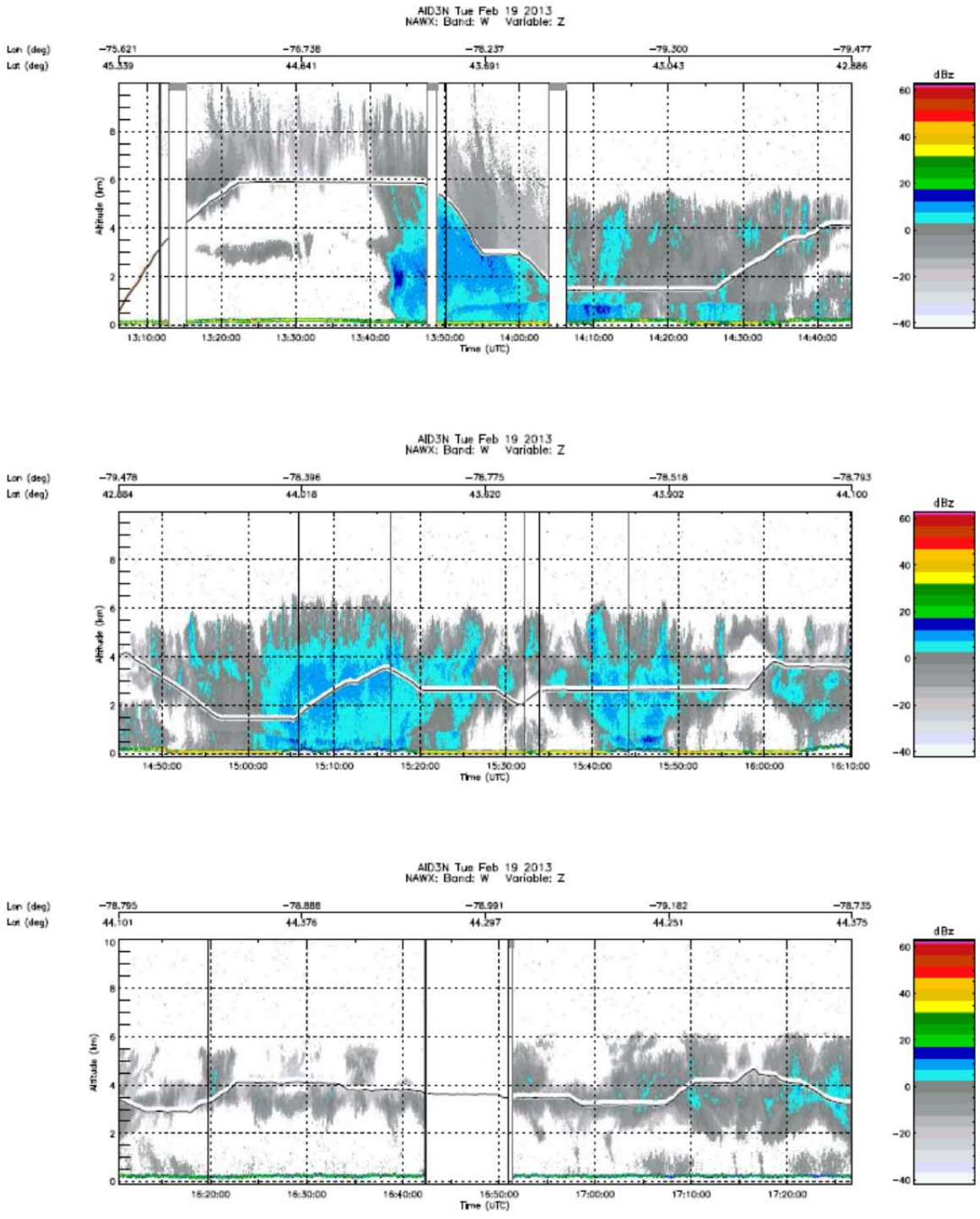

Figure 6-2. Time-height history of the flight on February 19, 2013, with key reflectivity displayed from the vertically pointing onboard W-band radar.

The most prominent period of SLW in this flight, both from the standpoint of the peak value (>0.4 g/m^3) and the duration (>15 minutes or nominally 90 km of flight track at 100 m/s) occurred over a constant altitude track (with T = –2° C) shown in Figure 6-2, and shown in greater detail over a 10-minute interval (1410–1420 UT) in Figure 6-3. Figure 6-2 also shows weak evidence of a radar bright band in the vertical beam W-band data at an altitude of around 800 m, and that is consistent with an S-band PPI at around this time and with a model sounding that depicts 'warm' surface air (not shown). Figure 6-2 also shows a vertical development approximately 3500 m above the altitude of the plane, consistent with a mechanism for sustaining SLW, and with some evidence for lateral variations that may reflect changes in convective development.

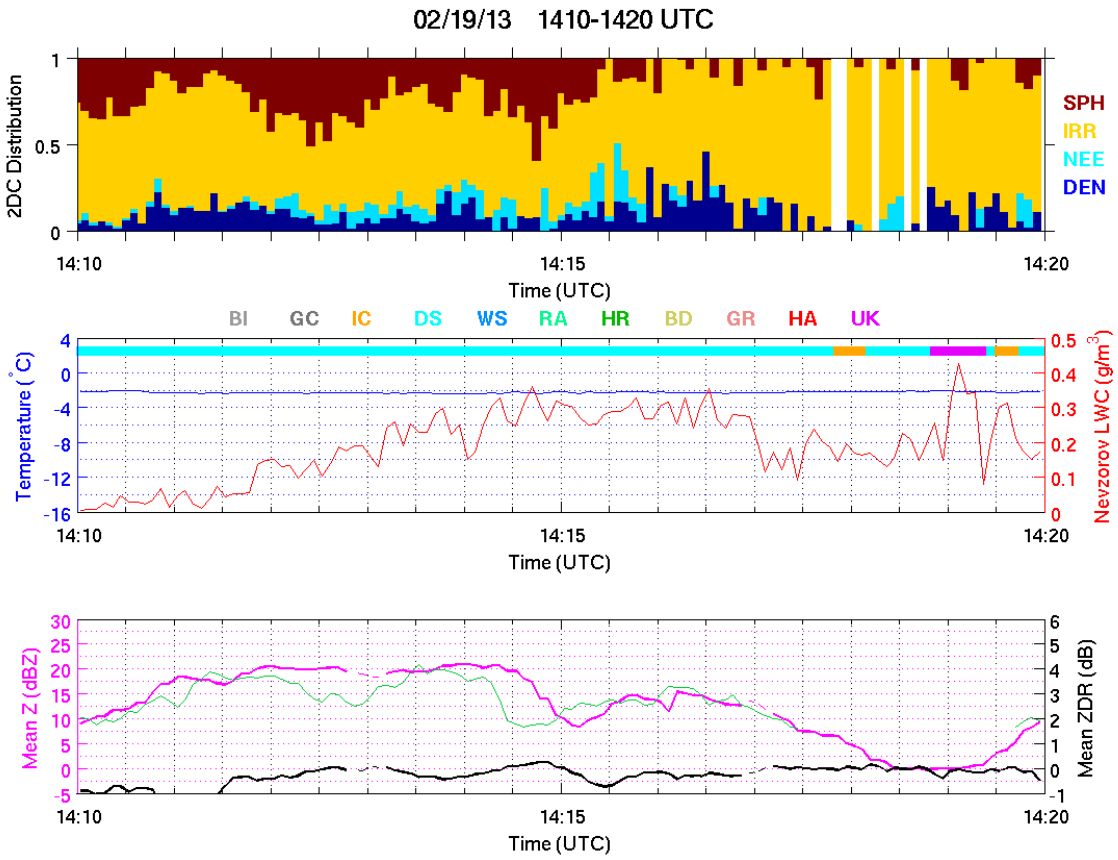

Figure 6-3. Ten-minute time series segment of nearly continuous supercooled liquid water (middle). Also shown are the SNDI hydrometeor designations (top), the Hydrometeor Classifications (middle), the S-band and X-band mean reflectivity and the S-band mean differential reflectivity (bottom). Solid (dashed) trace indicates data within (outside) the ±120 second designated time window.

The airborne FSSP sample at 1415 UT (not shown) showed abundant SLW in cloud droplet form, with a mean volume diameter of 13 μm. The PMS 2DC imagery (Figure 6-4) shows evidence for many irregular shapes, consistent with the predominant SNDI designation in the top of Figure 6-3, but also evidence for graupel particles with diameters substantially exceeding the 800 μm 2DC strip width. A significant percentage of 'Spheres' also appears in SNDI, and one can see quasi-spherical shapes in the imagery in Figure 6-4 that are most likely graupel particles in the 100–200 μm diameter range. They are not likely drizzle drops because the tail of the FSSP data on cloud droplet sizes is not strongly developed beyond 30 μm. Both the presence of quasi-spherical graupel and the irregular shapes documented with the aircraft data provide for a close-to-isotropic radar return, consistent with the ZDR measurements over this interval, which are close to 0 dB. The predominant HCA category over this 10-minute interval of Figure 6-3 is 'Dry Snow.'

Figure 6-4. Particle Measuring Systems 2DC imagery for the 47-second time interval 14:14:16 to 14:15:02 UT on February 19, showing evidence for irregular shapes, some columns, large graupel particles, and a number of hydrometeors in the 'Spheres' category that are most likely small graupel particles.

Four-dimensional (space and time) analysis was undertaken over this same time interval to determine whether the pronounced SLW along a horizontal track would influence the development of the surface-based radar data, as a possible diagnostic for its presence. This test is illustrated in Figure 6-5 that shows three panels from the same radar PPI but taken at three successive scan time intervals (14:08:59 UT, 14:13:15 UT, and 14:17:31 UT). The X-Y position of the Convair is marked by a black X in each panel. Consistent with expectation, one can discern local increases and decreases in radar reflectivity in the top set of panels (superimposed on the northeastward advection of radar features), with evidence for growth at the location where SLW has been documented by the aircraft. No obvious change in ZDR (lower panels) is evident in that location, but in another region to the north experiencing decay, some enhancement of ZDR is evident, which may be associated with the formation of an edge effect in the trailing portion, something that we have documented in other dual polarimetric analyses in winter storms (Williams et al., 2015).

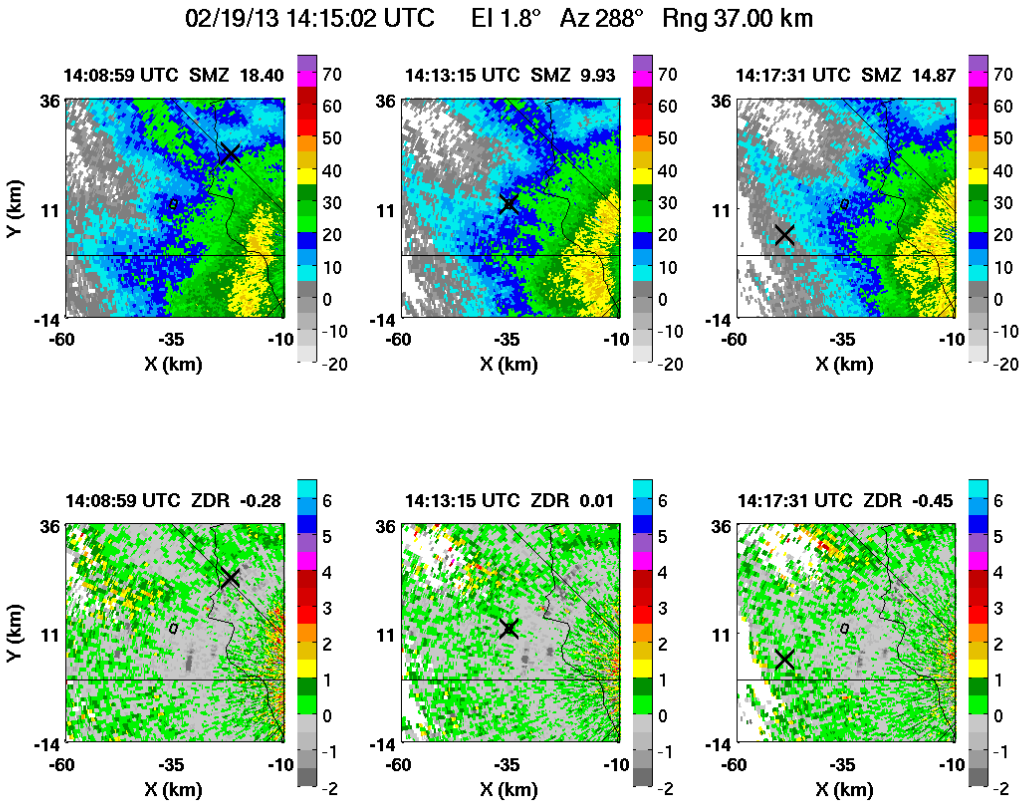

Figure 6-5. Three-panel plots of KBUF S-band SMZ (top) and ZDR (bottom) at three successive times to illustrate changes in parameters associated with the presence of SLW documented by the aircraft. The changing aircraft location (with time running from left to right in the plot sequence) is marked with a black X as described in the text.

Following the time interval documented above, the aircraft increased its altitude from 1427 UT to 1442 UT (see Figure 6-2) and exited the cloud into clear air above at an altitude just over 4000 m. Photographs were then taken from the plane looking downward onto the cloud indicating a glory and presence of SLW. Later, around 1700 UT, the Convair-580 was near 4000 m altitude in similar conditions. A photograph from then (Figure 6-6) shows a clearly defined glory with the shadow of the Convair-580 in the "bulls-eye." This documentation of the cloud top at –20° C is evidence in itself for supercooled cloud droplets.

Figure 6-6. Documentation of the optical phenomenon glory in the cloud top when the aircraft exited into clear air near 4000 m. This observation of an upper cloud boundary at –20° C is evidence in itself for the presence of supercooled droplets.

Supercooled water in cloud droplet form is often present in the tops of winter storms. The aircraft observations on February 19, 2013 afforded an opportunity to study this with an optical phenomenon known as 'glory,' in conjunction with the FSSP observations of cloud droplet size and the Nevzorov probe for supercooled water content. This optical diffraction pattern is formed by supercooled cloud droplets illuminated by sunlight, with colored rings concentric around the shadow of the aircraft on the sunlit cloud. The glory was photographed (by the lead author) as the plane dipped in and out of the cloud top, whenever the Sun-aircraft-observer geometry was favorable. Examples of the glory are shown on the right in Figures 6-7 and 6-8. All of these observations were carried out at an aircraft altitude near 4000 m where the in situ temperature was in the range –18° to –20° C.

The FSSP probe was operating continuously during the traverses in and out of the cloud, recording full droplet spectra at 1-second time intervals (representing 100 meters in space), in size bins of 3 microns and with droplet concentrations in units of cm^{-3}/micron. The existence of cloud droplets with the FSSP probe showed excellent agreement with the presence of supercooled water as recorded simultaneously with the Nevzorov probe. The comparisons confirm the existence of supercooled water in cloud droplet form.

Theoretical Mie scattering calculations on spherical water droplets of a single size show a unique relationship between the angular radius of the red (visually most prominent) glory ring and the droplet diameter (Laven, 2008). In this case, we have used the simple relationship for the angular diameter of the red ring (in degrees) = 96/D, where D is droplet diameter in microns. The angular diameter of the red ring has been determined from direct measurements on the photographs, and through the use of known dimensions on the aircraft wing and the measured distances from the observation window to these objects, for calibration purposes. The estimated droplet diameters for each glory observation are indicated by the red bars in Figures 6-7 and 6-8. The widths of the red bars represent the overall uncertainty in this measurement of droplet diameter. In the same figures for comparison are the cloud droplet spectra from the FSSP probe. These spectra represent 30-second averages of 1-second spectra, normalized to 1 second. The half-widths of these spectra are of the order of 3 microns, and so are comparable to the size resolution in these measurements.

In 11 separate observations of the same kind shown in Figures 6-7 and 6-8, the glory-measured droplet diameter either matches the peak droplet size in the FSSP spectrum, or is one bin removed from the maximum. We consider this excellent agreement between the two completely independent measurements. It should also be noted that the FSSP size distributions show quasi-monodisperse behavior, consistent with the existence of a well-defined diffraction pattern. In all cases, the inferred droplet sizes are substantially smaller than the ~28-micron-diameter threshold for droplet coalescence, in which scenario a major broadening of the droplet spectra would be expected, with a consequent destruction of the glory diffraction pattern. Such a scenario in runaway conditions could lead to eventual precipitation-sized particles large enough for dual pol radar detection. This fundamental 28-micron-size threshold for precipitation sets a minimum red ring angular diameter for the glory at about 3.4°.

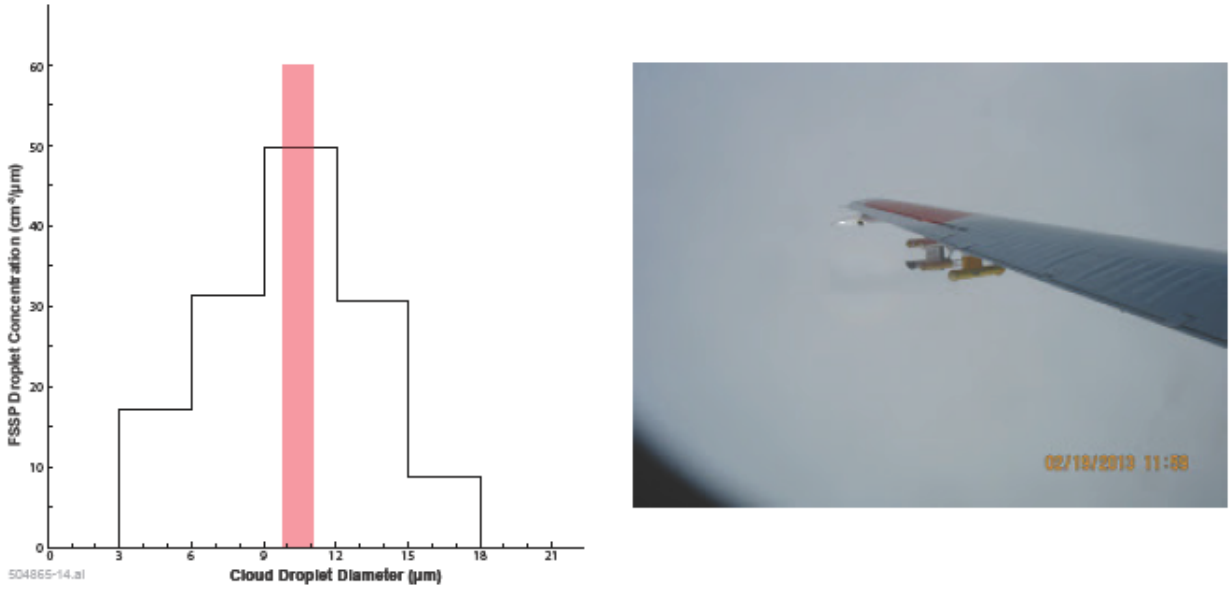

Figure 6-7. Cloud droplet spectra from the FSSP probe (left histogram) represent 30-second averages of 1-second spectra, normalized to 1 second. The red bar represents the estimated glory drop size for the image on right.

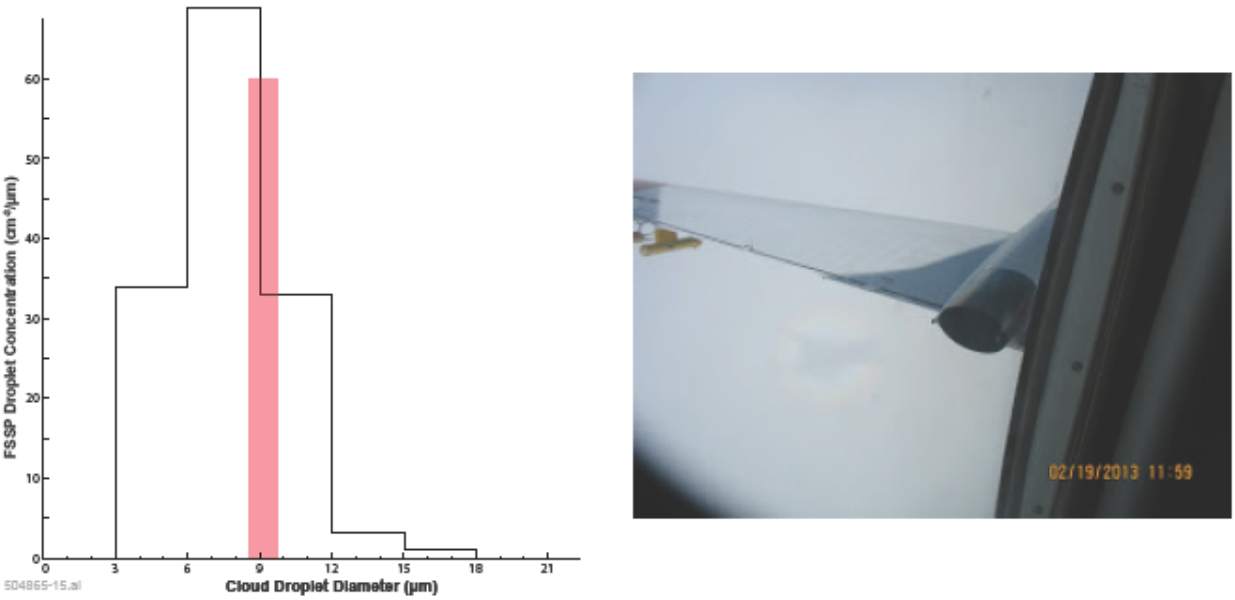

Figure 6-8. Cloud droplet spectra from the FSSP probe (left histogram) represent 30-second averages of 1-second spectra, normalized to 1 second. The red bar represents the estimated glory drop size for the image on right.

Another episode of SLW at much higher altitude and a lower in situ temperature (T = –20° C) occurred during the 10-minute interval 1620–1630 UT shown in Figure 6-9. The X-band radar on board the aircraft intermittently detected this event with very low returns (green line in lower panel of Figure 6-9). During this interval, there is also on occasion no return seen in the vertical W-band beam above the aircraft (Figure 6-2), so presumably this is a cloud turret close to the cloud top. According to the FSSP data at this time, the SLW is in cloud droplet form, with a median volume diameter in the range of 10–14 µm. Spheres and irregulars dominate the SNDI results. The 'spheres' are very likely tiny graupel particles. The HC is again predominantly 'Dry Snow.'

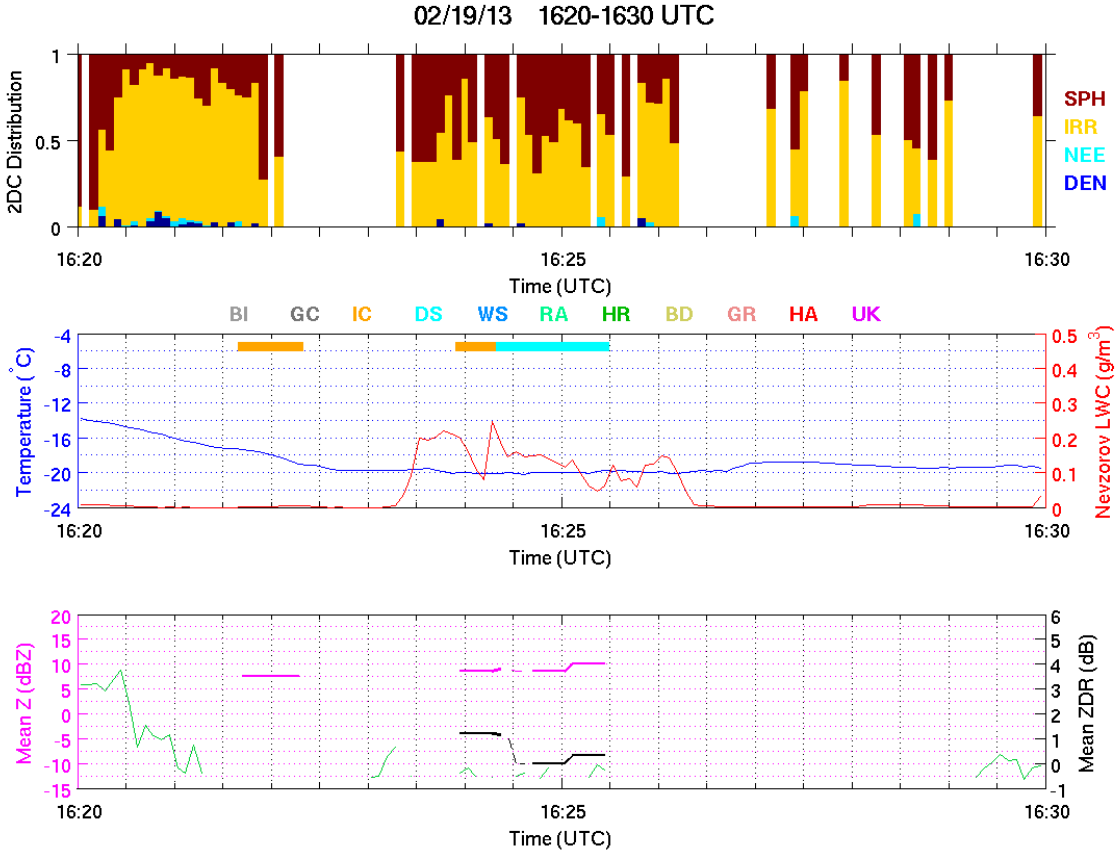

Figure 6-9. Ten-minute time series segment (1620–1630 UT) involving three-minute SLW episode at –20° C.

Analysis of the ground-based KBUF S-band observations (Figure 6-10) in a sequence of three separate PPI snapshots shows a delicate and transient narrow band oriented North-South a few kilometers east of where the SLW shows up at the aircraft location. We infer that ascent of cloud water is in close proximity to the reflectivity feature, and the absence of an S-band return where SLW is located with the

aircraft is consistent with the onboard X-band data. It is likely that insufficient time has been available for the formation of any radar echo in this case. The ZDR observations of the narrow feature (lower panels in Figure 6-10) show positive values, suggestive of the presence of horizontally oriented ice crystals.

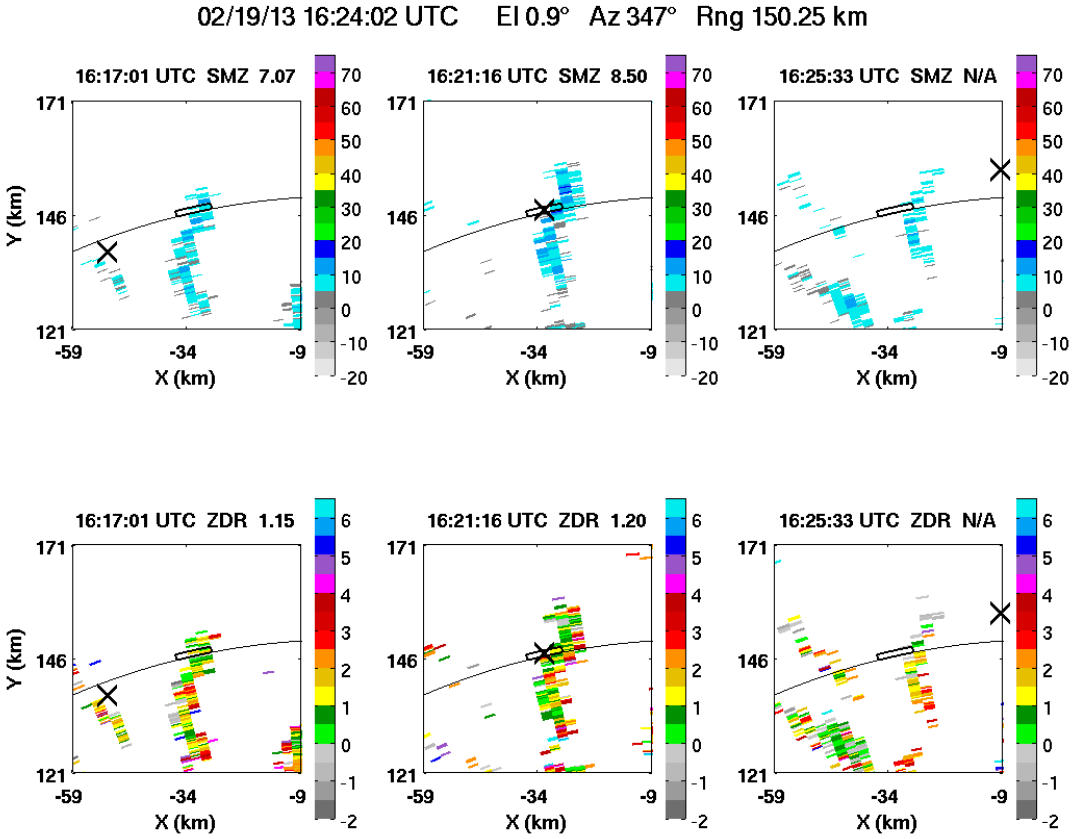

Figure 6-10. Three-panel plots of KBUF S-band radar reflectivity (top) and differential reflectivity (bottom) at three successive times to illustrate changes in parameters associated with the presence of SLW documented by the aircraft. The changing aircraft location with time (running from left to right in the plot sequence) is marked with a black X in each panel. The localized and transient nature of the radar return is consistent with the characterization of this event as a cloud turret.

The final analysis for the February 19 flight involves the comparison of radar mean reflectivity in comparison with the Nevzorov-measured SLW at the same location for all aircraft-radar comparisons matched within 120 seconds. These comparisons are shown in two plots, Figures 6-11 and 6-12. Figure 6-11 shows the corrected X-band reflectivity (see Appendix D for details on the correction of X-band measurements) versus the S-band reflectivity, with all points color-coded for supercooled water content in g/m^3. Figure 6-12 shows the same collection of data points, but now plotted to include the information on

differential reflectivity. The tendency for isotropic behavior (near zero ZDR) at the high reflectivity end is consistent with riming destroying the pristine crystals that produce the largest ZDR values. The presence of substantial positive ZDR values in the weaker reflectivity is consistent with a Bergeron process that is productive of highly anisotropic crystals, most likely the dendritic ones that grow fastest at water saturation.

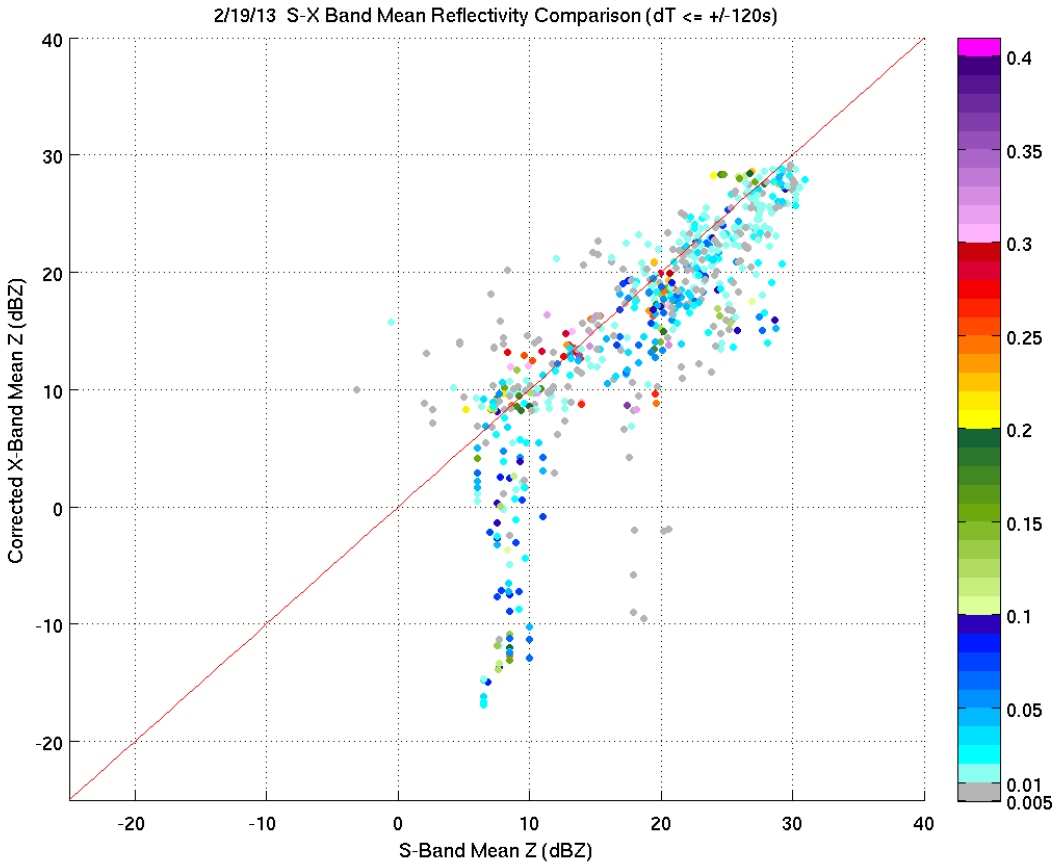

Figure 6-11. All five-second observations of corrected X-band reflectivity versus S-band reflectivity, but color-coded for Nevzorov probe-measured liquid water content in g/m^3.

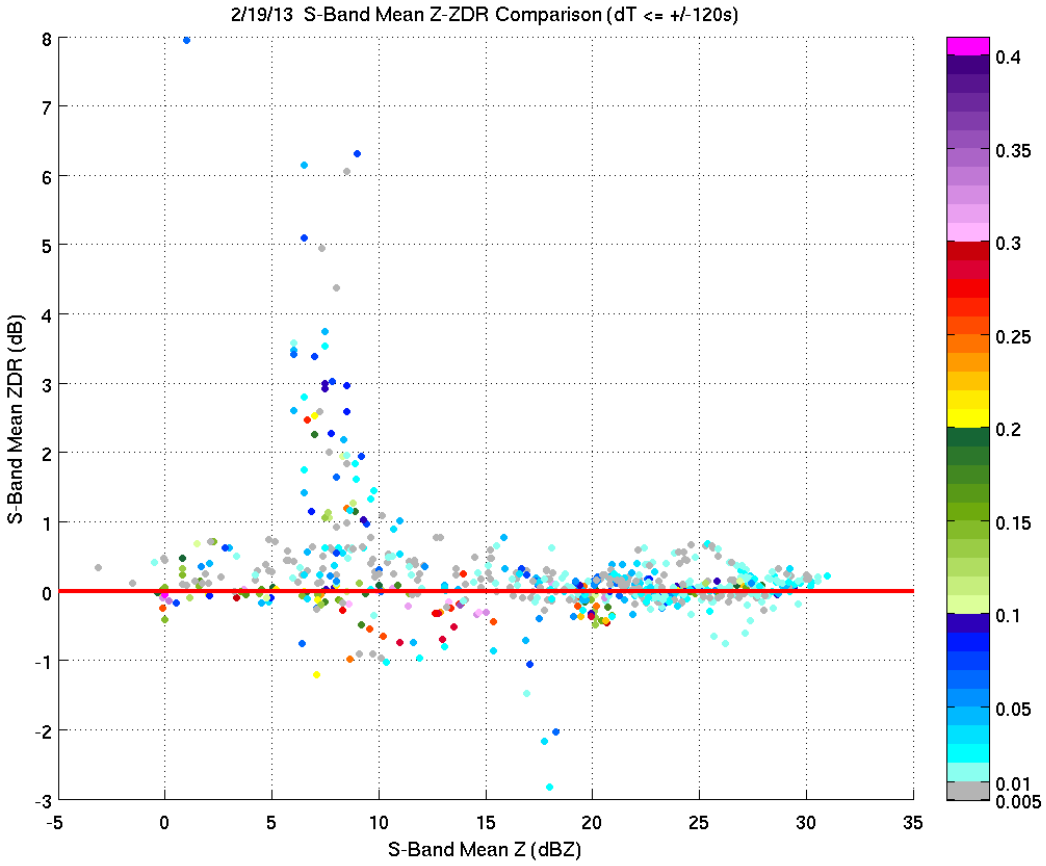

Figure 6-12. All five-second observations of S-band reflectivity versus differential reflectivity, with data points color-coded for Nevzorov probe-measured liquid water content in g/m^3.

The HCA category 'Dry Snow' has been problematic for this study because it does not allow conditions with and without SLW. For this flight in which 'Dry Snow' was by far the dominant HCA category, interest arose in checking all the NEXRAD dual pol parameters in a semi-controlled experiment in which in situ temperature was fixed and the Convair maintained constant altitude. The objective was to look for any changes in dual pol variables that would 'fingerprint' the SLW. Figures 6-13 and 6-14 both show time segments of this flight in which significant temporal variations in SLW are documented and in which in situ temperature, aircraft altitude, and HCA category are fixed quantities. No obvious correlated changes in dual pol variables SMZ, ZDR, KDP, or CC are noted here.

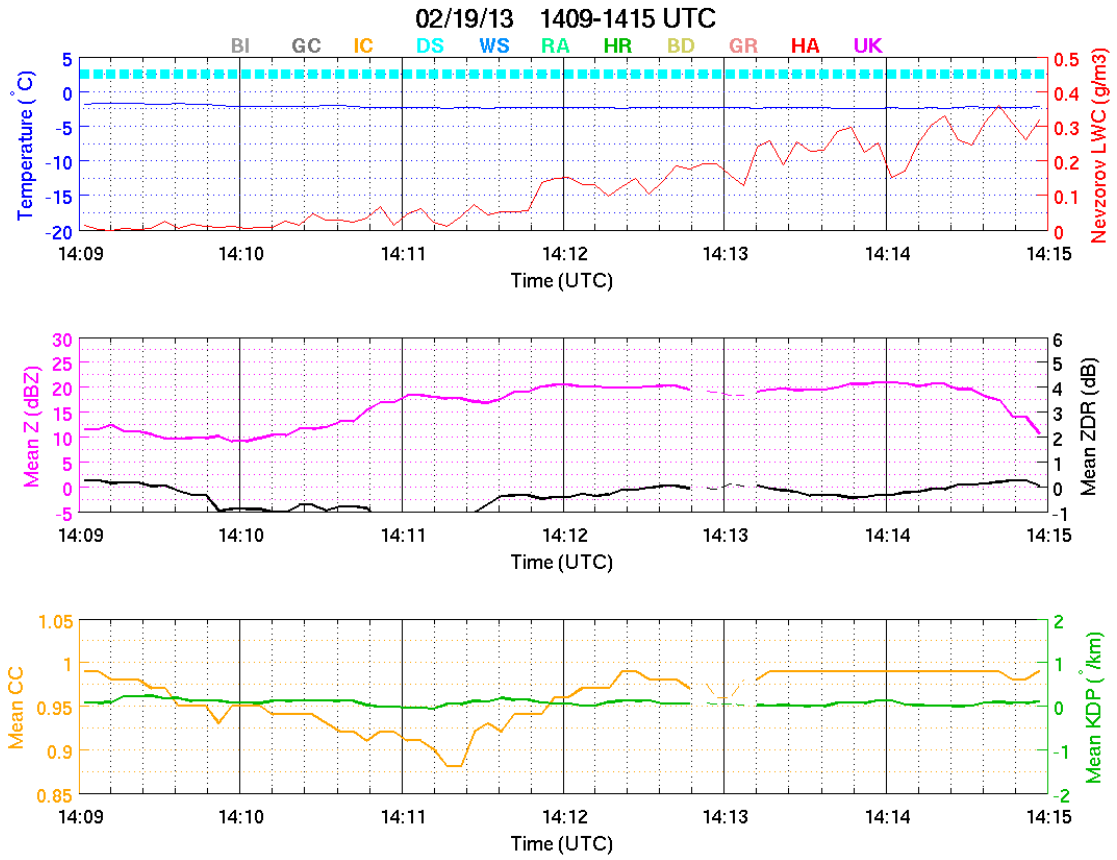

Figure 6-13. Time series segment from 1409–1415 UT showing SLW, temperature, and HC in the top panel, mean reflectivity (SMZ) and mean differential reflectivity (ZDR) in the middle panel, and correlation coefficient (CC) and specific differential phase (KDP) in the lower panel.

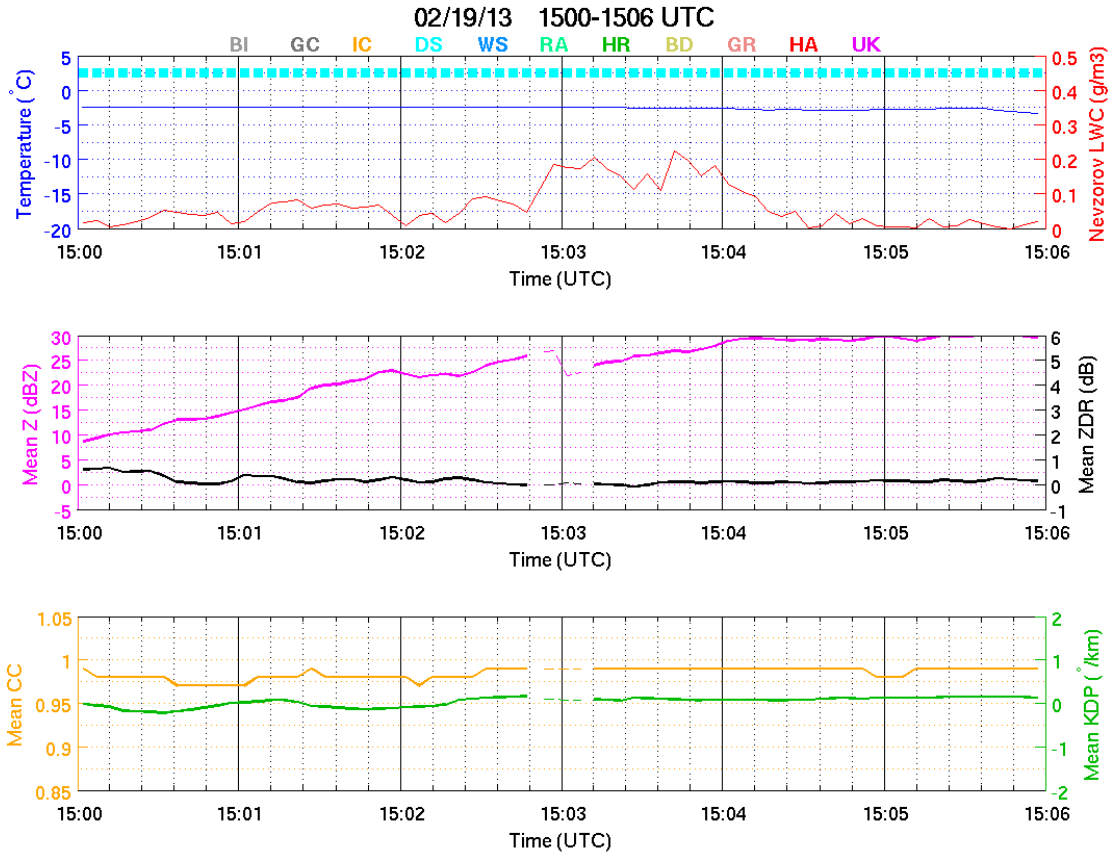

Figure 6-14. Time series segment from 1500–1506 UT showing SLW in the top panel, mean reflectivity (SMZ) and mean differential reflectivity (ZDR) in the middle panel, and correlation coefficient (CC) and specific differential phase (KDP) in the lower panel.

6.2 FEBRUARY 26–27, 2013 ('CLEAR ICING' FLIGHT)

This nighttime flight commenced at 2300 UT (Feb. 26) and returned to Ottawa by 0410 UT (Feb. 27). The plan view of this flight is shown in Figure 6-15. In contrast with the other two flights in which SLW was predominantly in cloud droplet form, in this case hazardous conditions were encountered with supercooled drizzle and with freezing rain. The latter circumstance gave this flight its name 'clear icing' case. Concerns were raised prior to the flight about the inability in nighttime conditions to see cloud layers of interest from the aircraft, but fortuitously, the meteorology on this day was not conducive to laterally extensive shallow layers. The nighttime context also prevented any observations of the glory from above the storm. This flight ranks as the most convective of the three, with 'Graupel' figuring prominently in the HCA (with verified detection in the PMS imagery) in the colder portions, consistent

with stronger vertical motions than is typical in snowstorms. This flight also serves to emphasize that supercooled drizzle, a verified radar target, is not currently categorized by HCA and remains difficult to distinguish from 'Dry Snow' in dual polarimetric observations because of its isotropic nature.

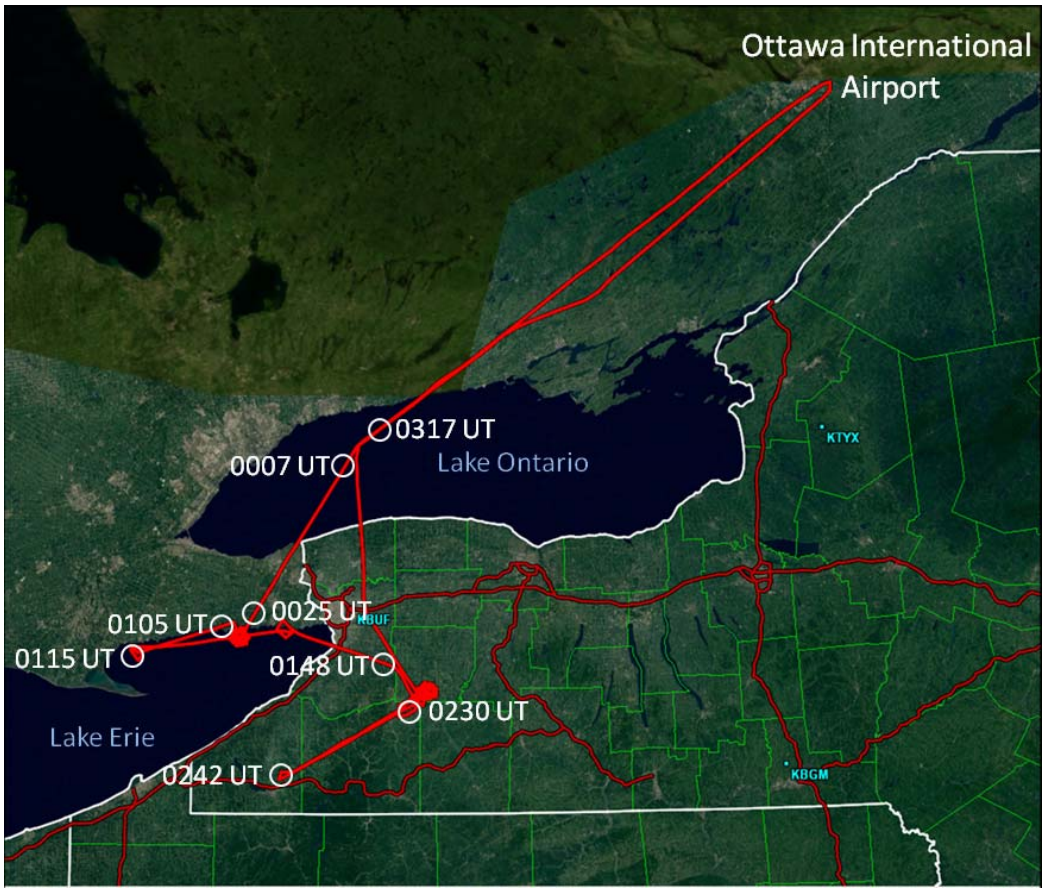

Figure 6-15. Plan view of the flight on February 26–27, originating in Ottawa at 2300 UT and completing there at 0410 UT on February 27.

Figure 6-16 shows the time-height plot for this flight (for the period 0015 to 0255 UT) that includes the continuously available onboard X-band radar observations in the vertical beam. The initial impression gained from this time-height presentation is that a laterally extensive conventional bright band is present. Comparison with the plan view of the overall flight in Figure 6-15, however, shows that localized spiral descents and ascents of the aircraft were undertaken in regions of interest identified by the real-time ground-based radar data to produce this time-height analysis. This situation will be further clarified as the description unfolds.

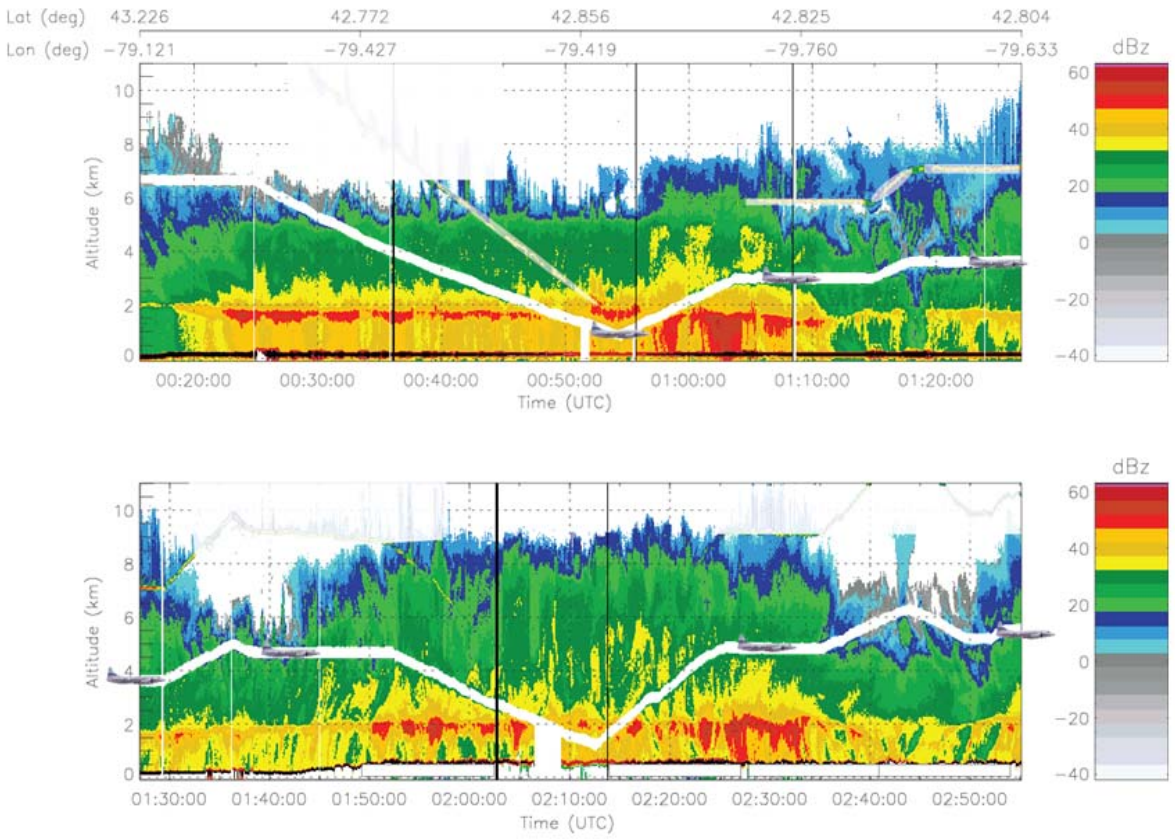

Figure 6-16. Time-height plot of the flight on February 27 in the time frame 0015–0255 UT with periods of supercooled drizzle and freezing rain that have been selected for more detailed discussion in the text.

The evidence that the laterally extensive reflectivity maximum in the time-height plot in Figure 6-16 is not a conventional bright band is shown by the aircraft soundings of temperature in both the descent and ascent portions of the top part of the time-height plot in Figure 6-16, as shown in Figure 6-17. Both down and up soundings show a 0° C crossing near 2000 m altitude, with 700-m-thick melting zone below that, and then a return to colder air below. Numerical model temperature soundings at this time also showed a large domain south of the aircraft location with three 0° C crossings with altitude. This is the so-called 'classical supercooled liquid drop' scenario (Cober et al., 2009) in which 'clear icing' hazard exists beneath the melting zone. The melting transition is responsible for the enhanced reflectivity evident in Figure 6-16 that has all the appearances of a conventional radar bright band. But the evidence here for liquid drops at sub-freezing temperature in this case (unlike the conventional radar bright band) is shown in the PMS 2DC imagery for the period 00:53:32 to 00:54:28 UT in Figure 6-18, in which some raindrops larger than 2 mm diameter are evident. Much surprise was registered by onboard scientists when these

drops appeared at sub-freezing temperatures, and some question was raised about the validity of the temperature measurements. The validity is now accepted. Some evidence for raindrop disruption during freezing may also be evident in the imagery (such as at 00:54:19 UT in Figure 6-18). The 10-minute time series segment in Figure 6-19 running from 0050 to 0100 UT encompasses the period of supercooling (to –3° C). The SNDI algorithm confirms the abundance of raindrops as 'Spheres' in the same time frame. The HCA (at the aircraft location) is correctly identifying 'Graupel' at altitudes above the zone of melting and refreezing, and is also correctly identifying 'Rain' (and occasional 'Big Drops'), even though these raindrops are supercooled (for which there is no category in HCA).

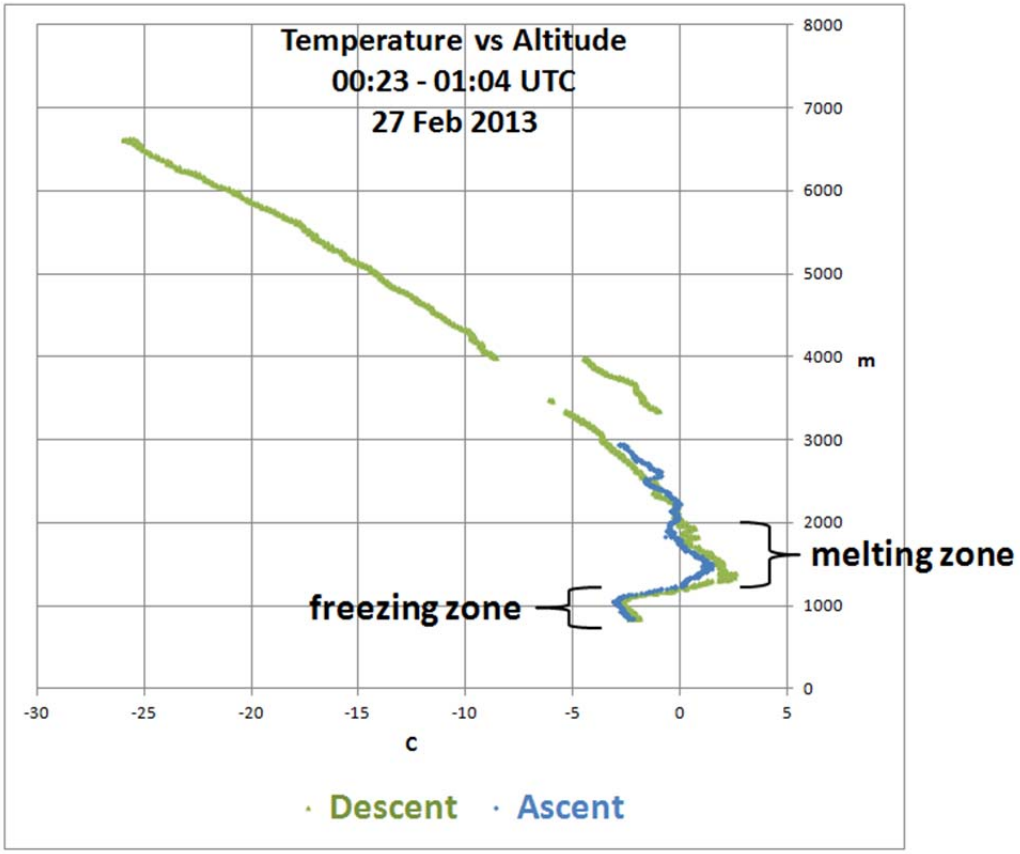

Figure 6-17. Convair-measured temperature during spiral descent and ascent during the upper period of Figure 6-16 on February 27, 2013.

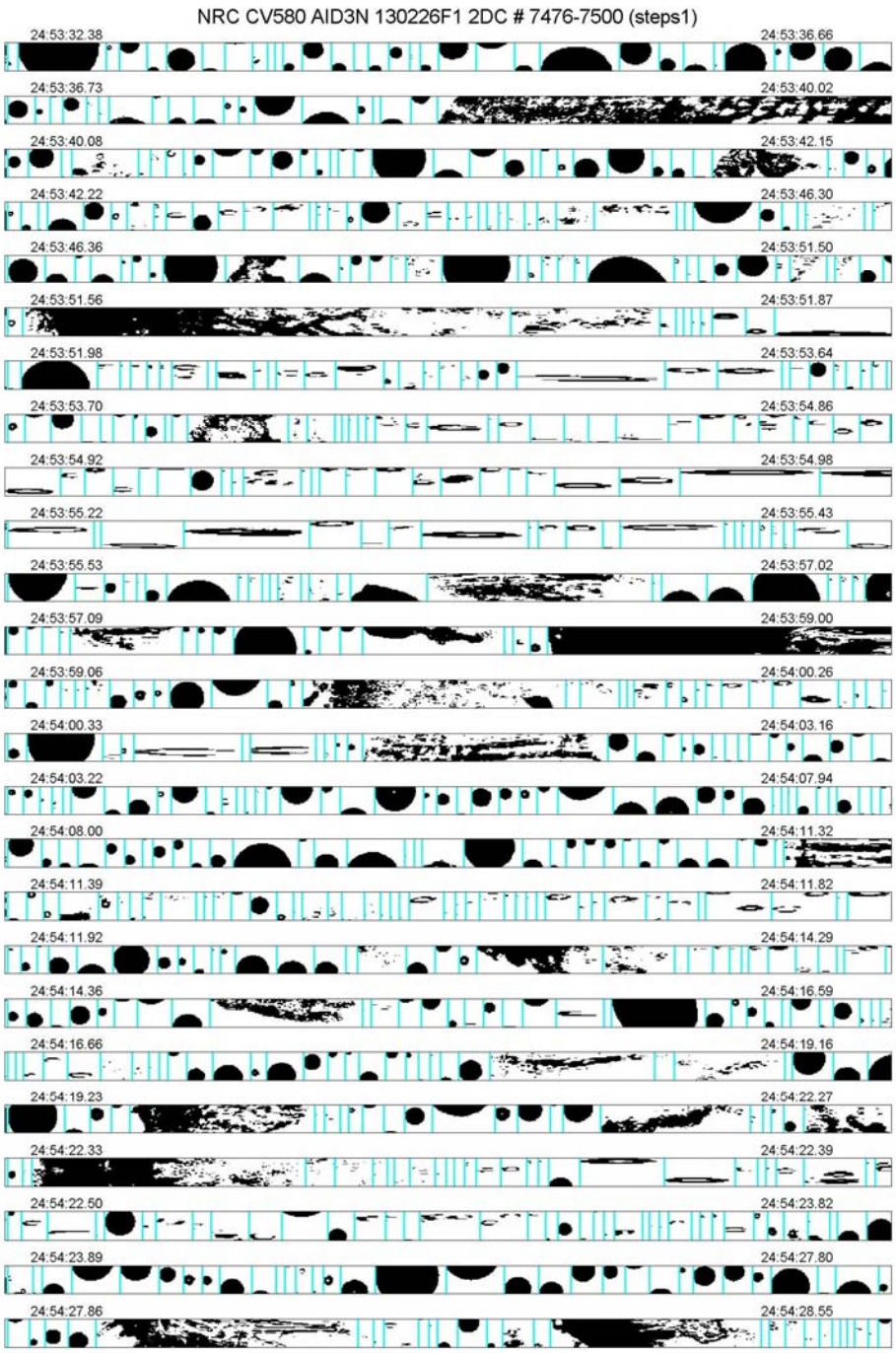

Figure 6-18. Imagery from the Particle Measuring Systems 2DC probe for the period 00:53:32 to 00:54:28 UT of supercooled freezing rain. The strip width is 800 microns. Raindrops in excess of 2 mm in diameter are clearly evident, as well as some possible evidence for the effects of raindrop freezing.

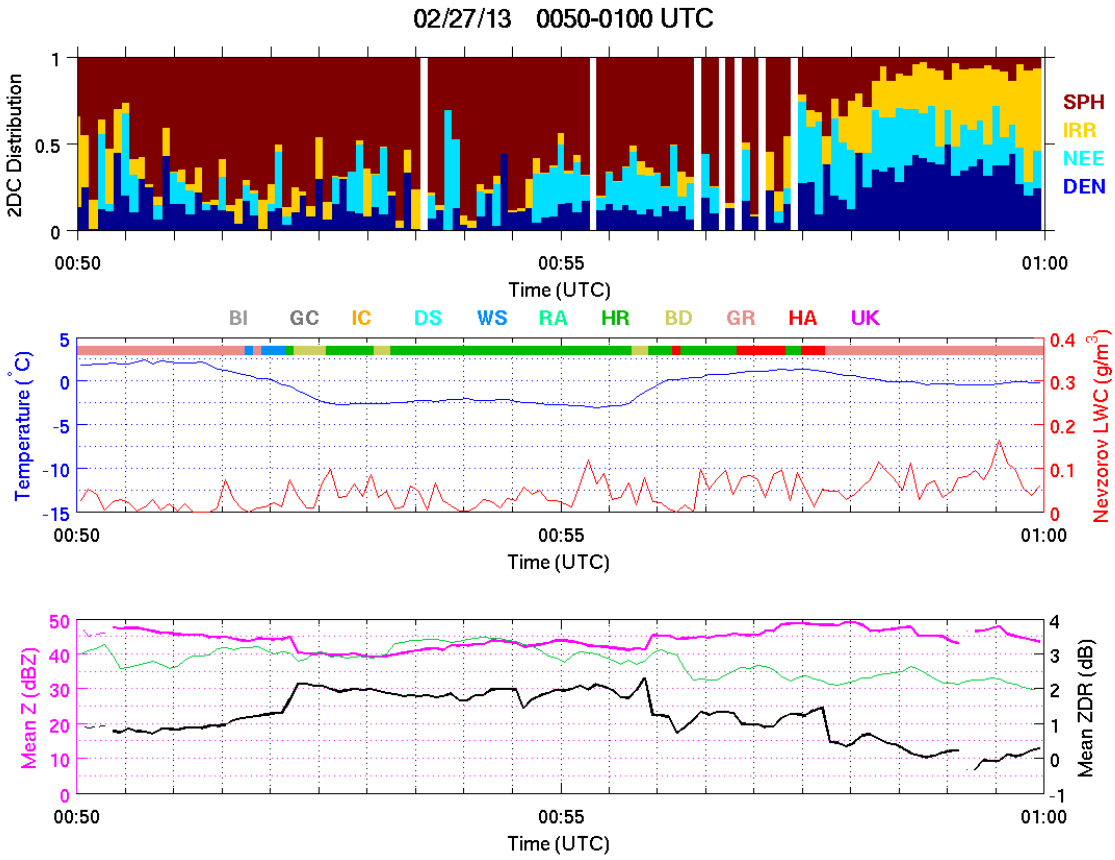

Figure 6-19. Ten-minute time series segment for the period 0050–0100 UT that encompasses the period of supercooled rain. 'Spheres' predominate in the SNDI algorithm (top). The differential reflectivity (ZDR) is elevated because of the oblate raindrops, and HCA correctly identifies 'Rain' and 'Large Drops' in this interval. 'Graupel' is also correctly identified at higher altitude, in time segments both before and after the period of supercooled rain.

Additional insight into HC for this case is possible in the display of KBUF radar data and HCA classification in PPI format for this time frame in Figure 6-20. The three panels here represent the SMZ (left), the ZDR (middle), and the HC (right). The white circles mark the heights of 0° C crossings recorded by aircraft in situ temperature, in this case at 1251 m and 1754 m, and bracket the melting zone. The location of the Convair at this time is between the two white circles and at a radar azimuth of about 265°. Consistent with earlier remarks that the horizontal feature in Figure 6-16 is a localized one, no obvious manifestation of a conventional radar bright band is evident in the PPI of radar reflectivity. Again, 'Graupel' is correctly identified at altitudes above the melting zone. The melting of the graupel and attendant increase in dielectric constant is causing large (>50) dBZ south of the aircraft location, and leading to 'Hail' identification that we cannot validate. The 'Rain' in the melting zone we did validate.

The ‘Rain’ in the supercooled zone within the inner white ring, where ZDR is also enhanced, we also validated, but note again that HCA has no separate category for this class of hydrometeor (supercooled rain).

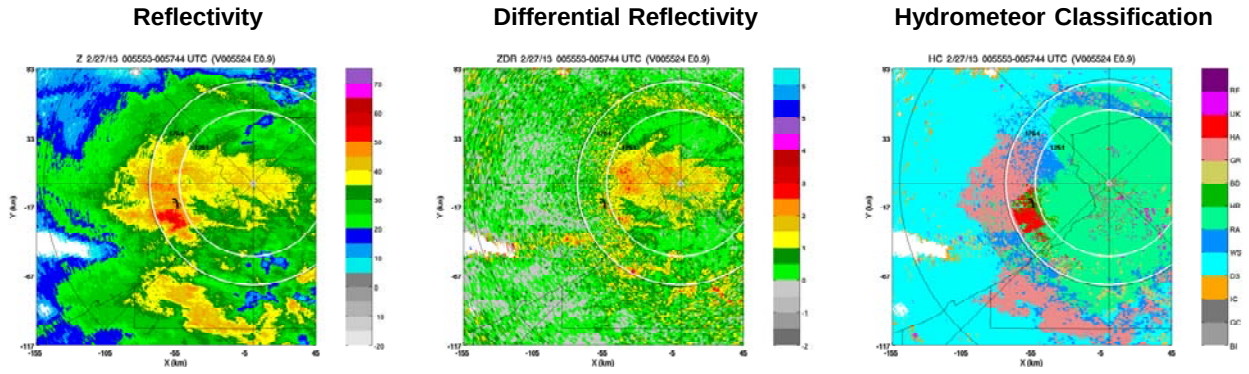

Figure 6-20. PPI displays of KBUF NEXRAD SMZ (left), ZDR (middle), and HC (right) for the first Convair descent (00:55:53 to 00:57:44 UT) through a melting zone and refreezing zone. The white circles delimit the melting zone on the basis of aircraft in situ temperature readings.

Following the ascent of the Convair out of this zone of supercooled rain in the interval 0100–0115 UT (see Figure 6-16), the aircraft encountered a zone of supercooled drizzle and maximum in SLW (~0.3 g/m^3). Figure 6-21 shows the 10-minute time series segment from 0110–0120 UT. The increase in Nevzorov LWC starting around 0115 UT is accompanied by a systematic increase in the ‘Spheres’ category in the SNDI algorithm, which shows essentially 100% ‘Spheres’ by 0118 UT, where the in situ temperature has leveled off to T = –9° C. The corresponding 2DC imagery is shown in Figure 6-22. The confidence that the ‘Spheres’ are liquid water drops rather than quasi-spherical graupel particles is found in the FSSP imagery (not shown) at this time showing a strong tail beyond 40 µm diameter, the threshold for active collision-coalescence.

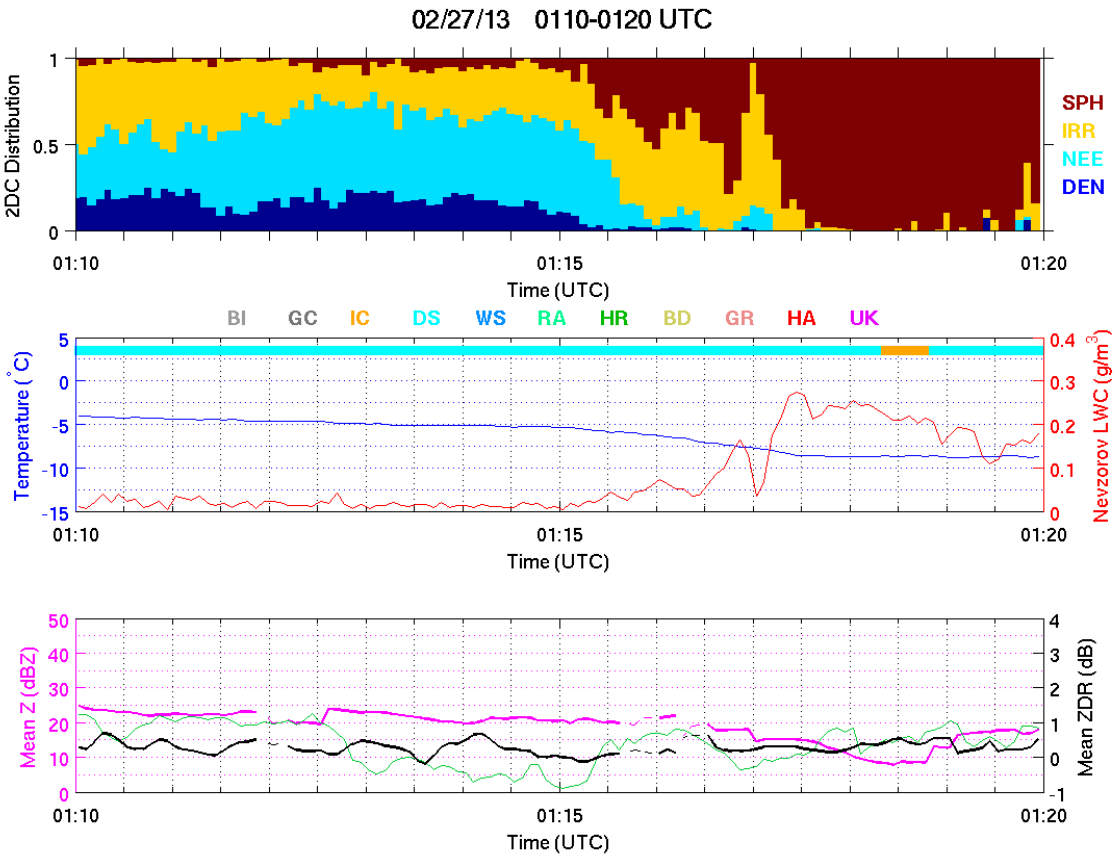

Figure 6-21. Ten-minute time series segment for the interval 0110–0120 UT, showing evidence for enhanced supercooled water content on the Nevzorov probe and an increasing population of 'Spheres' in the SNDI algorithm. The predominant HCA identification is 'Dry Snow,' and this is incorrect.

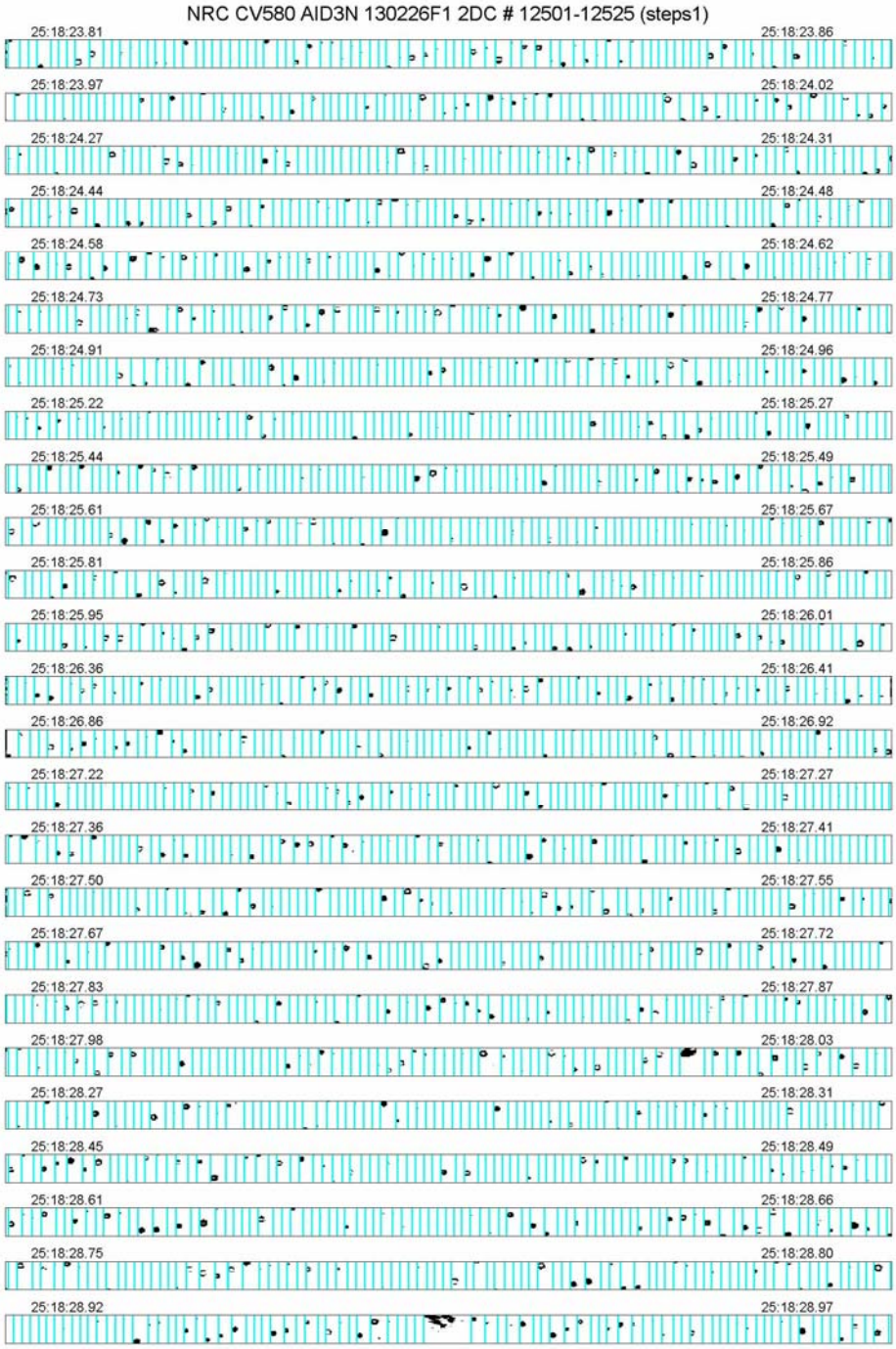

Figure 6-22. Imagery from the Particle Measuring Systems 2DC probe for the period 01:18:23 to 01:18:28 UT, showing evidence for supercooled drizzle drops with sizes in the 100–300 µm, and no larger hydrometeors.

This episode of inferred supercooled drizzle has been examined further in 4D analysis with PPI scans at three separate times in Figure 6-23. The aircraft is engaged in a counterclockwise maneuver in this overall time interval, explaining the absence of a monotonic progression of the X in one direction. But in a region sampled by the aircraft and in which supercooled water is present, a noticeable increase in radar reflectivity with time is noted. This is the enlarging area of green (20–25 dBZ) just north of the rectangle center. No obvious changes in ZDR (lower three panels in Figure 6-23) in the same general area are noted.

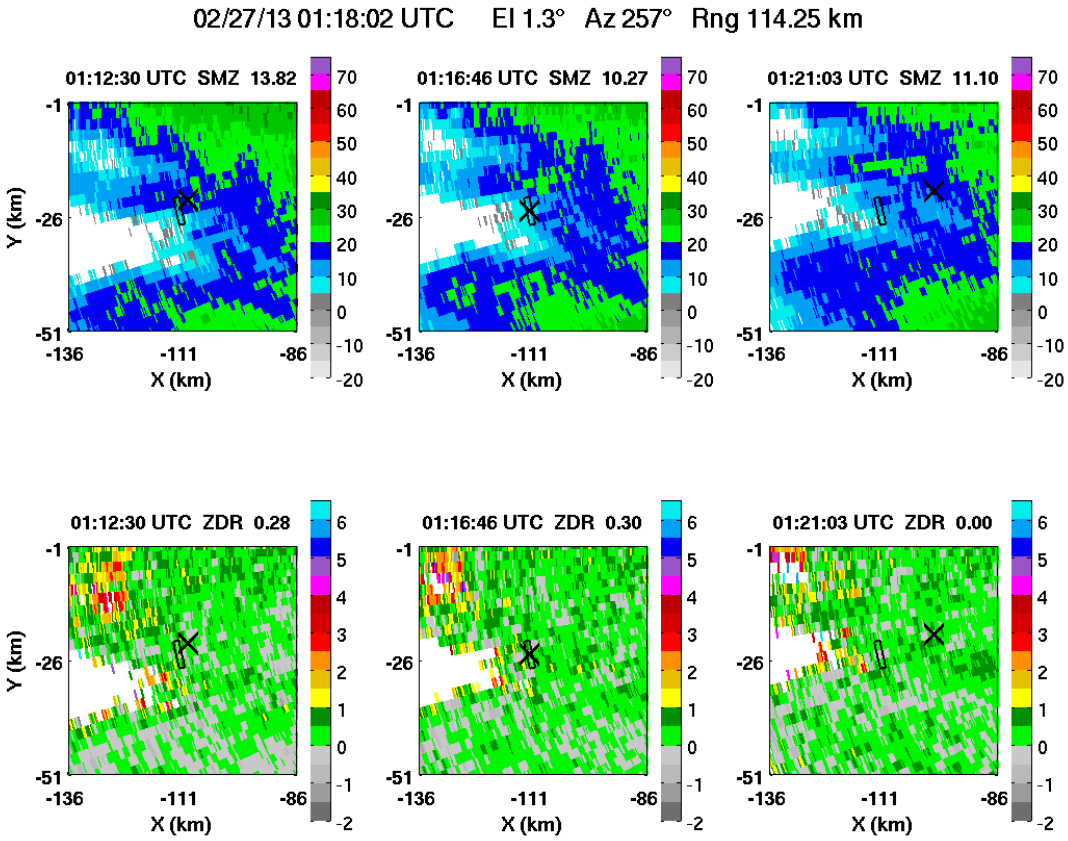

Figure 6-23. Four-dimensional analysis of the supercooled drizzle episode, in both reflectivity (SMZ, top panel) and differential reflectivity (ZDR, bottom panel), with PPI scans at 01:12:30 UT, 01:16:46 UT, and 01:21:03 UT, and also shown in the 10-minute time series plot in Figure 6-21. The Convair location is indicated by a black X as in prior figures. The black rectangle shows the location where the mean quantities in the upper right corner are calculated. Growth of the reflectivity feature just northeast of the aircraft location is evident in the 2nd and 3rd PPIs.

As shown in Figure 6-16, following this encounter with supercooled drizzle, the Convair spirals down again through the melting/freezing zone in the time interval 0152–0212 UT. Note here that in the vertical beam of the X-band radar, the storm has deepened considerably (to 8–9 km), in comparison with the earlier period with cloud tops at 6–7 km. But the height of the reflectivity maximum at lower altitude is remarkably the same, even after a period of more than an hour of elapsed time. The model results at this time show a large area around the KBUF radar in which triple 0° C crossings in the temperature soundings are evident, providing additional evidence for the persistence of a hazardous condition for aviation.

The 10-minute time series segment encompassing the aircraft traversal of the sustained melting and freezing zone is shown in Figure 6-24 for the period 0210–0220 UT. The period near the beginning of the record when the aircraft experiences sub-freezing temperatures (to T = –4° C) also coincides with an interval in which liquid drops are in evidence in the 2DC imagery, as shown in Figure 6-25. In contrast with the earlier freezing rain episode documented earlier, in this case ground-radar-based HCA is identifying 'Graupel' rather than 'Rain' in the freezing zone. Further insights into the workings of the HCA are achieved by repeating the radar analysis of Figure 6-20 for the first freezing rain episode, in Figure 6-26. Here the 0° C crossings from the in situ temperature have been updated to this time to make the white circles in this figure. Like the model evidence for more extensive triple crossings of 0° C in the temperature sounding, and consistent with the deeper storm structure found from the Convair, the reflectivity distribution is more closely centered on the KBUF radar at this later time. As with the earlier episode, no obvious conventional bright band symmetry is evident in the reflectivity field of Figure 6-26. The aircraft location in this time frame is now in the southeast quadrant of the KBUF radar. Consistent with the information in Figure 6-24, the prevalent HCA category in Figure 6-26 both above and below the altitude of the aircraft is 'Graupel,' with some more minor areas of 'Wet Snow.' The graupel above the aircraft location is verified in the 2DC particle imagery (not shown), but the missed 'Rain' below the melting zone may be an error in the model temperature field used by the HCA. Consistent with the HCA sticking with 'Graupel' below the inferred melting zone, the differential reflectivity in Figure 6-26 does not become enhanced for some distance below the melting zone.

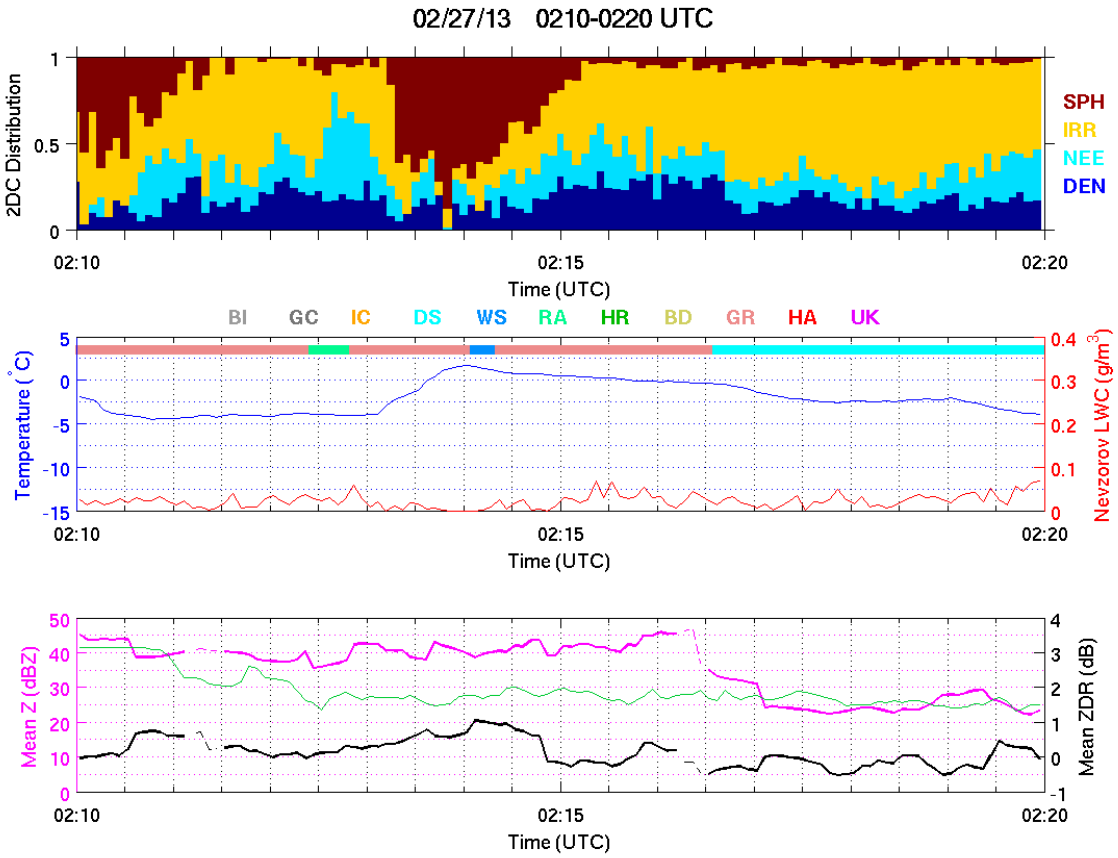

Figure 6-24. Ten-minute time series segment for the interval 0210–0220 UT, just as the aircraft descends into the supercooled raindrop zone and during which the SNDI algorithm is identifying 'Spheres.' But HCA is identifying 'Graupel' in this time window, in contrast to 'Rain' as in the earlier freezing rain episode.

Figure 6-25. Imagery from the Particle Measuring Systems 2DC probe for the period 02:09:57 to 02:10:44 UT, showing an abundance of raindrops with sizes in excess of 1 mm diameter in a zone of freezing temperature (T = 0° to –4° C).

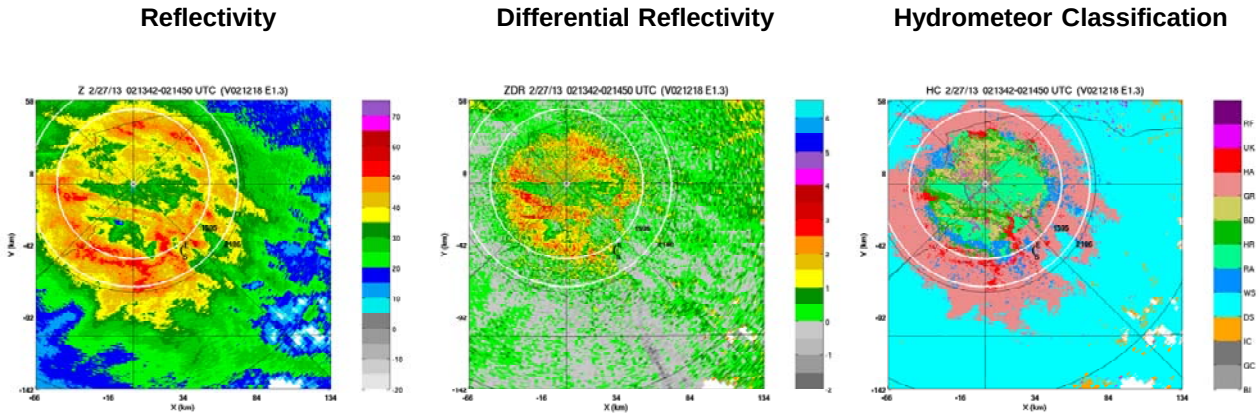

Figure 6-26. PPI displays of KBUF NEXRAD smoothed reflectivity SMZ (left), differential reflectivity ZDR (middle), and HC (right) for the second Convair descent (02:13:42–02:14:50 UT) through a melting zone and refreezing zone. The white circles delimit the melting zone on the basis of aircraft in situ temperature readings.

The final item of note for this flight is the evidence for the so-called +ZDR 'bright band,' a phenomenon identified in earlier studies with ground-based dual pol radar observations alone (Kennedy and Rutledge, 2011; Williams et al., 2011; Williams et al., 2015). One example of this ring of enhanced differential reflectivity in a PPI at 15.6° elevation angle of KBUF is shown in Figure 6-27 at 0130 UT. The altitude of the 'bright band' is 4.9 km and so above the altitude of the Convair for the majority of flight time shown in Figure 6-16. Careful examination of the entire sequence of KBUF imagery indicates that this bright band was present for the majority of this flight, but because of the initial indication of icing hazard and the interest in the supercooled rain at lower altitudes, our exploration of this upper level feature was unfortunately neglected. A chance encounter occurred when the aircraft intersected the height of the +ZDR bright band on descent from higher altitude (see Figure 6-16), and the in situ conditions are documented in the 10-minute time segment for 0030–0040 UT (Figure 6-28). This evidence serves as verification of a 'Category A' condition and presence of supercooled water inferred from dual pol observations (Williams et al., 2015).

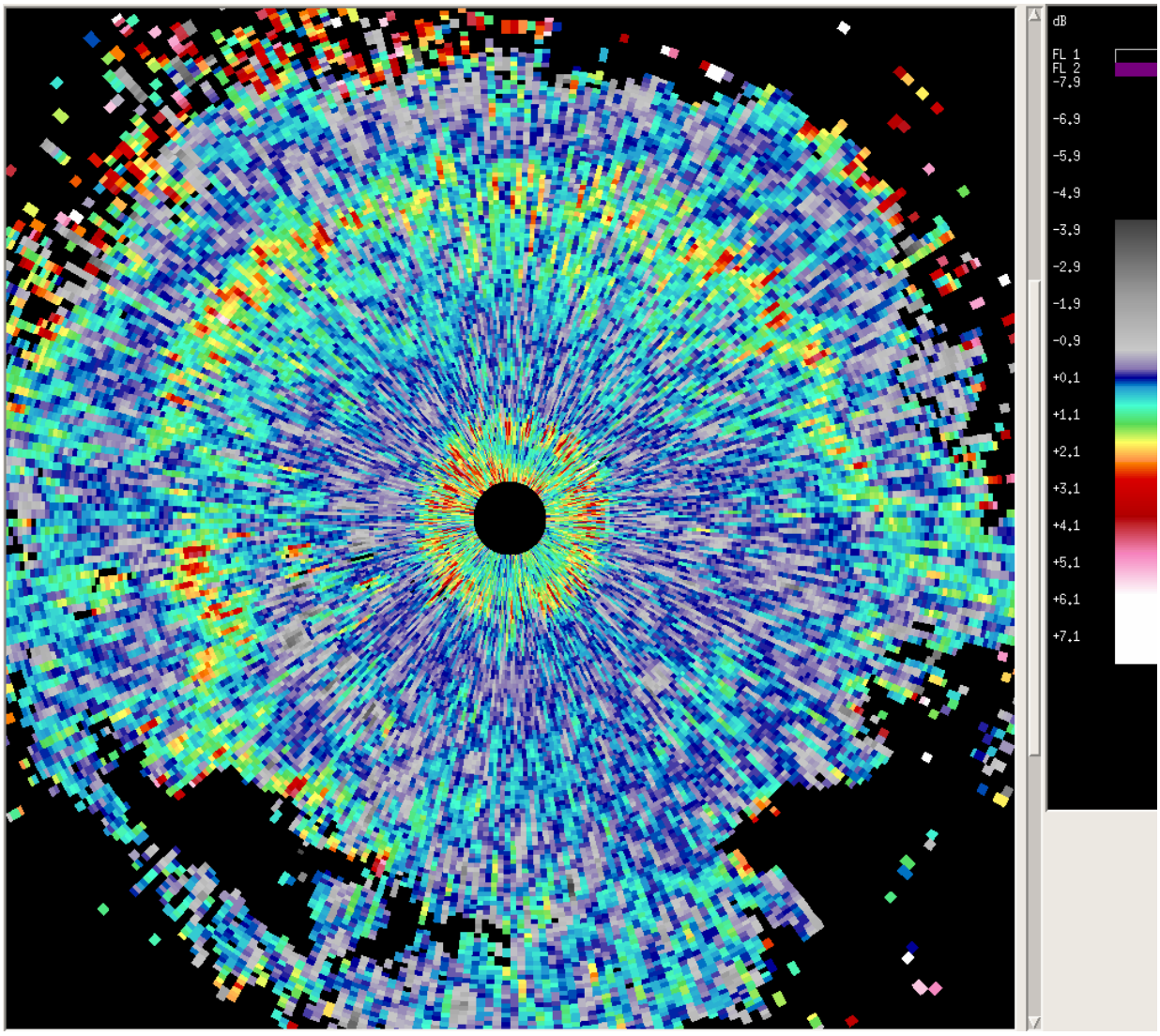

Figure 6-27. KBUF PPI scan of differential reflectivity at 15.6° elevation angle at 0130 UT, showing evidence for a +ZDR 'bright band,' nearly encircling the radar location.

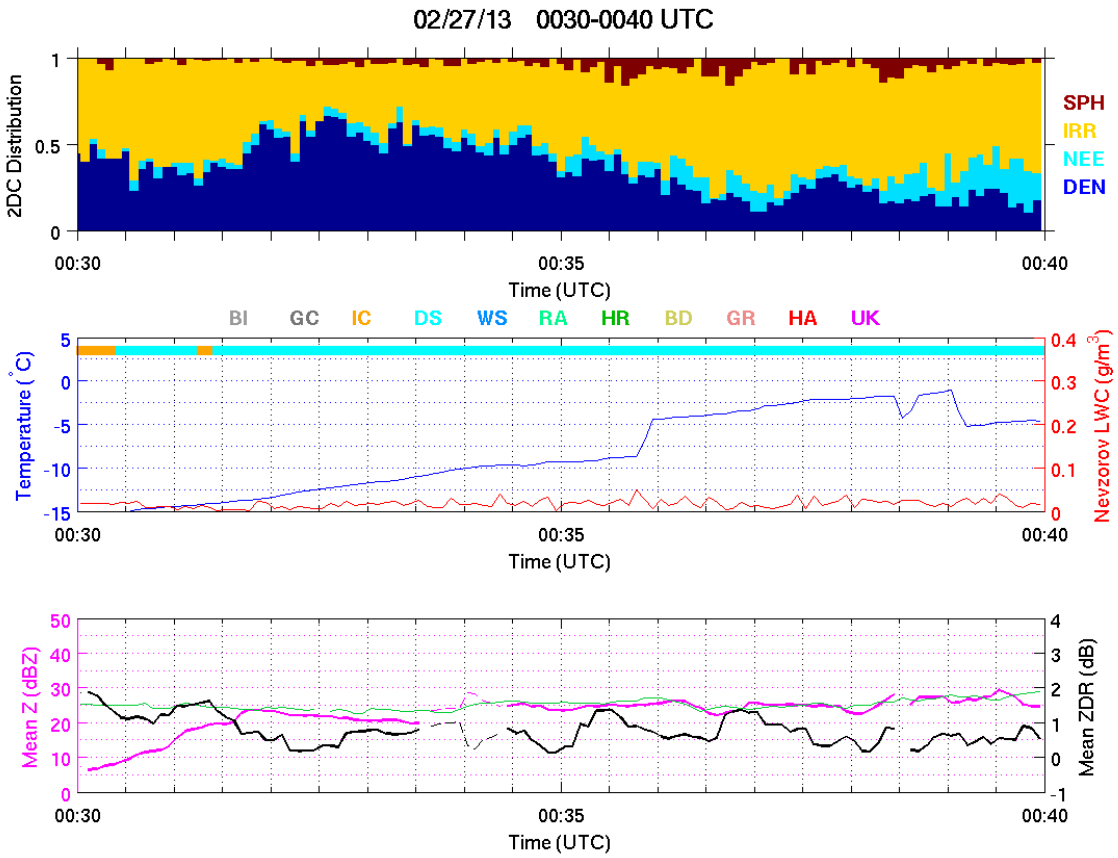

Figure 6-28. Ten-minute time series segment for 0030–0040 UT depicting the time interval of aircraft descent through the region identified in high-level radar PPI scans as the +ZDR 'bright band.' Note the evidence for an abundance of dendritic crystals, and the continuous presence of SLW, when the in situ temperature is in the range of –10° to –14° C.

6.3 FEBRUARY 28, 2013 ('HEXAGONAL FLAT PLATE CRYSTAL' FLIGHT)

This daytime flight began in Ottawa at local noontime (1700 UT) and was completed by 2050 UT (flight path in Figure 6-37). This was the most gentle snowstorm of the three explored by the Convair in February 2013, and that aspect may be largely responsible for its most remarkable feature: quasi-uniform populations of specific ice crystal types (needles, dendrites, and plates) were observed in thermodynamic conditions broadly consistent with the findings in laboratory diffusion chamber measurements, as discussed in Section 2.2 and illustrated by Figure 2-2. As discussed in an earlier study of this flight (Williams et al., 2013), the most remarkable crystals observed in abundance were the hexagonal flat plates, a relatively rare crystal type in previous aircraft measurements, and from this the flight got its

name. The thermodynamic linkage of all three prominent crystal types with a water saturation condition, and the tendency for the same crystals to provide strong positive response in differential reflectivity measurements, together serve to provide a fingerprint for supercooled water in weak reflectivity environments.

Three factors contributed to perhaps the most successful flight of the campaign: (1) the ground-to-aircraft communication and transfer of KBUF NEXRAD radar information to the Convair worked continuously, (2) the KBUF radar was operating in the sensitive clear air scanning mode providing greater sensitivity to the weak radar targets (oftentimes with negative dBZ values) exhibited by the ice crystal populations, and (3) a 'porpoising' maneuver was adopted with the Convair as a distinct departure from the tracks at fixed altitude, and this proved exceedingly valuable in exposing the layered structure of supercooled water and quasi-uniform ice crystal populations.

The role of 'porpoising' in disclosing the organization of the February 28 storm into layers of large horizontal extent is illustrated by the time-height plot for this flight, using the onboard W-band radar data, as shown in Figure 6-29 over the period 1750–1950 UT. As the aircraft approached the region northwest of the KBUF radar and at high (4–5 km) altitude for further probing, the glory was evident looking down on the storm top, as shown by the photograph in Figure 6-30. That was the first evidence of the flight for the presence of supercooled water in cloud droplet form in the storm below. As porpoising continued, the PMS particle probes showed evidence for consistent alternation between needle crystals at low altitude and higher temperature (T = –4° to –5° C) and hexagonal flat plate crystals at higher altitude and lower temperature (T = –9° to –11° C). This repeated behavior along a flight track covering tens of kilometers is evidence for layering of both the crystal types and the supercooled water.

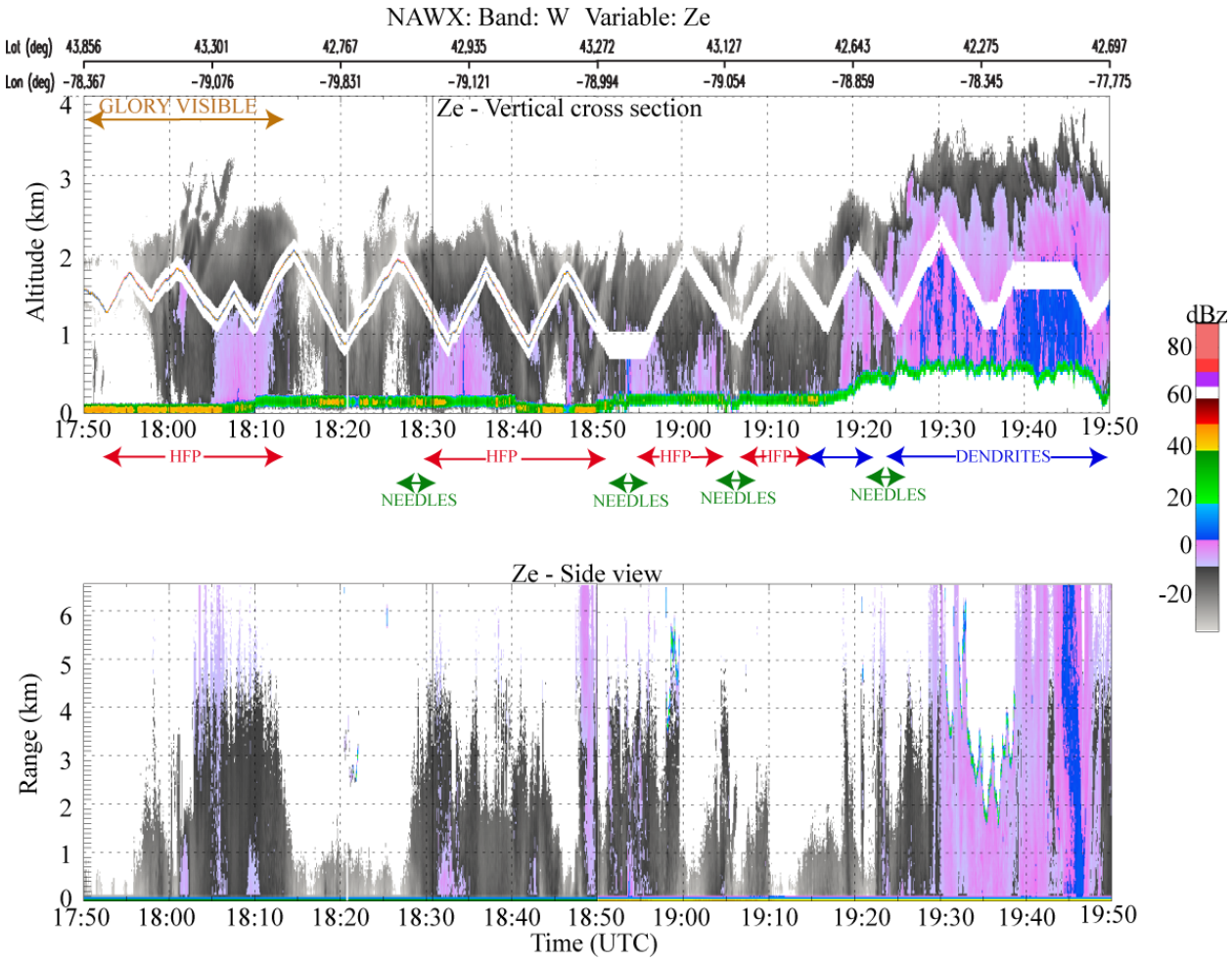

Figure 6-29. Time-height history of aircraft W-band reflectivity for the February 28 flight, showing the triangular pattern of the altitude changes associated with 'porpoising,' and the evidence for repetition in dominant crystal types with altitude and in situ temperature. The early period of glory observations is also marked here.

Figure 6-30. Photograph of the glory and the shadow of the Convair in its center at 1811 UT. The presence of the glory in a cold cloud top is direct evidence for supercooled cloud water in monodisperse droplet form.

The first period of abundant hexagonal flat plate crystals is noted in the top panel of Figure 6-29. A better look at the behavior of the Nevzorov supercooled water content is documented in the 10-minute time series segment in Figure 6-31 for the period 1800–1810 UT. Hexagonal flat plates (HFPs) are the dominant crystal in the 2DC imagery (shown in Figure 6-32), but the trace of liquid water content is intermittent in the same period. The FSSP data indicate that the SLW is in cloud droplet form, as there is no strong tail in the distributions at large cloud droplet sizes. The SNDI algorithm (top panel in Figure 6-31) is showing 'Spheres,' but the evidence from the raw 2DC imagery is that the HFPs are masquerading as 'Spheres' in that algorithm. Note the SNDI algorithm struggles with a majority identified as 'Irregulars.' The large ZDR values evident in Figure 6-31 (+2 to +4 dB) are consistent with the presence of the highly anisotropic HFPs, but the Hydrometeor Classification Algorithm is incorrectly

identifying these hydrometeors as ‘Unknowns.’ Hexagonal flat plate crystals may also wind up in the ‘Irregular’ category.

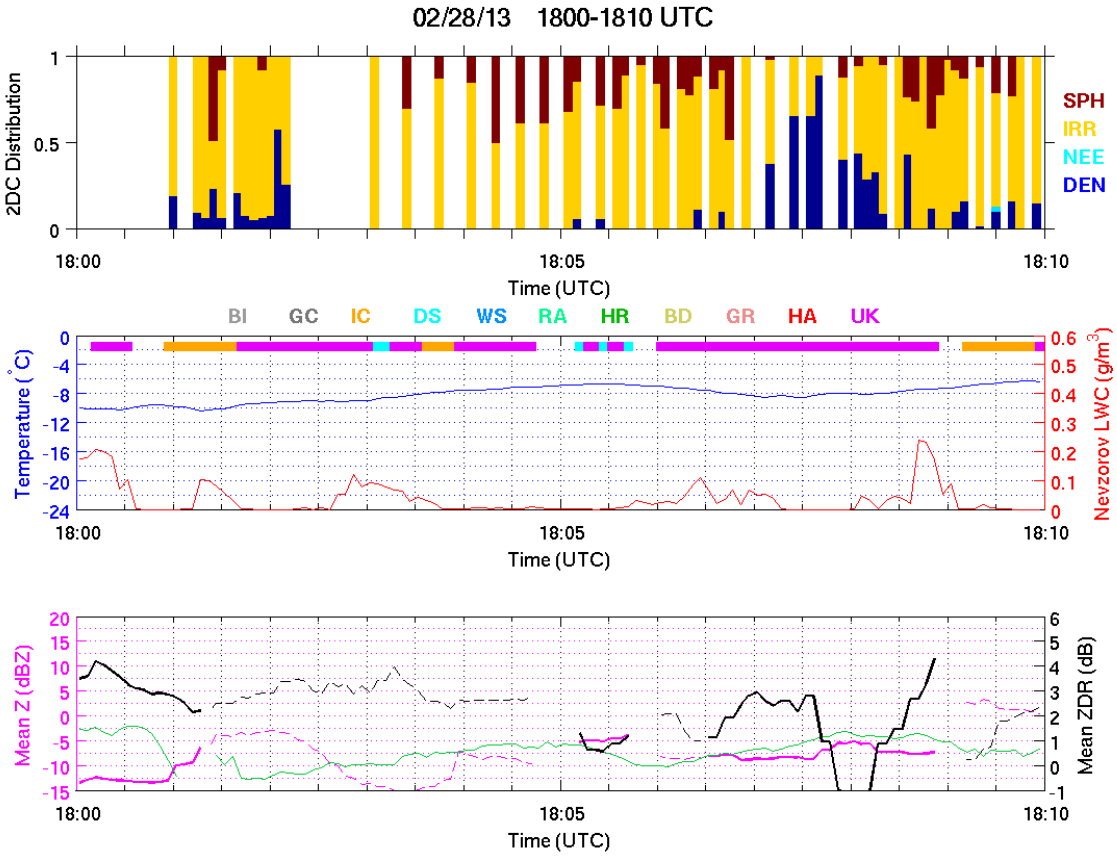

Figure 6-31. Ten-minute time series segment for the interval 1800–1810 UT when hexagonal flat plate (HFP) crystals are prevalent, the SNDI algorithm is reporting predominantly ‘Irregulars,’ and when the hexagonal crystals are likely masquerading as ‘Spheres’ to explain the 15–40% of the SNDI output in that category. The HCA is reporting primarily ‘Unknowns,’ and despite the expected large ZDR values in this interval (+2 to +4 dB), still not identifying the HFPs as ‘Ice Crystals’ as it should.

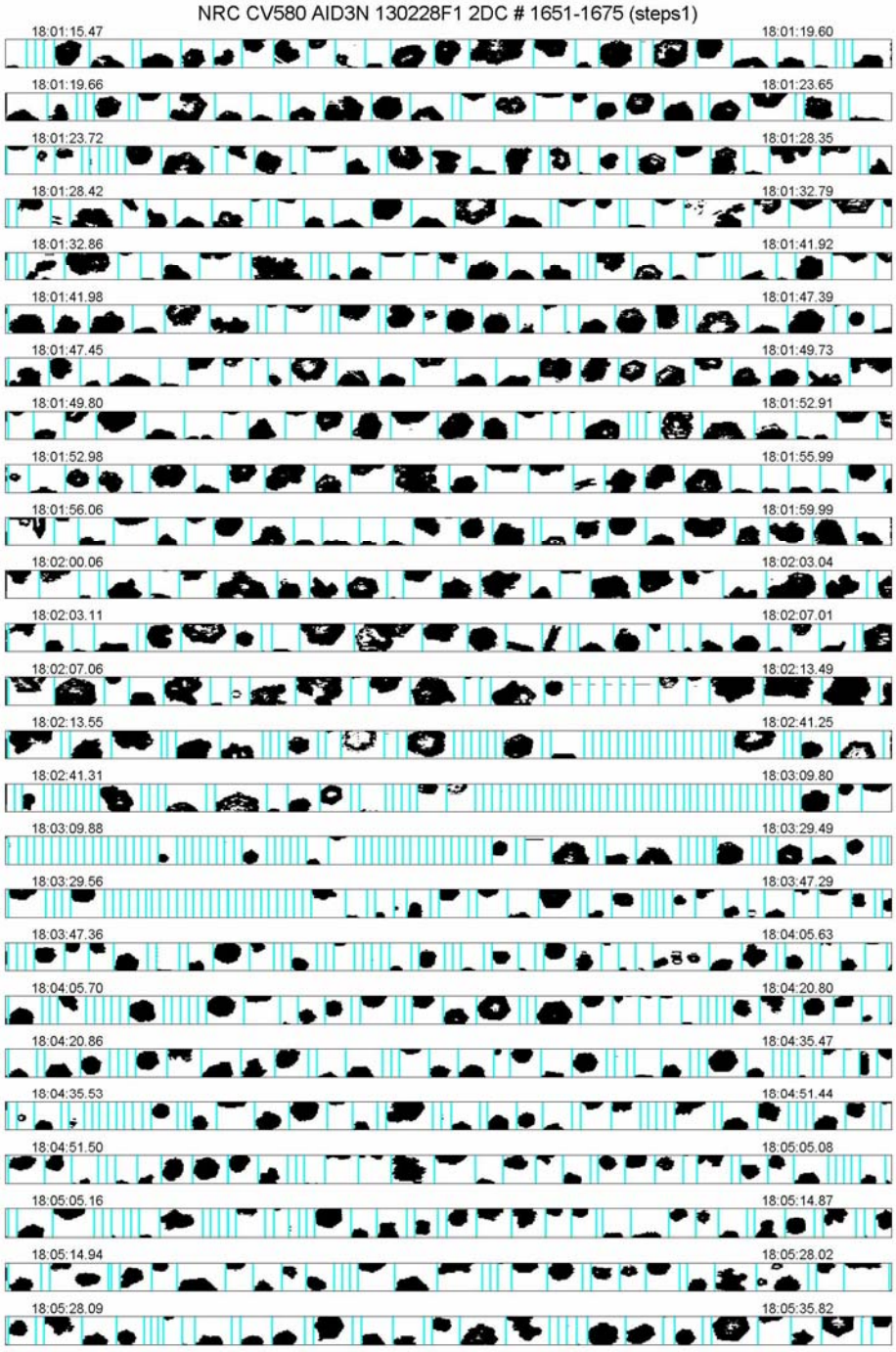

Figure 6-32. Imagery from the PMS 2DC probe for the period 18:01:15 to 18:05:35 UT showing a great dominance of hexagonal flat plate (HFP) crystals with diameters in the range of 400–1200 µm. Comparison with Figure 6-31 suggests that the HFPs are occasionally masquerading as 'Spheres' in the SNDI algorithm.

The most conspicuous maximum in SLW for this flight, and indeed one of the largest maxima for all three flights, occurred during the 10-minute time interval 1830–1840 UT, as shown in the time series plot in Figure 6-33. The maximum supercooled water content exceeds 0.5 g/m^3. As shown in Figure 6-29, this time interval involves the aircraft ascent from a warm region (T = –4° to –5° C) with needles (and indeed the SNDI algorithm identifies needles at that time, as the top panel of Figure 6-33 shows) into a colder region dominated by HFPs (when the SNDI algorithm is showing a higher percentage of 'Spheres' and when the HCA is identifying 'Unknown' for the plates). The maximum in LWC at 1834 UT coincides with rather abrupt transition from needles to plates, when the concentration of large crystals of either type is at a minimum.

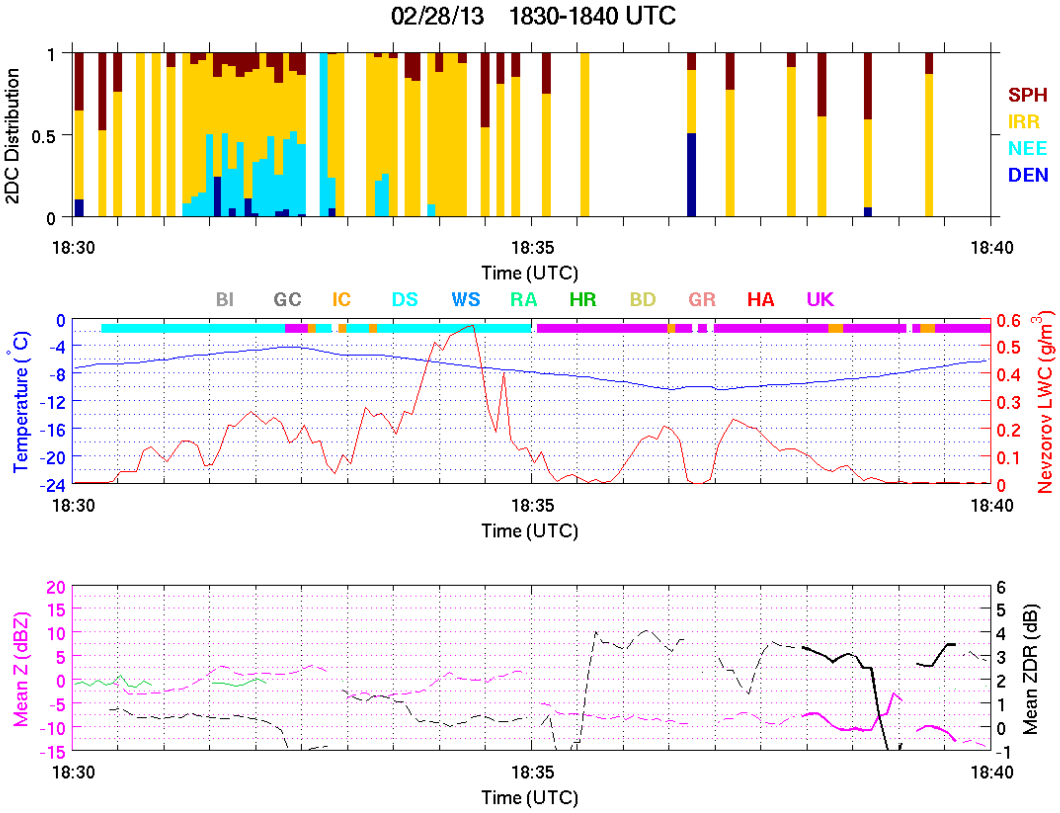

Figure 6-33. Ten-minute time series segment for the period 1830 to 1840 UT showing a period of maximum supercooled water content between a period of needle crystals (see SNDI algorithm, top) and a period of hexagonal flat plate crystals (with enhanced ZDR and HCA designation 'Unknown').

As an illustration of the abruptness of the transition from one crystal type to another during aircraft ascent and descent, we have found several examples of 2DC imagery, continuously recorded during such transitions. Figure 6-34, spanning the six-minute time interval from 18:47:12 to 18:53:23 UT, shows a good example of predominantly HFPs in the top portion and needles in the bottom portion, with a change in just 30–40 seconds. In this case, no maximum in SLW was noted during the transition.

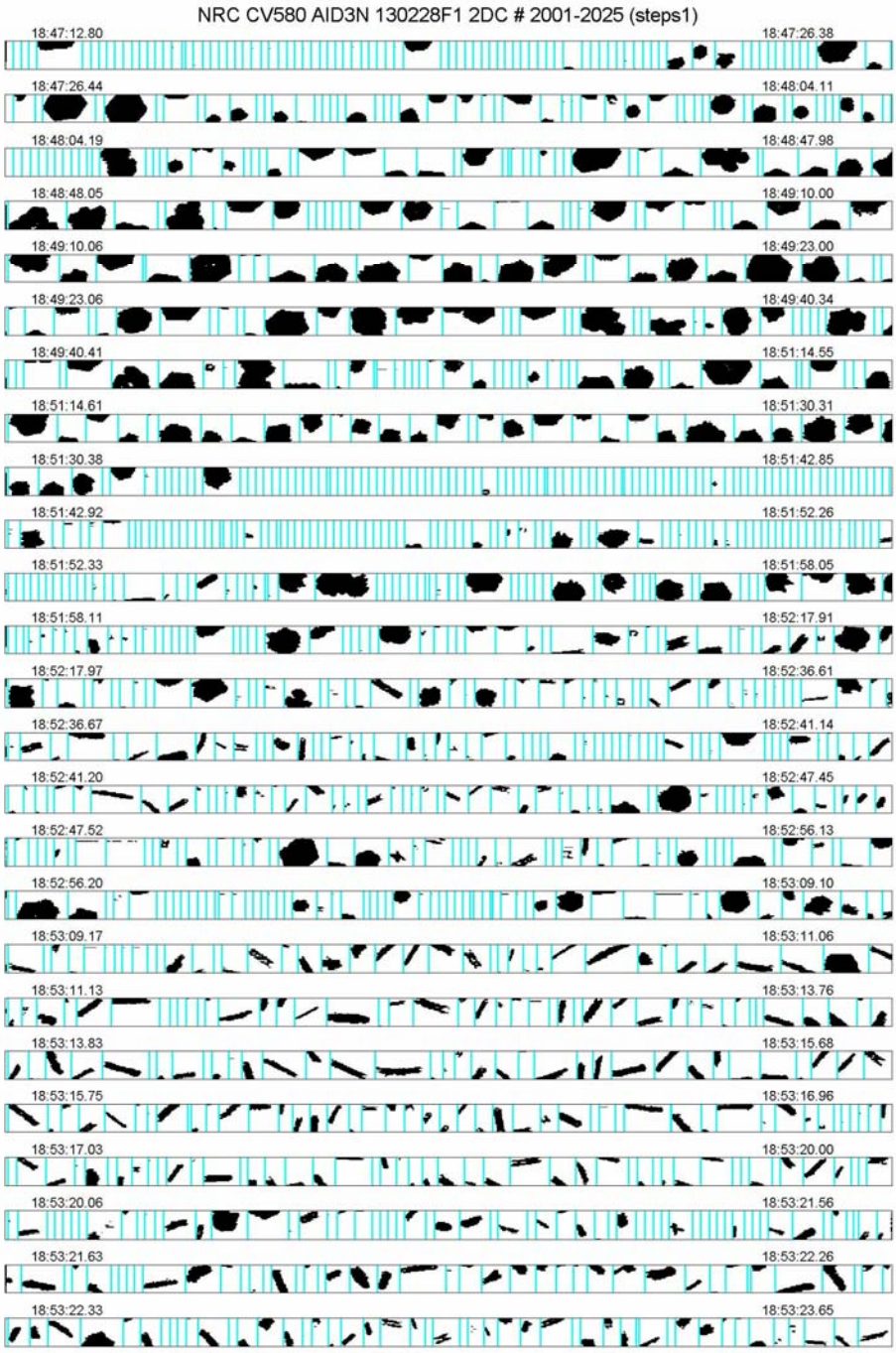

Figure 6-34. Continuous imagery from the PMS 2DC probe for the time period 18:47:12 to 18:53:23 UT showing an abrupt transition from hexagonal flat plate crystals to needles during the descent of the aircraft from T = –10° C to T = –4° C.

At 1944 UT, a conspicuous identification of ‘Big Drops’ by HCA at an in situ temperature of –10° C prompted a closer examination of the reasons for the apparent miss. Figure 6-35 shows the 10-minute time series segment that includes this misidentification, in the midst of longer segments with correct identification of ‘Dry Snow’ in the presence of rich concentrations of ‘Dendrites’ in the SNDI algorithm. Examination of the 2DC imagery confirms the presence of large dendritic crystals at the time in question. Figure 6-35 shows that ZDR is also maximizing at this time to +1.3 dB. That signature together with a >15 dBZ reflectivity may be admitting the ‘Big Drops’ classification, despite the rather low in situ temperature. Incidents such as this are deserving of further examination.

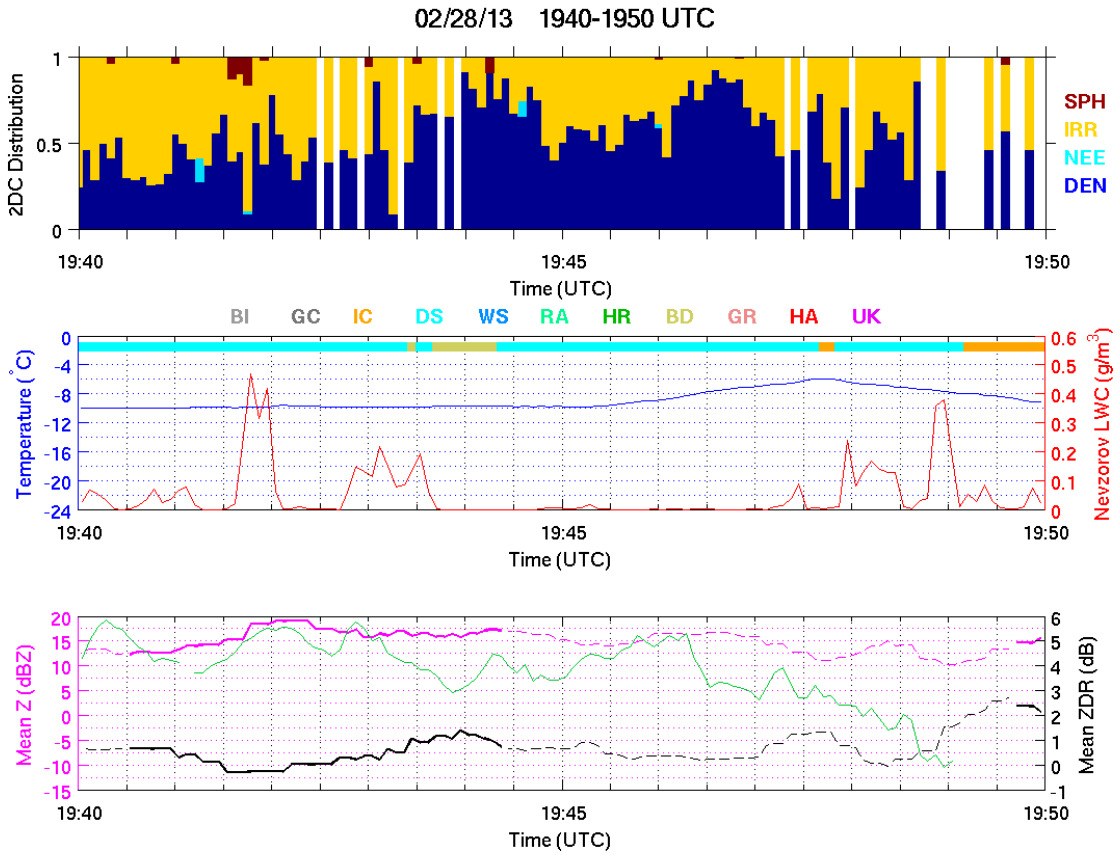

Figure 6-35. Ten-minute time series segment for the interval 1940–1950 UT when the Hydrometeor Classification Algorithm is identifying ‘Big Drops’ at 1944 UT. Supercooled liquid water is also identified by the Nevzorov probe in the beginning of this misidentification period.

As further documentation of the KBUF dual pol response to the quasi-uniform ice crystal regimes during this flight, a Z-ZDR scatter diagram shows specific space-intervals when hexagonal flat plates, needles, and dendrites were the Convair-verified targets. That diagram is shown in Figure 6-36.

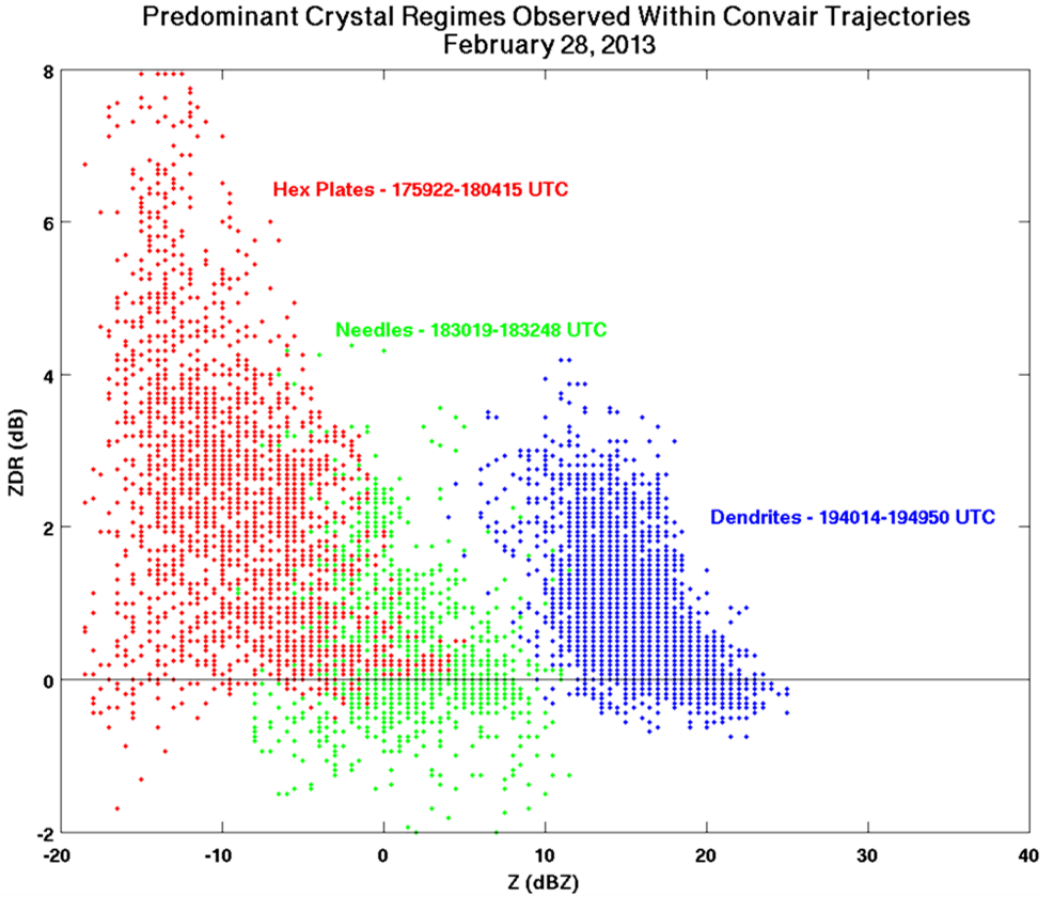

Figure 6-36. Summary scatter plot of reflectivity (dBZ) and differential reflectivity (dB) for the periods of quasi-uniform ice crystals observed during the flight on February 28, 2013. The ordering of ZDR values is broadly consistent with the theoretical calculations discussed in Section 2.

Crystals with the most anisotropic response, and hence the largest +ZDR values, are the hexagonal flat plates. Some of these pulse-resolution-volume-integrated values are as large as +8 dB and, so, close to the theoretical limit for oblate plates. In contrast, the reflectivity for the plates in Figure 6-36 tends to be least, perhaps because their lateral growth at any value of ice supersaturation is less than that for needles and dendrites, and because in conditions of intermittent LWC, they are not always growing at water saturation. The dendrites show the largest reflectivity values of all crystal types because they are the fastest growing shapes and require water saturation for their presence. Though these quasi-uniform crystal

regimes may serve as fingerprints for the presence of SLW, the quantity of SLW (needed for water saturation) may not always be hazardous to aviation.

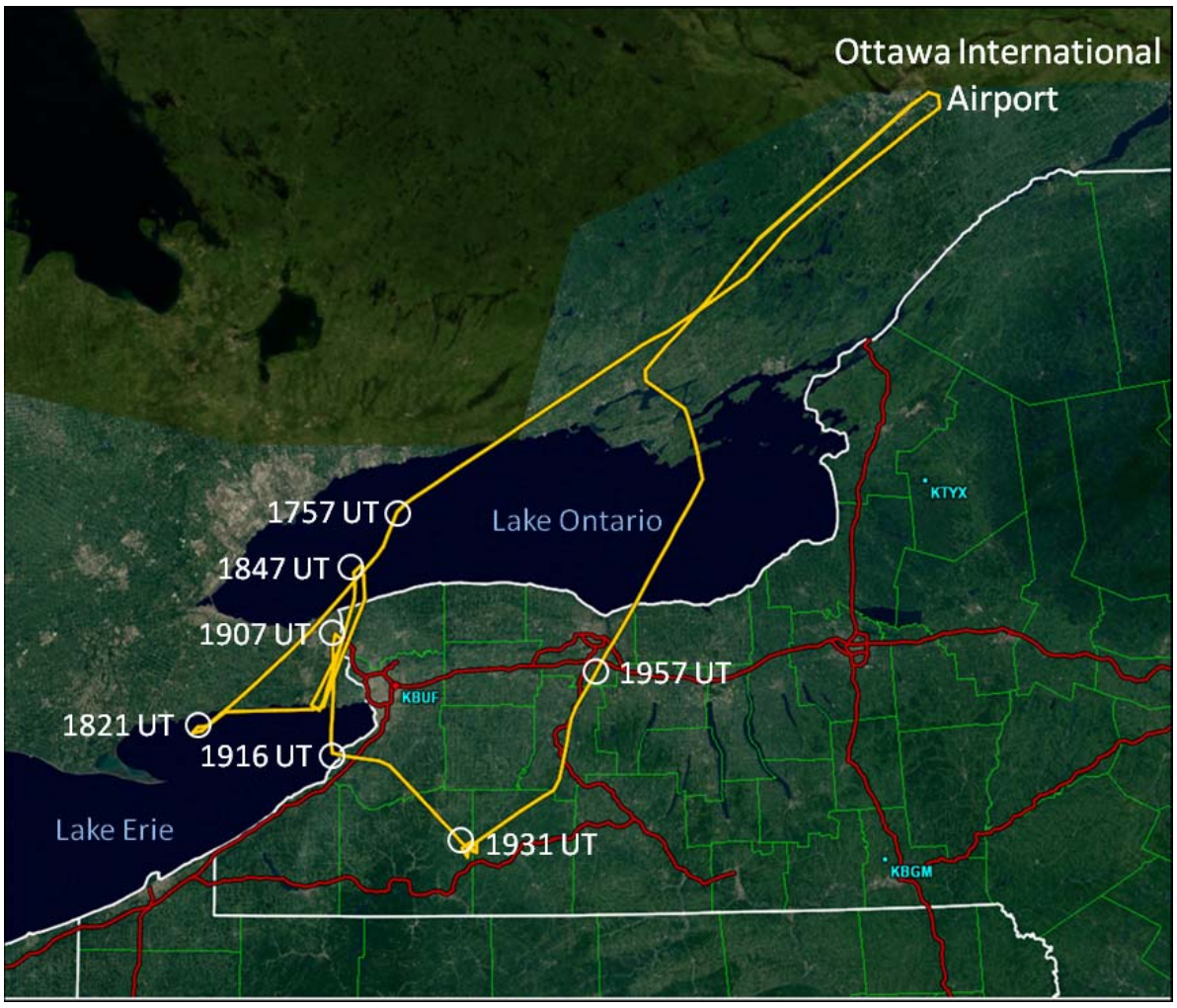

Figure 6-37. Plan view of the Convair flight from Ottawa to areas both northwest and south of the KBUF NEXRAD radar on February 28, 2013.

This page intentionally left blank.

7. DISCUSSION ITEMS

7.1 VERIFICATION OF HCA WITH CONVAIR SNDI

The current HCA precipitation classification categories and interpretation were presented in Section 2.3. The NRC aircraft particle identifier is able to classify the shapes of the particles/drops intercepted by the aircraft. The particle classification provides an opportunity to verify whether the current HCA is correctly categorizing the type of precipitation. There are challenges when relating derived onboard particle image classifications to NEXRAD HCA classifications due to the nature of the data (particularly in terms of image resolution for resolving crystal sub-structures). In addition, the onboard data are virtually a point source of information compared to NEXRAD pulse resolution volume HCA sampling – orders of magnitude difference of sampling volumes. The onboard particle image data are from hydrometeors explicitly intercepting the sensor. The NEXRAD classifications are based on a complex interpretation of remotely sensed returns from a bulk collection of hydrometeors.

Three particle imagers were available on the NRC aircraft, 2DC (for smaller sizes) and 2DP and 2DG (for larger sizes). NRC uses a post-processing image detection algorithm to determine the percentage of each particle type at each time step (Korolev & Sussman, 2000). After careful examination of the output from the two sensors, the 2DC data were chosen because that output was more stable over time. The onboard particle images are broken into four categories: 'Spheres' (S), 'Needles' (N), 'Dendrites' (D), and 'Irregulars' (I). They are collectively referred to as SNDI data with examples of such shown in Section 6, and a brief explanation of the algorithm in Section 3.1.5. The particle designations were not designed to provide classifications of the kind in the NEXRAD HCA. Therefore, to use SNDI data as a NEXRAD-esque classifier for comparison against actual HCA results, LL needed to develop a reasonable set of classification rules.

The SNDI data are only useful for classifying the precipitation categories. So for this hydrometeor verification analysis, 'Biological' and 'Ground Clutter' were not considered. In addition, the 'Unknown' category, by its very nature, cannot be verified because we do not know what the category represents (Section 7.4 discusses the 'Unknown' category further). Table 7-1 shows the threshold limits that were utilized in creating the scoring rubric to compare the HCA particle type to that of the SNDI sensor. Note that the verification of HCA with SNDI data is not an absolute test; the classification rules are designed to illustrate whether the particle types sampled are consistent with the identified HCA category. Overlaps are evident in the context of the SNDI thresholds and cannot be resolved further due to the limitations of the SNDI data both in resolution and categorization. For example, the rain categories in HCA should predominantly contain drops of water that would appear as spheres in the SNDI data. Therefore, the 'Big Drops,' 'Rain,' and 'Heavy Rain' categories are all verified when the 'Spheres' category percentage exceeds 50%.

TABLE 7-1

SNDI Categorization Thresholds

Description of Presence	Test Utilized	Explanation
Not present	"<10 %"	Threshold accounts for incorrect classifications with SNDI.
Mixed	">25 %"	When no one category is expected to dominate, but a category is expected to be present.
Primary category	">50 %"	When a category of particles is expected to be the primary type of particle found, but allowing for a mix of other particles.
Dominant	">75 %"	When a category of particles is expected to represent the vast majority of the particles.

The following set of classification rules were used to verify HCA with SNDI data:

Big Drops, Rain, Heavy Rain:

In periods of any form of rain, the particle detector analysis should be dominated by spheres from the water drops. In addition, the straight edges from needles or the branches from dendrites would indicate that some form of freezing is occurring. That mix would be more indicative of wet snow than rain, so needles and dendrites should be very small. Finally, the 'Irregular' category might be expected to be present as deformed drops may present themselves as irregularly shaped (this is also the default category in SNDI if it cannot classify the particle). Therefore, when SNDI indicates that the 'Spheres' category exceeds 50% of the samples, each of these HCA categories is considered verified by the SNDI analysis.

Hail:

Hail could appear as 'Spheres' (particularly for small hail) and/or 'Irregulars' (where the hail has developed nodules of ice). But 'Needles' and 'Dendrites' should be at very low levels due to the melt/freeze cycles implied by hail. Therefore, the threshold test for 'Hail' is verified when SNDI data show more than 50% 'Spheres' or 'Irregulars.'

Wet Snow:

Wet snow should be very dense with water and would appear as predominantly 'Spheres' or 'Irregulars' (where the sticky wet snow clumps together into odd shapes). Given the very wet nature of this category, 'Needles' and 'Dendrites' should be rare. Therefore, the threshold test for 'Wet Snow' is verified when SNDI data show more than 50% 'Spheres' or 'Irregulars.'

Ice Crystals:

Ice crystals grow as crystalline structures with branches, creating particles that when viewed by the sensor should have sharp edges and straight lines. Therefore, the 'Needle' and 'Dendrite' categories should be present. But, their relative presence to one another will vary based on temperature, updraft speed, and polarization. 'Spheres' should not be present in ice crystal regions, and 'Irregulars' should be at low levels as well. Therefore, 'Ice Crystals' are verified by SNDI when 'Needles' or 'Dendrites' are greater than 25%.

Dry Snow:

The reflectivity parameters for 'Dry Snow' are very broad, with a low value near the upper limit of 'Dry Snow' and the upper limit near 'Wet Snow.' As such, there are particles mixed in dry snow that range from needles and dendrites to irregulars. Therefore, it is easier to say that spheres should not be present, as their presence would tend to indicate rain or graupel and hail shapes. However, all other categories may occur in varying proportions to one another. Hence, 'Dry Snow' is verified by SNDI when 'Spheres' are less than 10%.

Graupel:

Finally, graupel is formed by SLW encrusting dry or wet snow particles. In cases where very little riming has occurred, the shapes will be similar to wet snow. But, in cases where more complete ice-over has occurred, the shapes would be more spherical. And, given the dynamic nature of graupel generation, it is likely that in any given time period there would be a mix of these two particle shapes. Therefore, 'Graupel' is verified by SNDI when either 'Irregulars' or 'Spheres' are greater than 25%.

There are many rationales possible when developing rules for converting SNDI edge categorizations to HCA categories. There could very well be other plausible combinations and nuances to explore in the future that are viable as well. Table 7-2 lists the HCA category and the corresponding SNDI verification thresholds that were identified for each precipitation type. Note that the rules do not invoke aircraft temperature. The NEXRAD HCA does not have the benefit of explicit temperature data to aid (or hinder) its performance. Further, quantities such as Nevzorov LWC were not used in this first attempt to declare NEXRAD-esque classifications from SNDI, as that adds layers of complexity and starts a path of developing a new, independent onboard-appropriate classifier. However, HCA comparisons to LWC are discussed in Section 7.4.

TABLE 7-2

SNDI Thresholds for Verifying HCA Categories

HCA Category	SNDI Thresholds
Graupel	I > 25% OR S > 25%
Dry Snow	S < 10%
Ice Crystals	N > 25% OR D > 25%
Wet Snow	S > 50% OR I > 50%
Hail	S > 50% OR I > 50%
Big Drops	S > 50%
Heavy Rain	S > 50%
Rain	S > 50%

Table 7-3 shows the verification statistics for all the aircraft encounters with a specific HCA category based on the SNDI verification tests in Table 7-2.

While every precipitation category was encountered over all the cases, three categories dominate: 'Dry Snow,' 'Ice Crystals,' and 'Graupel.' Figure 7-1 shows the breakdown of HCA categories for the three flights. As detailed in Section 6, each flight had different properties, and Figure 7-1 highlights that the February 28 flight is very different in terms of HCA encounters. In the other two flights, 'Dry Snow' dominates, but on February 28, 'Dry Snow' is present but less so than in the other flights. In addition, 'Graupel' is only encountered on February 26, and there is also a short but concentrated period of 'Heavy Rain.' The remaining four HCA categories have fewer than 40 observations each over all the cases. For these categories, the relevance of the scoring data is limited. But, the SNDI results for 'Heavy Rain' indicate that 'Spheres' is the predominate category, resulting in an 89% Probability of Detection (POD). ('Wet Snow' categories also score well). The sensed temperature of the aircraft in the cases where HCA declared 'Big Drops' is well below zero (–7° C to –9° C), which is far below the allowed temperature for HCA to declare this category. The temperature in the NEXRAD algorithm (from the NEXRAD Melting Layer Detection Algorithm (MLDA)) is incorrect in this case, and HCA would have yielded a frozen category if it had had the correct temperature. A similar error is likely occurring in the rain category where the aircraft is reporting just below 0° C. The 'Hail' category has the fewest aircraft encounters of all the precipitation categories. In addition, it is far easier to verify hail aloft with ground observations and during the development of HCA the 'Hail' class was verified through intensive observation programs.

In the higher incidence categories, the 'Dry Snow' and 'Graupel' categories have PODs of 76% and 94%, respectively. Therefore, these HCA categories appear to verify well with the SNDI data. However, as was stated earlier, the SNDI data only supports a very broad verification of the encountered HCA categories. The 'Ice Crystal' category, where 'Needles' and 'Dendrites' were expected to be the predominant categories, did not score well (POD 22%). Referring again to Figure 7-1, the scores for individual flights are listed above each category. Note that on February 28, where 'Ice Crystals' were relatively more prevalent, there is a much higher POD (64%). The SNDI data consistently indicated 'Irregulars' in the February 19 and February 26 flights and, given the widespread nature of the 'Dry Snow' on those days, it is likely that the low scores represent a failure of the HCA to properly categorize these regions.

TABLE 7-3

Verification of NEXRAD HCA Category with SNDI Thresholds (all flights)

NEXRAD HCA Category	Hits	Misses	Total Observed	POD (%)
Dry Snow	2600	804	3404	76%
Ice Crystals	115	403	518	22%
Graupel	250	17	267	94%
Heavy Rain	39	5	44	89%
Big Drops	7	9	16	44%
Rain	0	12	12	0%
Hail	4	4	8	50%
Wet Snow	7	0	7	100%
Overall	3022	1254	4276	71%

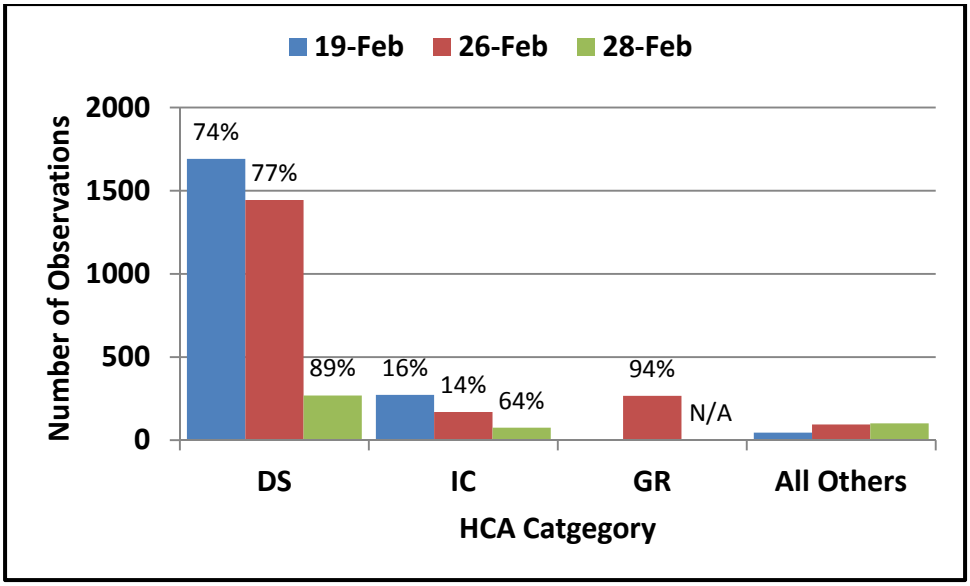

Figure 7-1. HCA category distribution (color bars) and PODs (% numbers over color bars) for the three flight days.

A perspective regarding judging the wellness of the NEXRAD HCA based on the three, 2013 icing missions is that only one HCA class – 'Dry Snow' – accounted for about 75% of total observations. General observation of the HCA performance during winter storms frequently shows that 'Dry Snow' is the predominant category above the freezing level. The question arises as to whether the predominance of 'Dry Snow' will validate. The icing missions confirmed that the 'Dry Snow' class is frequently masking the presence of SLW, and that other, secondary-type HCA classes were therefore under-sampled. An initial takeaway message for NEXRAD HCA should be that generally all the classifications, no matter their amount sampled, show positive performance. Further, this is the first ever attempt to have in situ measurements within NEXRAD radar volumes for the purpose of validating the fielded, operational NEXRAD HCA directly. Looking ahead, this data set (Convair and KBUF) has a potential to be exploited further regarding classifications. However, making a classifier from onboard SNDI, LWC, temperature, etc. would be challenging. A second approach could be to develop a better SNDI algorithm based on advanced image recognition concepts. In either case, there still will be no substitute for additional in situ icing missions in all seasons to fully vet the operational NEXRAD HCA.

Reliance on the SNDI algorithm (Korolev and Sussman, 2000) for 'calibration' of hydrometeor types should be interpreted cautiously. Some success has been achieved here, but two key limitations we have encountered are (1) the resolution of the PMS 2DC imagery that feeds the algorithm, and (2) the fact that SNDI was not designed with HCA verification as a goal.

As far as the first limitation is concerned, the SNDI developers summarized the situation by saying: "Nakaya (1954) used 41 categories for classification of ice particles … The low pixel resolution (25 μm), the small field of view, and the low grey-level resolution (black and white) makes the habit recognition of OAP-2DC imagery significantly limited, and it definitely cannot provide classification of 40–80 habit categories." Clearly for first-class verification of HCA, a hydrometeor category count greater than four is highly desirable. As indicated by dedicated observations of winter time precipitation with high resolution microscopes, the classification of the 'Irregular' particles in the SNDI algorithm can be greatly improved (Stoelinga et al., 2006). Despite the limitations of SNDI, we frequently visited the raw 2DC imagery for the three flights to gain improved physical insights about the microphysical scenario. But unfortunately one needs quantitative information to do HCA scoring.

As far as the second limitation is concerned, the problem is really twofold. HCA was developed (Park et al., 2009) without consideration of supercooled water as a primary objective. 'Dry Snow' can legitimately be accompanied by supercooled cloud droplets, but that condition is not explicitly recognized in the HCA. Furthermore, supercooled drizzle, despite being a radar target, is not a category in the HCA.

7.2 DISCUSSION OF MADISON, WISCONSIN, INCIDENT AS CASE STUDY

In addition to the dedicated mission with the Convair-580 to verify in situ icing conditions, other chance opportunities arise for documenting icing hazard when aircraft traverse regions with supercooled water that are also within range of a NEXRAD radar. One such event occurred on February 21, 2013 between Watertown and Madison, Wisconsin. MIT Lincoln Laboratory was notified about this event by Thomas Webster at the FAA shortly after the incident, and it was subsequently investigated as another case study.

The pilot of a Piper Archer aircraft ventured out of Watertown airport ~13 km northwest of Milwaukee in late afternoon to make some practice takeoffs and landings, with full expectation that the forecast ceiling height of 1800 ft would be suitable for his planned activity. Shortly after takeoff at 4:20 p.m. local time, the pilot encountered a substantially lower ceiling at 600 ft, at which point his windshield immediately 'fogged' with rime ice, largely blocking his view. Shortly thereafter, the pilot radioed air traffic control in nearby Madison to report his condition, and they recommended that he proceed to that airport to land.

The extending aircraft flight track, sampled at three times from the time of the radio call to the time of landing in Madison (at 4:57 p.m.), are shown in Figure 7-2, in which the red square to the east shows the location of the Watertown airport, and the red square to the west locates the Madison airport. The NEXRAD KMKX (Milwaukee, WI) dual pol radar was operating in clear air mode during much of the important time interval of this flight, thereby providing additional sensitivity to weak radar returns, as discussed in Section 7.3 of this report. Figure 7-2 shows the measured reflectivity in the top row, the differential reflectivity in the middle row, and the hydrometeor classification results from the radar analysis in the bottom row, all taken from the 0.5° elevation angle lowest level PPI scan for KMKX. The great majority of the radar returns lies in the 'grey' portion of the reflectivity color scale, with values in

the range –5 to 5 dBZ. In the clear air scan, all of these values are well above the noise level of the radar. The ZDR values are distributed tightly around 0 dB, though some very localized values (off the flight track) reach the red region of the color scale at +3 to +4 dB. The HCA plots show a dominance of lavender color indicating 'Unknown,' but also prevalent 'Dry Snow' conditions (in turquoise color).

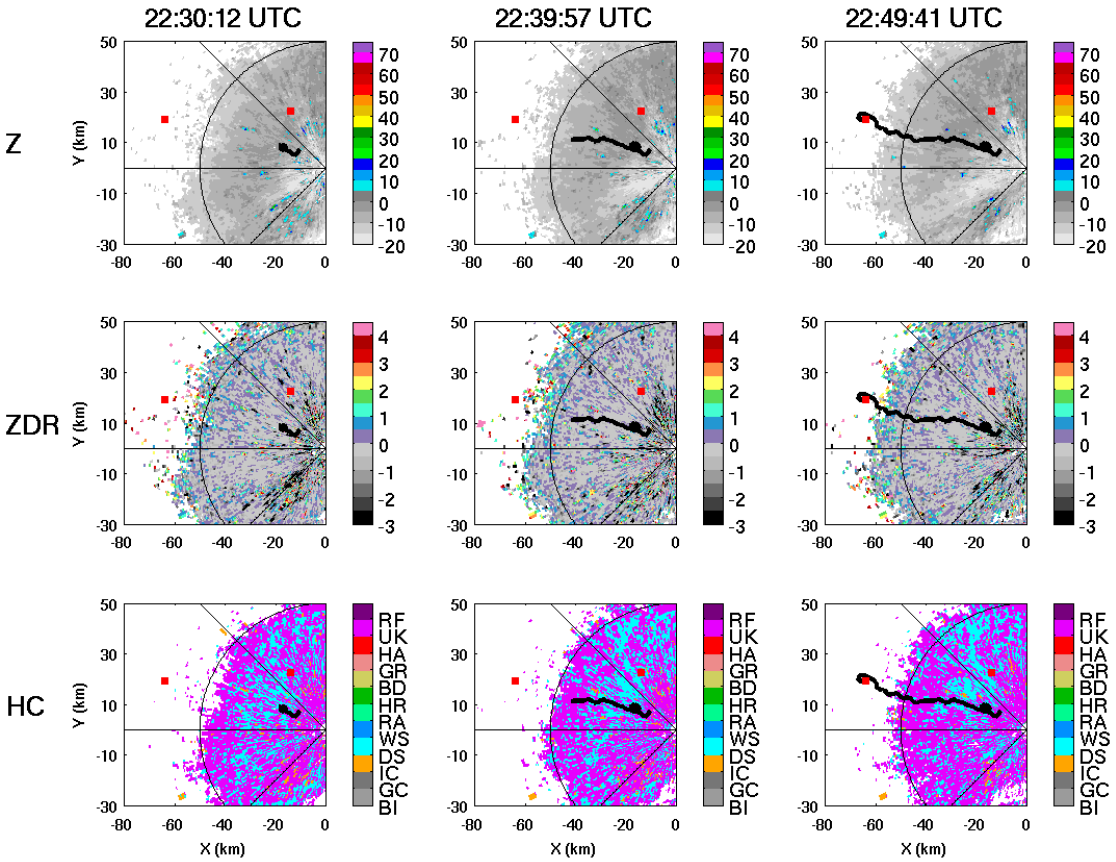

Figure 7-2. KMKX NEXRAD radar observations (north up the page) at three times during the flight of the Piper Archer aircraft from Watertown (red square to east) to Madison (red square to west), and showing smoothed reflectivity SMZ (dBZ) (top row), differential reflectivity ZDR (dB) (middle row), and the results of the Hydrometeor Classification Algorithm (bottom row).

The pilot relayed afterward that he was in icing conditions for essentially the entire flight. The total path length from the takeoff in Watertown to the landing in Madison has been estimated at 108 km. The report that the pilot could see out of one small clear space in the windshield was attributed to the effect of the aircraft defroster, finally beginning to work near the time of landing. Substantial rime ice had accumulated on many portions of the aircraft and had a major impact on the aircraft performance,

particularly on the approach to Madison. For negotiating the turns evident in the flight track in Figure 7-2, the pilot made use of rudder rather than the ailerons out of concern that the plane might stall with the extra wing loading.

The rime ice accumulation on the aircraft was documented in photographs taken only 2–3 minutes after the landing in Madison. Sample photographs are shown in Figure 7-3 for the nose of the plane, the gas cap on the wing, and on the slanting antenna. The air temperature on the ground at the time of landing was –6° C, enabling good preservation of the rime deposits. The maximum rime thicknesses were measured from the photographs, using specific known aircraft dimensions for 'scale,' and ranged from 50–60 mm. Given the total flight length and the mean speed of the aircraft (100–115 knots), one can estimate a mean rime accretion rate of 2.5 mm/100 seconds (±15%). This estimate can be compared with the simple calculation for rime accretion rate discussed previously in Section 2.6 to infer a mean supercooled LWC intercepted by the Piper Archer aircraft, as shown in Figure 7-4. The inferred values are in the range of 0.3 to 0.5 g/m^3 and so well within the range of values measured by the Convair-580, as documented in the probability distributions for the three flights in Figure 5.1. The estimated accretion rate is less than the threshold identified as 'severe' by Newton (1978) and discussed again by Cober et al. (2009), and also included in Figure 7-4 for comparison. An important lesson from this analysis is that even with modest SLW values in situ, extending horizontally in layers as we expect is the case for this incident, if any aircraft remains in such a layer for a sufficiently long time (in this case 30 minutes or more), serious problems may result.

Figure 7-3. Photographs of rime accretion on the Piper Archer aircraft on (a) nose of aircraft, on (b) the gas cap on the wing, and (c) on the slanted antenna. These photographs were taken a few minutes after the plane landed.

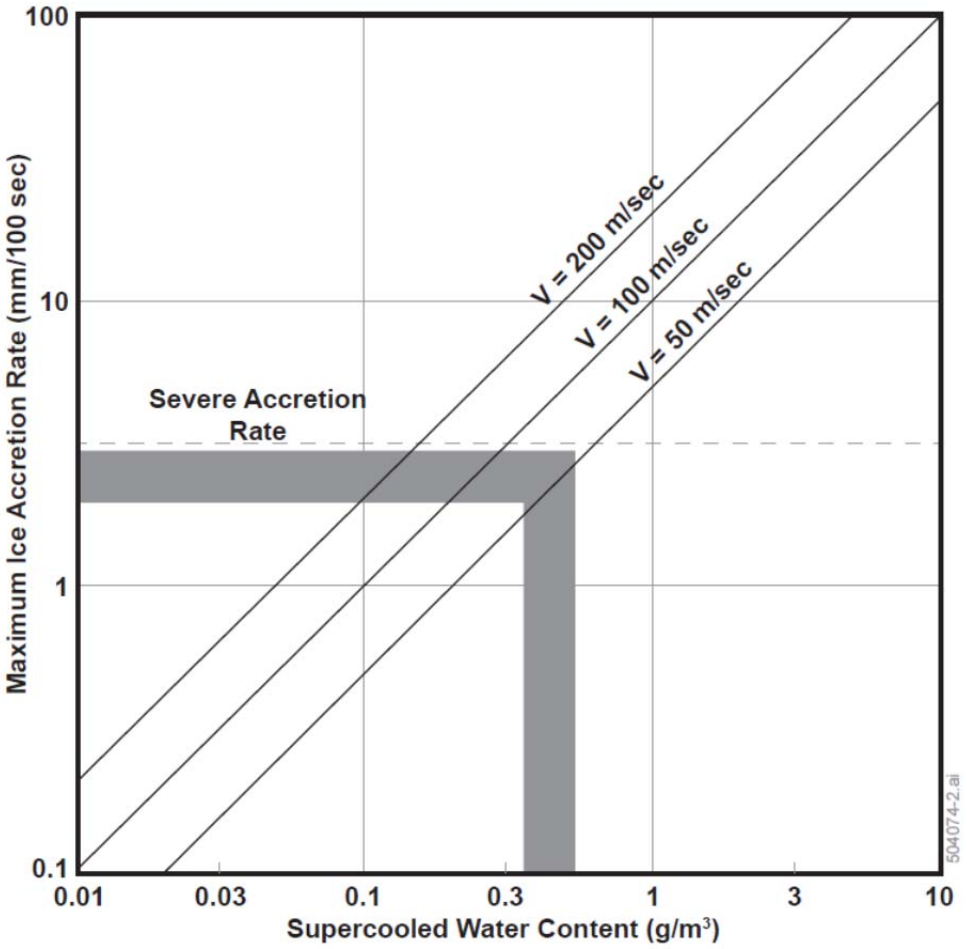

Figure 7-4. Comparison of estimated rime accretion rate with the theoretical predictions shown earlier in Figure 2-7 in Section 2 of this report. The gray region provides best estimates (and attendant uncertainty) for the icing situation with the Piper Archer aircraft on Feb. 21, 2013.

7.3 OPERATIONAL VALUE OF CLEAR AIR MODE RADAR SCAN FOR WINTER STORM DIAGNOSIS

Winter weather often differs by orders of magnitude from summer, convective weather in terms of lift (upward vertical motion), available moisture, time duration of event, and area extent of features. Thunderstorms have much larger updrafts (10+ m/s) focused in small zones (10–20 km) as compared to the long, gentle lift (1 m/s) of overrunning "warm" air in winter synoptic-scale systems (100–500 km). The life cycle of the most intense thunderstorms that evolve into mesoscale convective systems is on the order of one day, while synoptic winter systems last for perhaps five days. From a weather radar

perspective, this reality of weather manifests itself in the type of radar echoes forecasters and NEXRAD algorithms have available to them.

The key radar features in convective weather are relatively short-lived, fast-moving, and intense. The NEXRAD program designed volume coverage pattern 12 (or VCP12) as a select sequence of elevation angle scans specifically to maximize monitoring such weather. The trade-off made to perform full volume, VCP12 scans in 4.1 minutes is to reduce the sensitivity to weaker weather. This is because the radar must scan through a large swath of azimuth in a short time resulting in fewer individual pulses per resolution volume. Table 7-4 below for VCP12 shows the azimuthal scan rate (AZ Rate) and the associated pulses available for each scan angle. The tan rows indicate angles with a surveillance scan followed by a Doppler scan (more pulses, but less range). The Doppler scan is the scan used to collect dual pol parameters. The blue rows indicate "batch" processing with an interleaving of surveillance and Doppler pulsing. The purple rows for the upper scan angles show the pulses for Doppler scanning.

In non-winter weather, the FAA prefers VCP12 for its rapid updating while monitoring the convective weather as such weather is a major variable in disrupting National Air Space capacity. The forecasters at the National Weather Service (NWS) offices likewise prefer VCP12 in order to best serve the public with issued warnings and alerts relating to wind and water in convective weather. For the first two in situ icing missions, LL requested the KBUF and KCLE weather forecast offices to operate their NEXRADs in VCP12 so as to have the most rapid updating of radar volumes and minimize time separation between radar-collected and Convair-collected data. Strong weather likely permeates the collective psyche of the NEXRAD operators (NWS), and even in winter weather it is usual to observe the radars in operation with precipitation mode VCPs (including 12).

The NEXRAD program does not have a specific VCP designed for weaker winter weather. There are, though, two clear air scan strategies available ostensibly to operate the radars when little to no weather radar returns are present. In fact, automatic algorithms in the NEXRAD system are designed to relieve a radar of a precipitation mode VCP when area coverage and intensity thresholds indicate lack of weather. In some regions such as the Great Lakes and Northeast U.S., radar operators select the clear air VCP 31 to monitor winter weather. This VCP completes a reduced set of elevation scan angles in 10 minutes. The trade-off to get improved sensitivity to the (usually) weaker winter weather is a noticeably slower update of the weather from volume to volume. The VCP31 table in Table 7-4 below shows the much slower AZ Rate and subsequent much improved number of pulses per resolution volume that provide for a sensitivity gain estimated to be about 4.8 dB (source: Warning Decision Training Branch). Color coding is the same as with the VCP12 table.

TABLE 7-4

VCP12 and VCP31 Scanning Strategies

VCP 12		
Angle (°)	AZRate (°/sec)	# Pulses
0.5	21.15	15
0.5	24.99	40
0.9	21.15	15
0.9	24.99	40
1.3	21.15	15
1.3	24.99	40
1.8	26.64	3, 29
2.4	26.40	3, 30
3.1	26.40	3, 30
4.0	26.40	3, 30
5.1	28.00	3, 30
6.4	28.00	3, 30
8.0	28.40	38
10.0	28.88	40
12.5	28.74	44
15.6	28.74	44
19.5	28.74	44

VCP 31		
Angle (°)	AZRate (°/sec)	# Pulses
0.5	5.04	63
0.5	5.07	87
1.50	5.04	63
1.50	5.07	87
2.50	5.04	63
2.50	5.07	87
3.50	5.07	87
4.50	5.07	87

For the last in situ icing mission on February 28, LL requested VCP31 be operated, as this is more in line with the procedures at KBUF. The longer time between updates in radar products, though, generally increased the separation time between the NEXRAD KBUF and Convair data. During this mission, KBUF did not switch to a precipitation mode. However, for the Wisconsin icing incident discussed in Section 7.2, the NEXRAD at Milwaukee (KMKX) did for a single volume switch between VCP31 and precipitation mode VCP21. We do not know why the switch was made, and after one volume, the radar was switched back to VCP31. The images below in Figure 7-5 show the sequence in the radar reflectivity data from VCP31 to VCP21. The panel shows base reflectivity from KMKX on February 21, 2013. The left is for VCP31 at 2340 UT, and the right is for VCP21 at 2350 UT. The reduced coverage is

apparent with VCP21 in this weak weather event. Very strong areas of return in both are suspected to be wind farms. Further, in VCP31, subtle fine structure to the weak weather returns is evident, and that is lost in VCP21. The ability of the NEXRAD to discern structure in such weak returns is currently not generally recognized by typical users of NEXRAD nor the NEXRAD algorithms such as the Hydrometeor Classification Algorithm that struggles with weak returns. As noted, the NWS not the FAA is responsible for the day-to-day operation and selection of VCPs in the NEXRAD network. LL recommends further study to explore parameters that would indicate when the improved sensitivity of VCP31 should be the default for winter weather monitoring at the expense of updating rate.

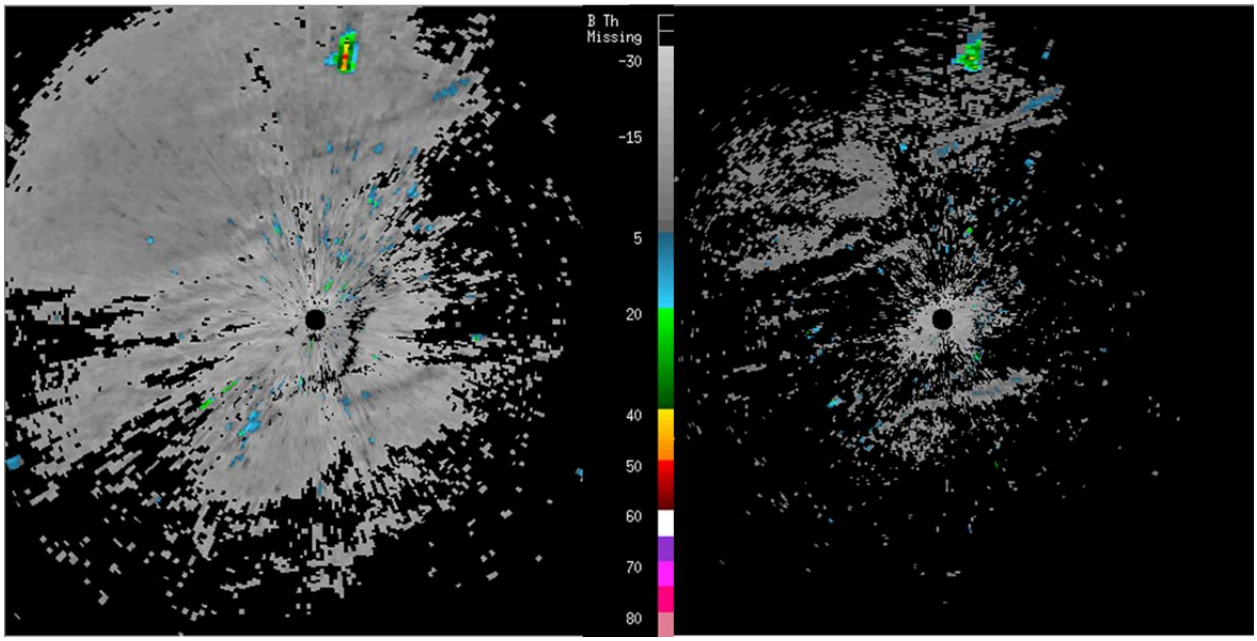

Figure 7-5. Radar reflectivity panels for the 0.5° elevation scan angle from the KMKX Milwaukee, WI, NEXRAD on February 21, 2013 are shown. The left panel is for 2340 UT, while the radar was in VCP31 clear air mode. The right panel is for 2350 UT, while the radar was switched for one volume into VCP21 precipitation mode. The considerable loss of sensitivity in this weak winter weather with the precipitation mode is evident.

7.4 CHARACTERIZATION OF SLW BY HCA CATEGORIES

The initial applications of HCA within NEXRAD were to provide (a) the ability to classify hail in hazardous thunderstorms, (b) a distinction between frozen and liquid precipitation for more accurate calculations of quantitative precipitation estimation (QPE), and (c) detection of clutter and biological contamination. As such, the HCA classifier does not have a SLW category because SLW is often in cloud

droplet form and is generally mixed with particles of larger size that mask the radar's ability to detect the SLW component. Instead, HCA attempts to classify the types of precipitation and non-precipitation categories by radar detectable parameters. Therefore, understanding the frequency with which a particular HCA class will include SLW and therefore have the potential for in-flight icing is important for the NEXRAD Icing Hazard Levels (IHL) algorithm.

Opportunities to verify active icing regions relative to the HCA categorization are limited. The most common methods, namely PIREPs, ground observations, and verified accidents, are discussed in the alternative icing verification section (Appendix A). These alternative methods offer assistance in verifying icing regions, but they don't shed light on differences in radar characteristics that would indicate how to modify the HCA to detect active SLW regions. In contrast, in situ aircraft measurements by NRC provide not only direct evidence of the presence of SLW, but also the opportunity to examine radar and thermal characteristics for subdividing key HCA categories into icing and non-icing categories.

One of the key tenets of the IHL algorithm is to leverage existing NEXRAD products in the development of the algorithm. Therefore, defining categories within HCA that are more or less likely to have areas of SLW is an important detail that can be extracted from the NRC flights. Four categories of HCA were broadly sampled during the NRC flights: 'Ice Crystals,' 'Dry Snow,' 'Graupel,' and 'Unknown.' Figures 7-6 through 7-9 show the relative distribution of SLW as sampled in these categories. The SLW distribution in (g/m^3) is broken down by None ($\leq$0.005 – based on the sensor sensitivity), Very Weak (0.005 to 0.05), Weak (0.05 to 0.1), and Significant ($\geq$0.1).

'Graupel' forms the basis of the IHL algorithm because the definition of graupel is that it is heavily rimed snow. Therefore, SLW is present in the creation of graupel and should be co-located with regions of 'Graupel' found by HCA. Figure 7-6 shows that the vast majority (93%) of graupel encounters had measurable SLW (above 0.005 g/m^3), confirming the use of 'Graupel' in the IHL algorithm.

Conversely, Figure 7-7 shows that a majority (62%) of the 'Ice Crystal' observations show no SLW present. While 18% of these observations do show significant SLW, of the four most frequent categories examined, 'Ice Crystals' were the least likely to be co-located with weak or significant SLW.

'Dry Snow' is observed to be the dominant category at altitudes above the freezing level (similarly the 'Rain' category dominates below freezing). As such, 'Dry Snow' has been a focus of LL efforts to understand if the category represents a uniform particle category or also contains regions of potentially significant icing. While 44% of the dry snow encounters had no SLW associated with them, a majority did have some level of SLW (see Figure 7-8). Given the widespread nature of the 'Dry Snow' category, there is a need to subdivide this category further in order to isolate the conditions where significant icing might occur.

Finally, the 'Unknown' category is produced by HCA when the coverage of reflectivity is significant but not enough interest weight generated from the other precipitation categories. LL has seen evidence that the 'Unknown' category can be associated with icing PIREPs. Figure 7-9 confirms that a

considerable portion (almost 30%) of the aircraft encounters with the unknown HCA category occur in regions that have significant levels of icing (0.1+ g/m^3). Based on the PIREP and in situ measurements, it is clear that the 'Unknown' category contains very disparate types of hydrometeors. A prototype HCA detector for 'Hex Plates' has been developed that is only triggered by the initial selection of 'Unknown' in HCA. Other subdivisions of the 'Unknown' category may also be possible.

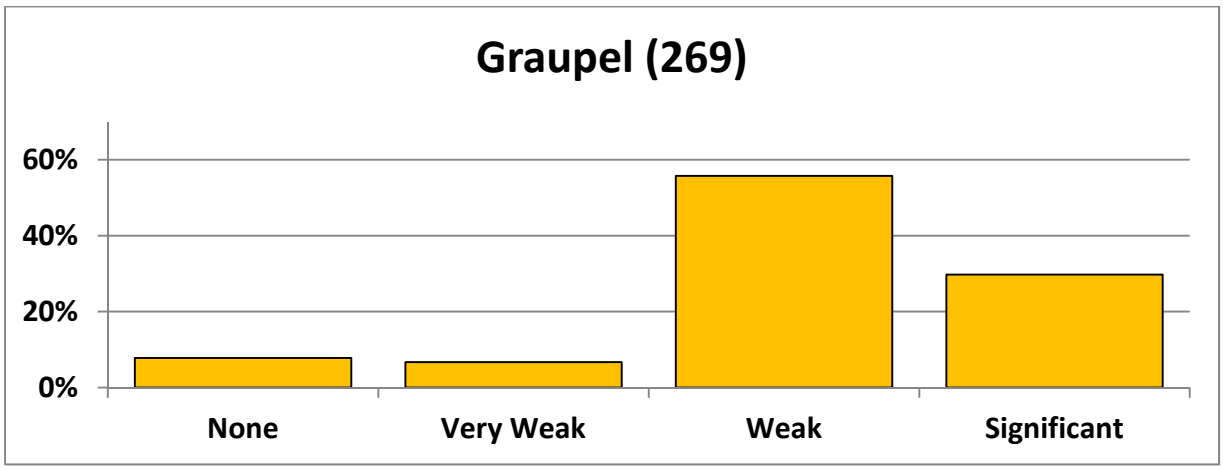

Figure 7-6. Distribution of SLW during aircraft encounters with HCA 'Graupel.'

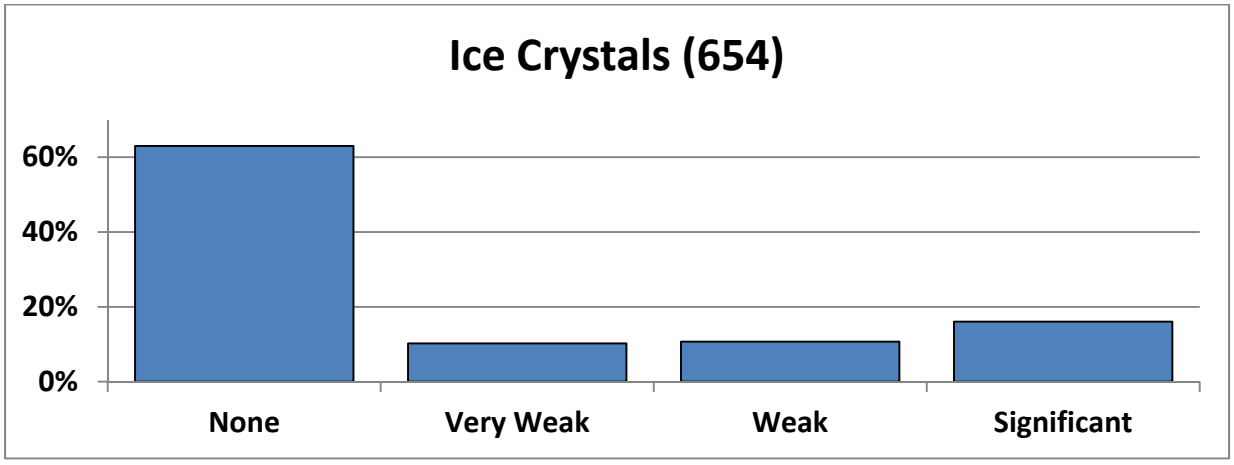

Figure 7-7. Distribution of SLW during aircraft encounters with HCA 'Ice Crystals.'

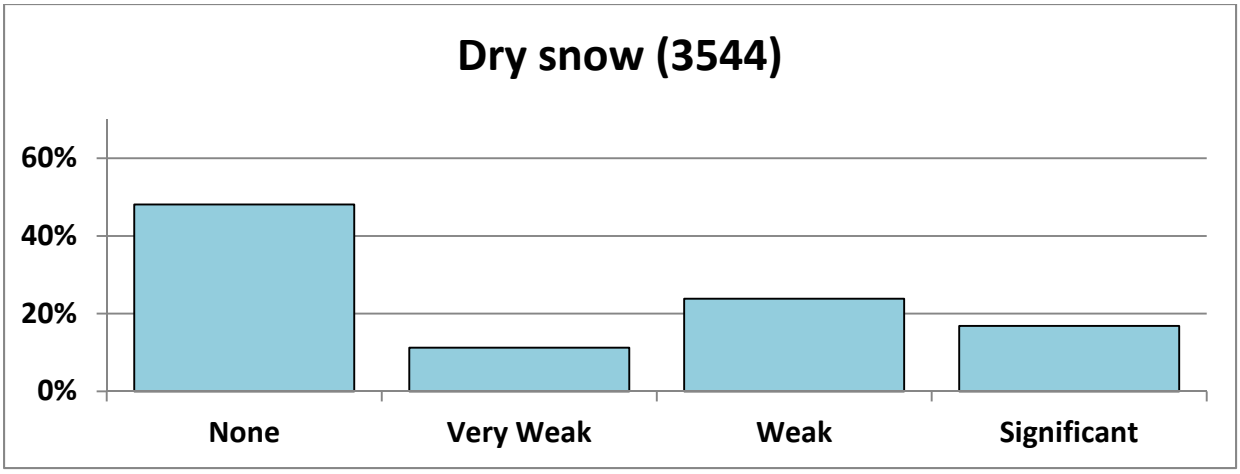

Figure 7-8. Distribution of SLW during aircraft encounters with HCA 'Dry Snow.'

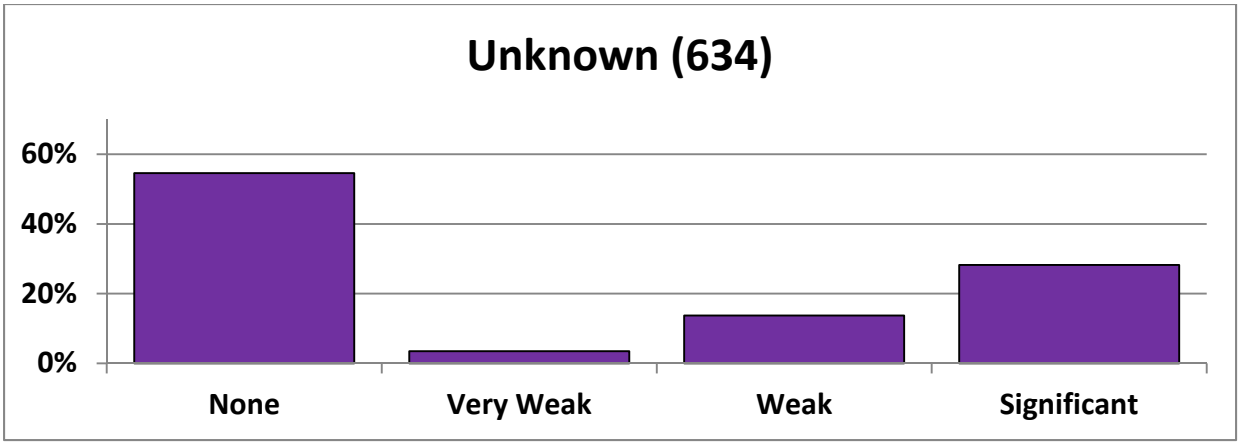

Figure 7-9. Distribution of SLW during aircraft encounters with HCA 'Unknown.'

7.5 RADAR DETECTION OF REGIONS WITH SUPERCOOLED WATER

Contrary to the expectation that SLW in cloud droplet form will not be detected by NEXRAD S-band radars, the present findings show that in the majority of cases in which in situ SLW is found, a radar return with a significant signal-to-noise ratio (SNR) is present. The Madison, Wisconsin, aircraft icing incident discussed in Section 7.2 is a graphic illustration of this claim, though in the absence of the "clear-air" NEXRAD scanning mode, many of these radar returns would have fallen below the radar sensitivity.

This is consistent with findings from the flights when comparing S-band reflectivity (SMZ) in the presence of SLW for all aircraft (five-second samples) and KBUF radar comparisons within ±120 seconds matched in time. For February 19, S-band data were coincident for 83% (762/913) of the total available comparisons in which LWC was >0.005 g/m^3. Similarly, 99% (1197/1207) and 79% (257/322) were coincident with significant LWC for the February 26–27 and February 28 flights, respectively. To contrast this with the onboard X-band radar, refer to Appendix D.

At least two cloud microphysical scenarios are possible for the existence of detectable radar returns from zones with SLW. The first scenario is based on a collision/coalescence process that enhances drop diameter D, greatly increases the D^6 contribution to radar reflectivity, and is favored by ultra clean aerosol conditions. The ultraclean condition guarantees that the available liquid condensate is shared amongst a smaller number of cloud droplets. Another example of this process occurring in a winter storm is found in Cober et al. (2001). The second possible scenario is based on the well-known Bergeron process, requiring only that the SLW zone contains some source of ice particles (ice nuclei, or the mixing of ice embryos from elsewhere in the storm) that can enlarge the ice crystal by vapor deposition in supersaturated conditions to radar detectable size. In the latter context, the small zones in the NEXRAD differential reflectivity with large ZDR values may be manifestations of the more localized growth of anisotropic crystals.

When the supercooled water is in drizzle drop form as on February 26–27, it is often radar-detectable, but drizzle drops are isotropic targets, much like the 'Dry Snow' targets in the cold part of the storm, and so the misidentification of the supercooled drizzle for 'Dry Snow' in the HCA is understandable. This is a challenging problem for dual pol observations in winter storms, but clearly of considerable importance in the context of aircraft icing hazard.

When the supercooled water is in raindrop form as it was for the February 26–27 case, then the oblate nature of these drops can serve as a signature for dual pol radar detection, but one must have reliable independent information on the temperature structure of the atmosphere to make the appropriate identification of "clear icing" zones. For this day, the model results had mixed success in matching the signatures derived from the NEXRAD dual pol radar alone. Nevertheless, the availability of dual pol observations in this situation brought considerably more definition to the situation than would ever have been possible with conventional single polarization radar.

As further confirmation, a comparison between PIREP icing observations and NEXRAD radar reflectivity was performed independent of the BAIRS in situ measurements. The analysis indicates that, within radar coverage of 125 km, the reflectivity is above threshold in 80–90% of the cases with active icing PIREPs. The study is summarized in Appendix B.

7.6 DUAL POL VARIABLES WITH AND WITHOUT SLW IN CLOUD DROPLET FORM

Preliminary efforts to identify distinguishing features in dual pol variables in regions with and without SLW in cloud droplet form (verified by aircraft FSSP measurements), in two periods classified as

‘Dry Snow’ in the February 19 flight by the NEXRAD radar-based HCA, met with limited success. The SLW in cloud droplet form is not in itself a radar target, so one must rely on some modifications of the radar detectable ice particle constituents of the ‘Dry Snow’ (amidst the supercooled droplets) to modify the dual pol variables. Riming is of course one possible modification, but that process is expected to dilute the anisotropy when ‘Dry Snow’ is already documented to exhibit a near-zero value of differential reflectivity. More work on this challenging aspect is needed.

8. MAIN CONCLUSIONS

The collaborative effort between LL and NRC has provided a wealth of information relative to the ability of the NEXRAD to detect icing hazards to aviation. These flights represent the first time that in situ verifications of NEXRAD dual polarization algorithms have been performed. In addition to verifying current HCA classifications, it has helped focus future algorithm development for IHL. Unequivocally, LL is further along in strategizing concept development for HCA and IHL based on the findings of the in situ missions than would have been possible otherwise.

During the course of three flights into three different storm environments, the sensor data have shown a rich diversity of conditions relevant to the icing hazard presented by supercooled water. The February 19 flight showed SLW in small droplet form and prevalent 'Dry Snow.' The February 26-27 flight showed SLW in large drop form and freezing rain with the potential for "clear icing" hazards without a current HCA category for such. The February 28 flight showed SLW in small droplet form and pristine crystals organized in layers, confirming predictions drawn from laboratory diffusion chamber measurements and revealing the 'Unknown' class to be associated at times with these conditions. The wealth of knowledge derived from these missions motivates LL to recommend further additional in situ aircraft observations.

Some success has been achieved with HCA verification of 'Dry Snow,' 'Graupel,' and 'Ice Crystal' categories through the use of the SNDI algorithm. Further progress in this regard would benefit from improvements in the SNDI algorithm (and/or particle imagery), and better definition on 'Spheres,' 'Graupel,' 'Hexagonal flat plate crystals,' and 'Dendrites.'

Examination of the aircraft-sensed regions of SLW found that NEXRAD signal returns were present, in contrast to the previous research consensus. In addition, for the first time in winter storms, the hydrometeors producing distinct signatures to a dual pol NEXRAD (KBUF) radar have been verified by in situ aircraft measurements.

Examination of HCA relative to SLW found that 'Dry Snow' and 'Unknown' categories have significant regions of potential icing hazards. The 'Unknown' category has distinct radar signatures that can be utilized to reclassify some of these 'Unknown' regions. Work has already begun to implement one of these subdivisions into a 'Hex Plate' category within HCA. Distinguishing 'Dry Snow' from 'Supercooled Drizzle,' however, remains a challenging task for dual polarization radar because both targets are quasi-isotropic. This underscores the challenge to extract a mixed-phase subclass from 'Dry Snow.'

In addition, SLW present in cloud droplet form in layers only a few hundred meters thick can result in serious loading on aircraft surfaces if exposure to riming conditions is sustained.

In terms of NEXRAD operations, the clear air scanning mode in NEXRAD provides a marked improvement in the detection of regions with a verified icing hazard. This finding also highlights the advantage to maintaining clear air scanning in winter storm situations where broad areas of icing are a concern.

SLW in cloud droplet form can be the seed for detectable radar echoes from regions with icing hazard, via cloud microphysics that are well understood. The two main processes are the Bergeron-Findeisen Mechanism and supercooled droplet growth by coalescence. Evidence for this association has been found in the radar comparison with aircraft-measured SLW, with the earlier NEXRAD PIREP comparisons, and with the space-time (4D) analysis of S-band reflectivity in verified icing zones. Cloud microphysics provide a reliable means to enlarge particles to S-band radar targets and generate NEXRAD reflectivity given the high percentage in the presence of SLW.

9. FUTURE WORK AND RECOMMENDATIONS

9.1 AIRCRAFT VERIFICATION IN THE +ZDR 'BRIGHT BAND'

One aspect of the three aircraft missions that has been conspicuously neglected in the verification context is the +ZDR 'bright band.' A large body of evidence has accrued from ground-based radar observations (Kennedy and Rutledge, 2011; Williams et al., 2011; 2015) for the robust presence of this dual pol target, which has been interpreted as arising from favorably oriented dendritic crystals in water saturated conditions. From the standpoint of icing hazard, these inferred layers of icing potential can be many hundreds of meters and can extend laterally (in wintertime warm frontal situations) for hundreds of kilometers. The existence and magnitude of SLW in such layers needs to be verified by directing the aircraft to these altitudes and making deliberate horizontal traverses over long distances. The use of the 'porpoising' maneuver may also be helpful in establishing the vertical variation of the LWC. Fleeting instances of these +ZDR 'bright band' conditions were noted in two of the icing missions as stated earlier in the report, but for a variety of reasons the feature was not well observed.

9.2 ASCENT RATES IN WINTER STORMS

One of the most elusive measurables in all of meteorology is the ascent speed of the air in precipitating systems, and most notably in winter storms. These ascent speeds in shallow-slope warm frontal lifting can amount to tens of centimeters per second, but that is the level of importance in establishing the disequilibrium between provision of SLW by condensation in the ascent and the take-up of the same SLW by vapor deposition on ice particles (e.g., Korolev and Mazin, 2003). We can make progress in estimating the ascent speeds by quantifying the frontal slopes (from models) and the upslope winds (from both models and direct observations). PIREPs will be useful in comparing the prevalence of icing hazard in situations with exceptional ascent rates calculated on the basis of these two other parameters.

9.3 4D ANALYSIS WITH NEXRAD OBSERVATIONS

A few examples have been shown based on the case studies for individual flights that local growth in reflectivity in a winter storm may signal the presence of SLW. A tracker of storm growth/decay that has been used successfully with NEXRAD radar data in summer weather conditions to distinguish large scale advection from local changes needs to be applied to winter storms. The challenge here for detecting local changes in winter is that both the ascent speeds and the concentrations of supercooled water are substantially smaller than in summertime conditions. On the other hand, the horizontal scales of the SLW anomalies have been shown to be larger in winter and that may help in quantifying the local changes and identifying the hazardous icing zones. The Wisconsin case provided evidence of structure in weak returns.

9.4 POTENTIAL USE OF CROSS-CORRELATION TRACKING

Four dimensional analyses of radar quantities related to interpretation of a potential icing hazard could be aided by application of a feature tracker. This would support monitoring trends in area coverage and intensity of distinct features such as radar reflectivity and differential reflectivity. That, in turn, suggests an additional dynamic would be available when assessing a potential icing hazard. LL developed a cross-correlation tracker (Chornoboy et al., 1994) used to track envelopes of radar returns along with separate tracking of features within the envelope. The tracker concept is behind the storm motion capability in the Corridor Integrated Weather System (CIWS) (Klingle-Wilson and Evans, 2005) that LL developed for the FAA. CIWS also includes a growth and decay capability analogous to intensity changes. These CIWS-integrated concepts could form the basis for similar approaches targeted to potential icing hazards.

As noted, SLW in cloud droplet form is expected to be an invisible radar target at S-band (NEXRAD). However, SLW in cloud droplet form is the seed for larger radar detectable hydrometeors, whether by collision/coalescence to form SLD, or by an active Bergeron process to form larger ice crystals that continue to grow by accretion of SLW. On this basis, one can expect that storm regions with SLW in cloud droplet form will often be growth regions for reflectivity. Evidence for this expectation is included in this report and provides additional incentive for developing a tracking capability aimed at localizing growth regions in winter storms.

Figure 9-1 shows the CIWS depiction of the weather coverage and intensity for the Buffalo, NY, area on February 19, 2013 at 1415 UT. This time corresponds to the 4D analysis demonstrated for this report. As determined by CIWS algorithms for surface conditions, green hues represent light rain, pink hues represent mixed precipitation, and blue hues represent snow. Darker colors indicated more intense precipitation. The area coverage is determined from a mosaic of NEXRAD non-dual pol radar data. From tracker information, forecast contours are used to project positions of identified envelopes of weather: blue at 30 minutes, magenta at 60 minutes, and white at 120 minutes. Yellow arrows have been added to associate the forecast contours to the originating weather envelopes. The tracker-based contour progressions (southwest to northeast) agree with the observed trends in the demonstrated 4D analysis of this case. Applying tracker concepts directly to the underlying dual pol radar quantities could benefit the IHL product's fidelity.

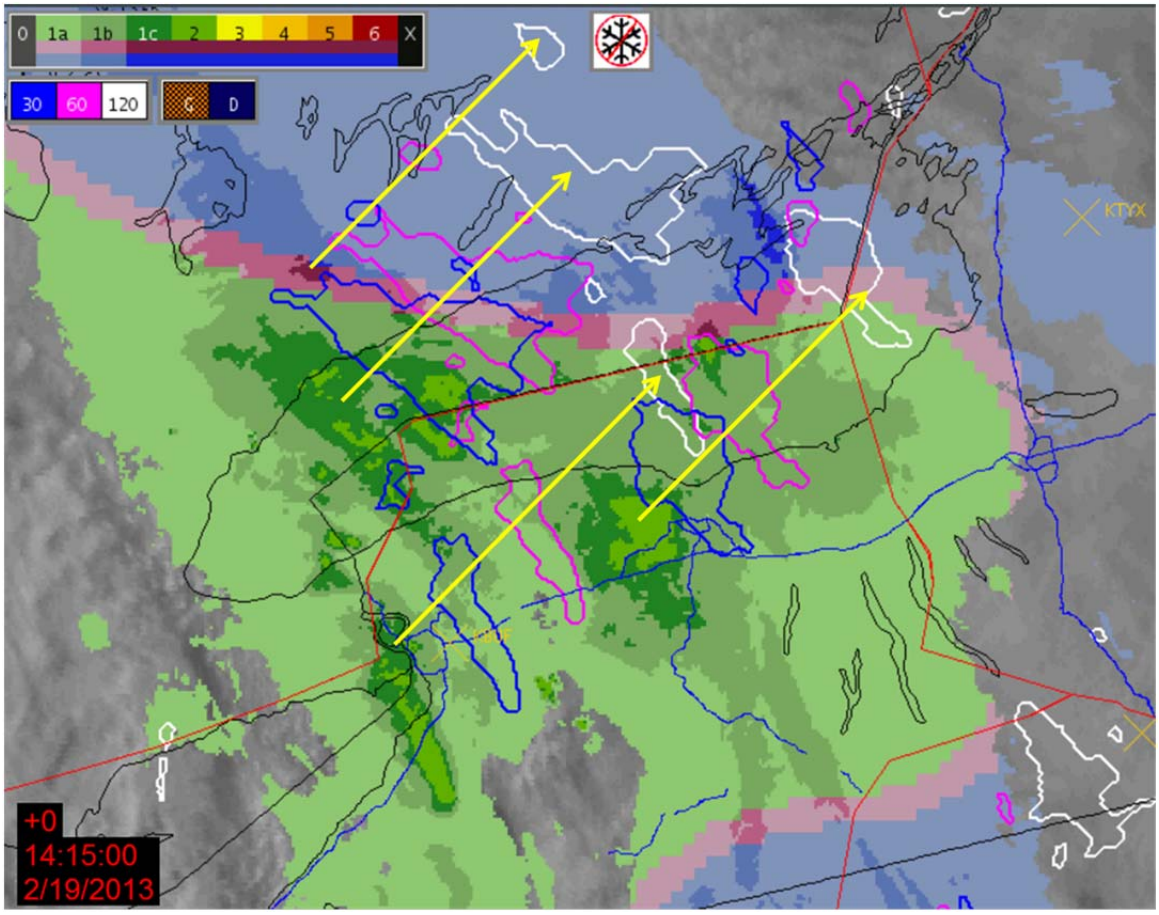

Figure 9-1. A CIWS depiction of winter weather coverage and intensity in the Buffalo, NY, area for February 19, 2013 at 1415 UT.

9.5 SUBDIVISION OF DRY SNOW AND UNKNOWN HCA CATEGORIES

It is clear from the in situ observations and previous PIREP analyses that the 'Dry Snow' and 'Unknown' categories are frequently associated with significant in-flight icing. The breakdown of SLW by HCA category (Section 7.4) illustrated that the 'Unknown' category, while mostly free of SLW, also had about 30% of the time where SLW was significant ($\geq$0.1 g/m^3). The challenge is to develop new categories that will reclassify these 'Unknown' regions. One area identified by careful scrutiny of the SNDI data is that hexagonal (hex) flat plates are found in regions where there is either no SLW or very weak amounts. Developing this new 'Hex Plate' category using the information derived from the in situ and NEXRAD data is an important step to isolating the SLW-laden 'Unknown' regions. 'Dry Snow' is an

abundant category within HCA, and as identified in the SNDI and SLW comparisons, encompasses a wide variety of particle types and regions with and without SLW. While various methods were examined in this study, more observations need to be made to subdivide the 'Dry Snow' category and identify regions of SLW. For that, 4D trending might be more effective than singular PPI examination of dual pol parameters.

APPENDIX A
ALTERNATIVE ICING MEASUREMENTS

Several other data sources are useful, to varying degrees, in identifying in-flight icing hazards. These methods are also being utilized for possible modifications to HCA classes and for verification of in-flight icing regions. None of these methods are as valuable or as accurate as in situ aircraft measurements from the NRC aircraft. However, they are presented here because these alternative methods provide surrogate information to broadly verify algorithm performance. They also represent the best viable alternatives to in situ aircraft measurements, and LL has taken steps to utilize them.

A.1 PIREPS FROM COMMERCIAL AIRCRAFT

One of the most valuable verification tools outside of in situ experimental aircraft measurements are icing PIREPs that are voluntarily logged by standard commercial aircraft on a daily basis. PIREPs provide direct observations of icing conditions, including type, severity, and affected flight levels and are obviously valuable for pilots following in the path of the reporting aircraft. Figure A-1 illustrates the frequency of all icing-related PIREPs from 2012. Not surprisingly, the highest density of reports is along typical air routes, and there are more reports in the northern than southern latitudes.

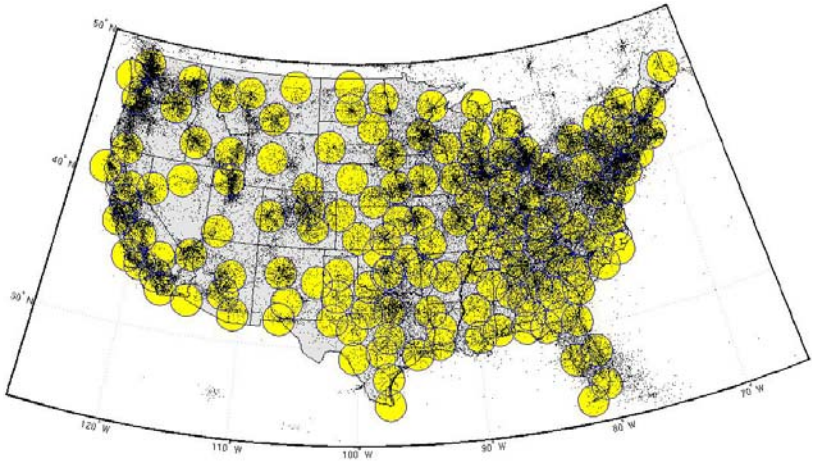

Figure A-1. Distribution of icing-related PIREPs from 2012 (black dots) relative to 125 km range of NEXRAD coverage (yellow circles).

Icing reports are based on visual inspection of the aircraft by the flight crew and include information on the type of icing (clear, rime, or mixed) and null to report that no icing is occurring. The

PIREP also provides an estimate of the icing severity on an increasing intensity scale of 1 to 8 (Table A-1). In most aircraft, this estimate is based on visual cues of airframe icing, but newer aircraft utilize the intensity of the current to the external heaters as an indicator.

TABLE A-1

PIREP Icing Severity Reporting Categories

Icing Severity Level	Description
1	Trace
2	Trace-Light
3	Light
4	Light-Moderate
5	Moderate
6	Moderate-Heavy
7	Heavy
8	Severe
–1 or –9	Unknown

Icing reports are reported only in areas where aircraft have flown but are not mandated. Therefore, the reporting of events, while broad in coverage area, is still sparse relative to the overall icing hazard. In addition, the reports are either reported over the radio or downloaded via the Aircraft Communications Addressing and Reporting System (ACARS). This manual processing of the observation frequently delays the report, and specific information can be incorrect or outdated (Bernstein et al., 2007). Figure A-2 illustrates the delayed reporting problem. Pilots often delay their report until they have safely left the icing region. So, while the report includes estimates of what level icing began and ended, the latitude/longitude of the report itself may not reflect the icing location. Corrections to observations or buffers for where the report is valid are often made to compensate for these errors. Nevertheless, these reports are valuable because they are currently the only routine means for verification of in-flight icing conditions and they provide coverage where aircraft fly (FAA 2013a). PIREPs have also been utilized to score the NEXRAD IHL algorithm, as they provide the best available "truth" (with an assigned space-time buffer) as to where icing is actively occurring (see Appendix B). A recent trend in the commercial aviation industry has been to completely shut down flight operations in the presence of the larger winter storms, resulting in complete silence regarding PIREPs. This proactive stance certainly has many benefits, but it has the undesirable effect of limiting icing PIREP observations during these extreme events.

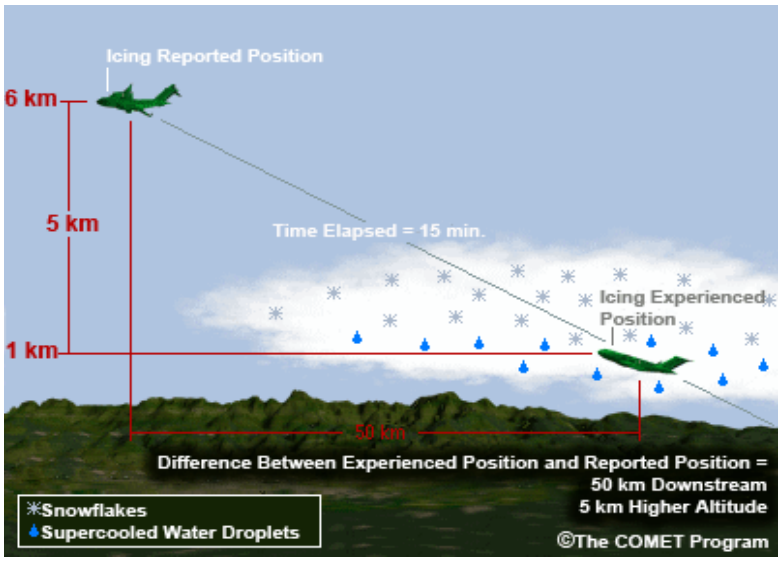

Figure A-2. PIREP icing report location issues (courtesy of COMET program).

A.2 NTSB ACCIDENT REPORTS

Unfortunately, today's icing detection and prediction technology can still result in aircraft that find themselves in hazardous icing situations. From January 2011 through December 2013, the National Transportation Safety Board (NTSB) investigated and reported on over 35 incidents and accidents caused or associated with icing conditions. These accidents provide absolute identification of the in-flight icing hazards that the NEXRAD algorithm development effort is designed to warn against. This report details an incident where a Wisconsin General Aviation pilot whose windshield ices up must be guided to a safe landing (Section 7.2). That guidance was at the expense of commercial air carriers that had to make way for the distressed plane. Thankfully, since the pilot landed the plane safely, that case is not in the NTSB accident database – but the nature of the comparisons LL is able to do with this case mirrors what can be done by looking at NTSB cases. By examining the accident details in conjunction with NEXRAD radar measurements and NEXRAD HCA and IHL output products, LL can validate how well the algorithms are performing, and, if necessary, how they might be improved to provide improved response to such cases. As with the in situ measurements, the NTSB cases allow LL to track changing conditions over time and altitudes.

Table A-2 lists the accident/incident locations and shows the number and types of accidents that have been reported from 2011 through 2013. While these cases are valuable, they represent a very small portion (and extreme impacts) of the overall hazard and can only be used to spot-check algorithm performance. In addition, the active icing region is captured only in a gross sense as for example "ice started building up on the windshield" or "pilot climbed to 10 kft to get above the weather." These

anecdotal comments are useful for identifying a general hazard and location, but lack the specificity and details of the in situ aircraft observations. An untapped resource, though, is having access to the investigators and their documentation that likely includes detail of interest regarding development of an icing hazard product.

TABLE A-2

NTSB Icing-Caused or Icing-Related Accidents 2011–2013

City	State	Date	Deaths	Injuries	Uninjured
Part 91 – General Aviation					
Soldotna	AK	12/4/2013		Minor(2)	
Yellow Pine	ID	12/1/2013	5		
Cedaredge	CO	11/19/2013	1		
Derby	KS	10/18/2013	2		
Amarillo	TX	12/9/2012	2		
Detroit Lakes	MN	12/7/2012			6
Bondurant	WY	11/17/2012	1		
Laramie Peak	WY	10/9/2012	4		
Colorado Springs	CO	10/5/2012			1
Glencoe	MN	3/21/2012	3		
Hayden	CO	2/19/2012	2	Serious(4)	
Amory	MS	2/14/2012		Serious(1)	
Morgan	UT	2/9/2012	2		
North Venon	IN	1/21/2012	2		
Brewster	MA	1/15/2012	2		
Denton	TX	12/20/2011	1	Serious(2)	
Morristown	NJ	12/20/2011	5		
Bryan	TX	12/19/2011	5		
Pampa	TX	12/9/2011			4
Silverton	CO	12/3/2011	4		
Midland	TX	12/2/2011		Serious(1)	
Casper	WY	11/18/2011	1		

Ulysses	PA	11/17/2011		Serious(4)	
Peru	WV	10/2/2011	3		
Gray	TN	6/15/2011			2
Taos	NM	5/20/2011	1		
Rock Springs	WY	5/18/2011	2		
Daggett	CA	3/20/2011	3		
Butte	MT	3/19/2011	1		
Romeoville	IL	2/21/2011			1
PART 135 – Commuter Aircraft/Props					
Payson	AZ	12/18/2012	1		
Anchorage	AK	3/5/2012			6
Kwigigillingok	AK	12/21/2011		Minor(1)	
Springfield	IL	1/6/2011		Minor(2)	4
PART 121 – Commercial Air Carriers					
Dayton	OH	1/31/2011			32

*Each of these accidents had verified icing on the aircraft, although it may not have been the primary cause of the actual event.

A.3 GROUND OBSERVATIONS

While the goal of the icing algorithm is to detect in-flight icing regions above the Earth's surface, the type of precipitation and, in particular, the crystal types within frozen precipitation at the ground can yield significant clues about the icing (or non-icing) conditions above the ground. LL has occasionally been collecting detailed ground observations of precipitation types and rates during local Boston events in an effort to further utilize these observations for algorithm verification. As shown in Figure A-3, these observations were initially gathered by visual inspection of the precipitation. Observers would attempt to discern the type of frozen particles (dendrites, irregulars, needles, graupel, aggregation) and whether those particles were rimed (coated in ice).

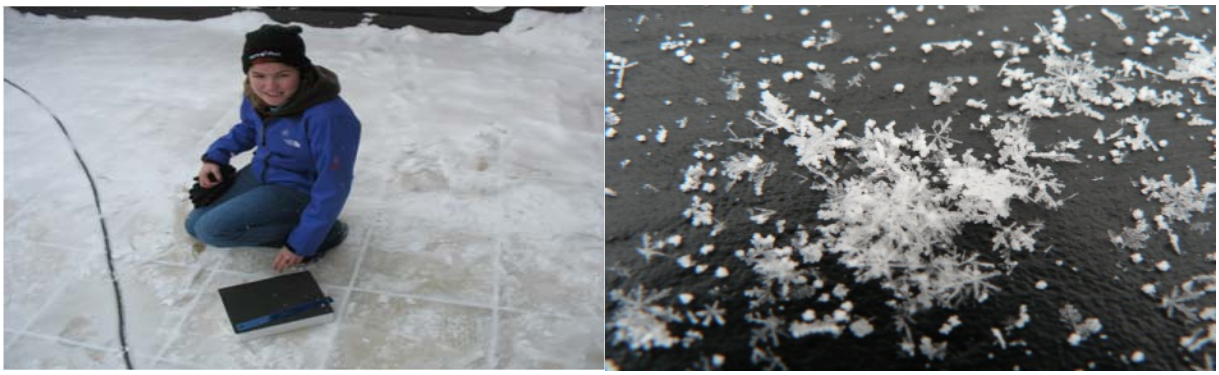

Figure A-3. Manual observations of ice particles at Valparaiso, IN (left) and eastern MA (right).

However, visual verification and documentation of riming is difficult due to the often miniscule features used to identify riming of an ice particle. Frozen water droplets typically associated with riming are nearly indistinguishable from the ice particle itself without magnification. Imaging a particle for more sophisticated and detailed analysis is possible using a point-and-shoot optical zoom camera. Unfortunately, macro modes vary widely from one camera model to another, and the zoom capabilities limit how close one can get to a particle while keeping it in focus, negating the zoom in some cases. To overcome these issues, an inexpensive lens from a single lens reflex (SLR) camera, a tripod, and spacer were combined to obtain high resolution images of ice particles.

In a conventional camera, light from a scene passes through a camera lens, and in the process, the resulting image is flipped and scaled to the size of a camera's digital sensor. A simplified example of this concept using a removable SLR camera lens is shown in Figure A-4(a). The scaling feature can be exploited by reversing the lens, resulting in the magnification of small objects of interest as illustrated in Figure A-4(b). An external SLR lens used in this manner acts as a large magnifying glass and can be used with any point-and-shoot camera to capture high-resolution images of frozen particles for verification of rime. A Soviet-made Helios 44M-5 SLR lens was used to magnify and document ice particles during the 2014 winter weather verification process.

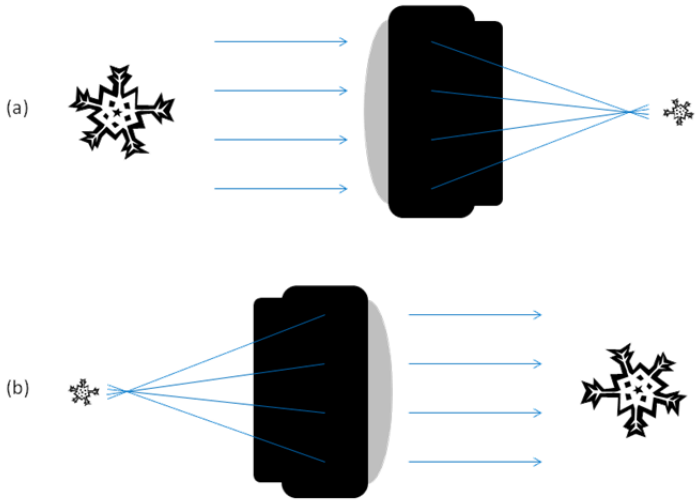

Figure A-4. Illustrations of how imaging of an object is transformed when passing through a camera lens utilizing (a) a standard and (b) an inverted lens configuration.

Referring to Figure A-5, for the 2013–14 winter observations, the apparatus was positioned with the camera set to maximum zoom and the edge of the camera lens positioned at the edge of what is normally the front of the SLR lens. An opaque spacer held the reversed lens at the proper distance above the crystal particle to analyze for focusing purposes. The spacer's color was advantageous, as external light was diffused evenly to light the particle for improved image quality. Finally, the camera was held in place using a flexible tripod to position the extended lens right next to the reversed SLR lens. A comparison between the camera in macro mode and the camera with full optical zoom and the reversed SLR lens shows an increase in magnification by a factor of 8. The test images are shown in Figure A-6.

Figure A-5. Camera apparatus for imaging frozen particles.

Figure A-6. Relative magnification standard (left) versus inverted lens (right).

The custom setup was utilized during several winter storms in February 2014. Several members of the LL NEXRAD team made observations of crystals in various locations in Massachusetts and New Hampshire. A winter storm on February 13–14, 2014 produced crystals where riming was visible at some observers' locations, while others observed little to no riming. Figure A-7(a) shows an example of a crystal that was imaged in New Hampshire with no riming, indicating an absence of SLW in the

atmosphere traversed by the crystal. The crystal in Figure A-7(b) from the February 18, 2014 winter storm shows heavier riming on a crystal. These frozen liquid water drops on the crystal verify the existence of SLW aloft in the atmosphere.

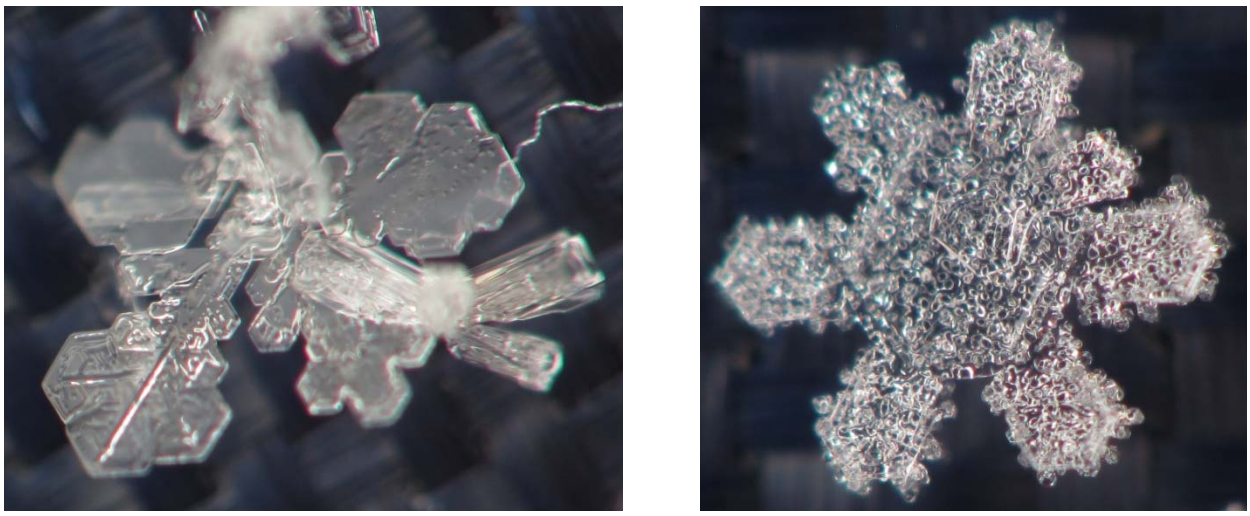

Figure A-7. Ice particle images from Nashua, NH, with enhanced camera configuration showing (a) ice crystal without riming on February 13, 2014 (left) and (b) ice crystal with riming on February 18, 2014 (right).

As evidenced by the case above, ground observations with imagery have utility in classifying storms that do and do not have SLW in a crystal environment and in identifying general types of ice particles (or rain drops). While rimed ice particles at the surface confirm that SLW was available in some layer aloft, it yields little information about the altitude of that icing region. It does suggest scrutiny of the NEXRAD data is warranted to search for dual pol parameter combinations associated with icing conditions as revealed by the in situ observations. The value of the ground observations are a) they are inexpensive, b) they generate much discussion within the LL NEXRAD team regarding the icing potential and underlying microphysics, and c) they can be used as a secondary verifier of icing potential in the presence of near-collocated PIREPs. Their value to date has been limited regarding direct algorithm validation, but often leads to examination of the dual pol parameters aloft for knowledge-building regarding possible variability in algorithm thresholds.

This page intentionally left blank.

APPENDIX B
PIREP STUDY

Despite the aforementioned uncertainties associated with PIREPs described in Section A.1, these reports cover a broad area and were the only source of information routinely available used to validate the baseline version of the NEXRAD Icing Hazard Levels (IHL) algorithm (Hallowell et al. 2013). This version determines the vertical extent of the icing layer top and bottom altitudes from the presence of the HCA 'Graupel' class detections found in each NEXRAD elevation beam at the same range-azimuth bin. Detections can be further extended in height to match any high icing interest potential region determined from favorable temperature and relative humidity conditions predicted by the Weather and Forecasting Rapid Refresh model. IHL detections consist of icing layer bottom and top altitude components, but they are portrayed in the two dimensional plane once per radar volume. This study provides an assessment of IHL algorithm performance from several NEXRADs over different geographical regions. The secondary objective of the study was to analyze the NEXRAD dual pol products within the radar coverage area associated with each PIREP.

Lincoln Laboratory operates a configurable Open Radar Product Generator (ORPG) clone network system capable of running up to 40 radar sites in real time. This capability allows for product evaluation over different geographic and climatological regions. The NEXRAD IHL algorithm was installed in each ORPG system to determine functionality and robustness prior to delivery to the NWS Radar Operations Center (ROC) in August 2012 and system-wide deployment in the summer of 2014. The LL network allows for archiving of the IHL and dual pol products on a daily basis. Prior to determining which radar sites to operate within the network, a frequency map of PIREP locations relative to each NEXRAD site was constructed for a three-year period between 2010–2012 and is shown in Figure B-1. Circles denote NEXRAD sites color-coded according to the fraction of PIREPs located within 300 km. Highest PIREP frequencies were located in the Northeast, Great Lakes, and Pacific Northwest states, and the red enclosures denote the 23 radar sites that were configured to run in the LL ORPG network for this study. IHL was evaluated over a two-month period between February–March 2013. Unfortunately, the KIWX (North Webster, IN) and KDTX (White Lake, MI) NEXRADs, showing the highest PIREP frequency, were not converted to dual pol at the time of this study.

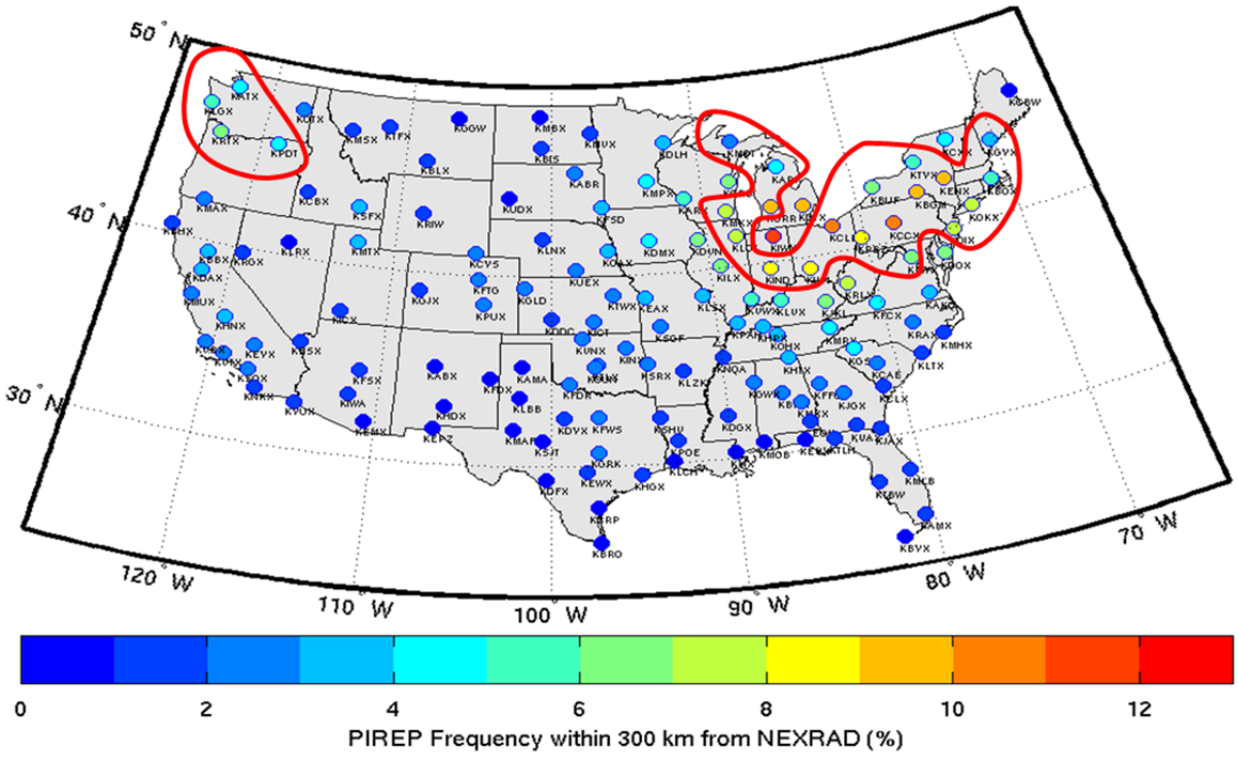

Figure B-1. Map of PIREP location frequency color-coded according to the number of reports within 300 km from each NEXRAD site for all reports received from 2010–2012. The red enclosures show the 23 NEXRAD sites where IHL-PIREP comparisons were made in the interval February–March 2013.

To account for PIREP reporting uncertainties in time and space (see Figure A-2) and with knowledge that icing can exist in layers over long distances in stratiform cloud systems, a cylinder of interest centered at each PIREP location is constructed to define an icing airspace associated with each report. An illustration of the cylinder geometry is shown in Figure B-2. For icing PIREPs, the cylinder is bounded by a radius of 50 km and 1 kft vertically to the flight level(s) reported by the pilot. For null PIREPs, locations where no icing was observed by the pilot, the cylinder is reduced to a radius of 10 km and 0.5 kft vertically. The smaller cylinder size of null PIREPs was chosen to limit an extension into nearby precipitation areas where icing may exist. The cylinder outline is extended to the surface to create a footprint from which an overlap with IHL detections can be compared. These comparisons were made for each PIREP in which any single NEXRAD elevation beam intersected the cylinder, and whether the IHL component icing altitudes matched any portion of the cylinder vertically. Example cylinder geometries, shown in magenta and blue in Figure B-2, denote regions where any PIREP-IHL overlap is evaluated for an icing and null PIREP, respectively. Comparisons were made for all radar volumes scanned ±15 minutes to the PIREP time and for all reports located within 125 km from each NEXRAD site.

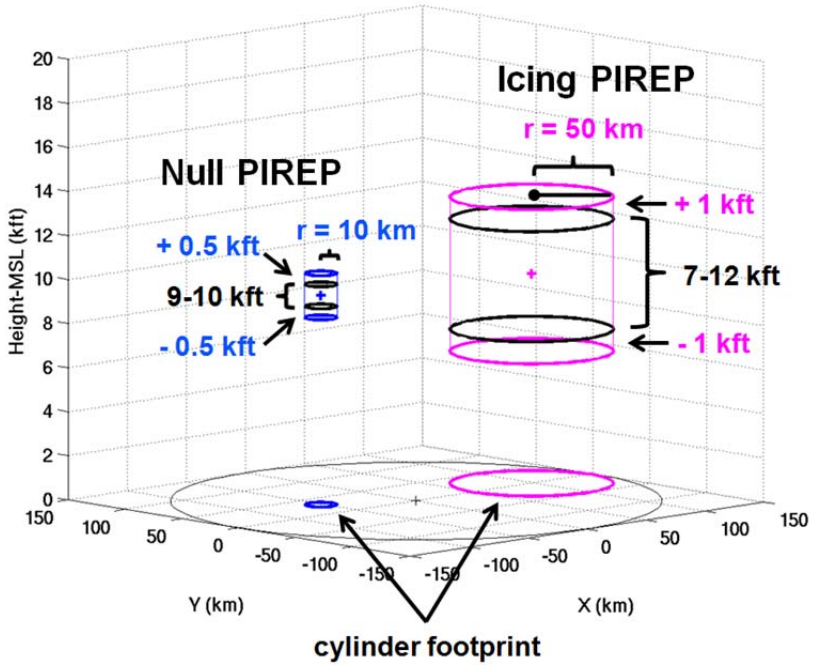

Figure B-2. Three-dimensional cylinder of interest geometries used to define the icing airspace or lack thereof associated with icing PIREPs (magenta) and null PIREPs (blue), respectively. Example PIREP flight levels are shown in black. The cylinder areas and boundary outlines depicted as footprints onto the surface plane were used in validating the IHL detections.

For all icing PIREPs, IHL performance was evaluated into the four scoring scenarios shown in Figure B-3. The top row shows a three-dimensional view of the IHL product in cyan and PIREP cylinders in magenta. The bottom row contains a footprint of each cylinder onto the surface plane. Scoring categories are defined as follows:

- HIT – IHL detection(s) resides in cylinder footprint and altitudes overlap
- ABOVE – IHL detection(s) resides in cylinder footprint, but IHL bottom altitude is above cylinder top altitude
- BELOW – IHL detection(s) resides in cylinder footprint, but IHL top altitude is below cylinder bottom altitude
- MISS – No IHL detections reside in cylinder footprint

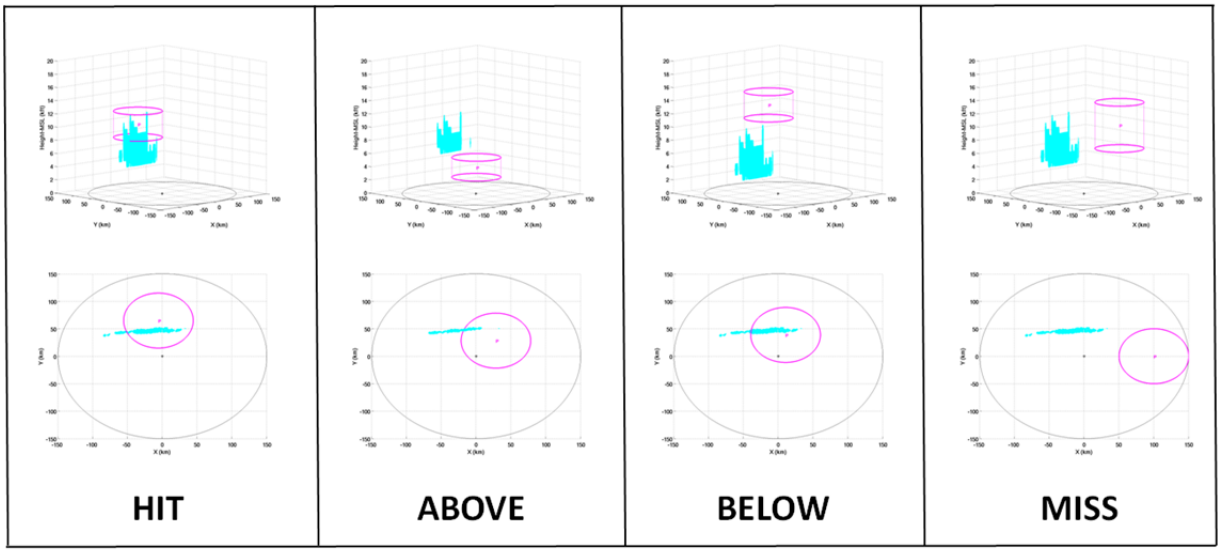

Figure B-3. Four possible scoring categories recorded for each icing PIREP-IHL comparison. IHL detections are shown in cyan and PIREP cylinders are shown in magenta. The top row shows the three dimensional view to determine overlap in altitude, and the bottom row shows a projection of the cylinder footprint on the surface plane.

Figure B-4 illustrates the two scoring categories recorded for all null PIREPs. As in Figure B-3, the top (bottom) row shows IHL detections and cylinders in a three (two)-dimensional view, respectively. Scoring categories for null PIREPs are defined as follows:

- CORRECT NO DETECT – No IHL detection resides in cylinder footprint
- FALSE ALARM – IHL detection(s) resides in cylinder footprint and altitudes overlap

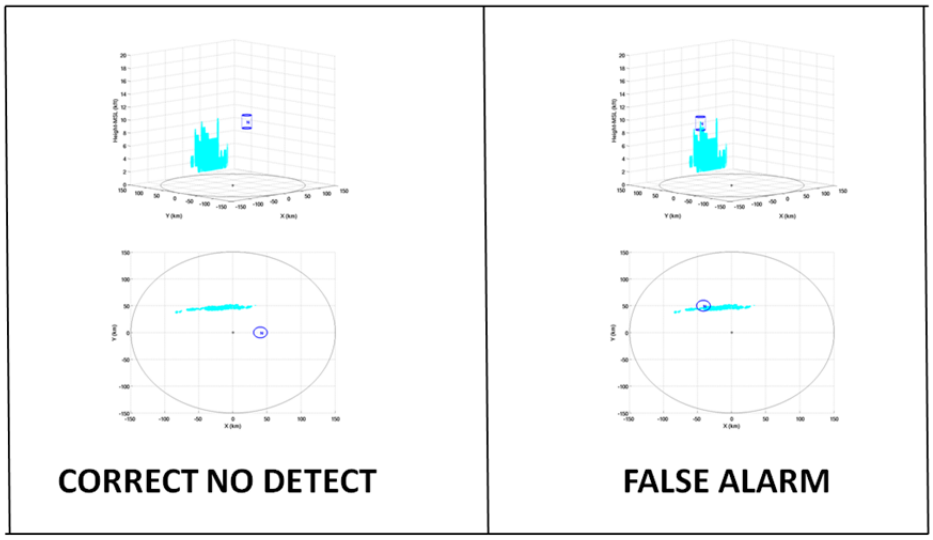

Figure B-4. Same as in Figure B-3 but showing the two possible scoring categories recorded for each null PIREP-IHL comparison.

The IHL algorithm performance was measured by computing the Probability of Detection (POD) and the False Alarm Rate (FAR) using the formulas shown below. A HIT is regarded as a complete match. IHL detections residing outside a PIREP cylinder and not within the footprint were not evaluated given the presence of icing (or lack thereof) was not determined. The FAR was calculated in this study, but the performance should be interpreted loosely. Null PIREPs are issued far more infrequently than icing reports, and as a consequence, a true measure of the IHL FAR cannot be obtained.

POD = number of HITs / number of icing PIREPs
FAR = number of FALSE ALARMS / number of null PIREPs

Over the two month period, 6,829 icing PIREPs and 507 null PIREPs were studied. Among all icing PIREPs, HC of 'Graupel' were detected in 16% (1,117) of the reports. Since the IHL baseline version only issues detections in the presence of graupel, the algorithm performance can only be judged on these subsets of reports. Among the PIREPs where 'Graupel' was present, IHL POD was 78% (869). A majority of the missed graupel cases were scored in the BELOW category. Future algorithm tuning of the model enhancement parameters should help to increase the IHL top altitudes in these cases allowing for a better overlap in altitude and an improved POD. The FAR among the null reports was 5% (26). While this result was encouraging, the importance of the result should not be given emphasis as per discussion of the caveats mentioned above.

Figure B-5 contains histograms of IHL POD and FAR performance for ***all*** PIREPs (reports that contained 'Graupel' and reports with no 'Graupel' for which IHL cannot detect in the baseline version) for each NEXRAD site analyzed in the study. Performance varies by site, with the highest PODs occurring at the radar sites (KATX, KLGX, KPDT, and KRTX) located in the Pacific Northwest states. Review on some of these cases revealed an abundance of HCA 'Graupel' detections associated with weather systems moving onshore and a characteristic difference from the graupel coverage observed with continental weather systems moving through other NEXRAD sites.

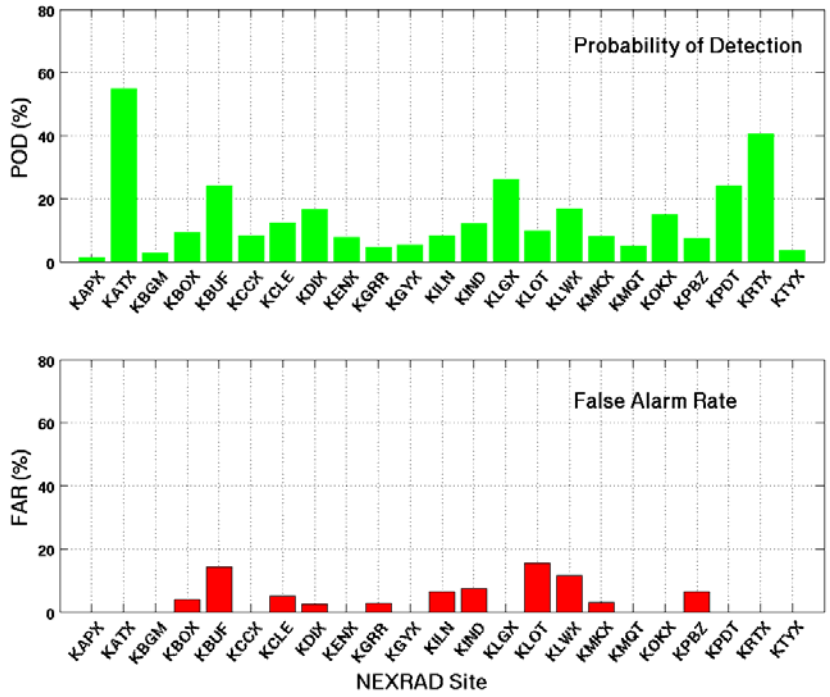

Figure B-5. Histograms of IHL algorithm performance for POD (top) and FAR (bottom) for each NEXRAD site in the study.

The second objective of this study was to evaluate the dual pol products among all elevation beam radar bins that intersect the PIREP cylinder. For this part of the analysis, the cylinder geometries were similar to those shown in Figure B-2, except the cylinder size for icing PIREPs was reduced to a radius of 25 km to limit analysis to an area more pertinent to the PIREP reporting location. The products studied include SMZ, ZDR, CC, KDP, and HC. The height of each radar bin was first converted from above ground level to mean sea level to match the flight level height convention reported by pilots, and then several standard statistical metrics were computed for each product among all valid radar bins and all volumes occurring within ±15 minutes to the PIREP time.

One important finding in this study was to determine the ratio of valid SMZ radar bins containing detectable echo among all bins that intersect the cylinder. These results are provided in the histogram shown in Figure B-6. Blue bars denote the frequency of all icing PIREPs located within 125 km from the NEXRAD sites categorized by the severity level encountered by the pilot. Severity levels 1–3, 4–5, and 6–8 denote trace to light, light-moderate to moderate, and moderate-severe to severe icing, respectively. The red bars denote frequencies of the PIREPs having some detectable SMZ among the radars bins intersecting the cylinder with the corresponding relative frequency percentages displayed above each bar. The figure shows Level 3 (light) icing is the most commonly reported severity level and that 80–90% of the PIREPs studied have some detectable echo. These results imply icing is frequently associated with detectable precipitation and strengthens the utility of icing detection with NEXRAD dual pol radars. However, no exercise was undertaken to quantify the utility at the time of this writing.

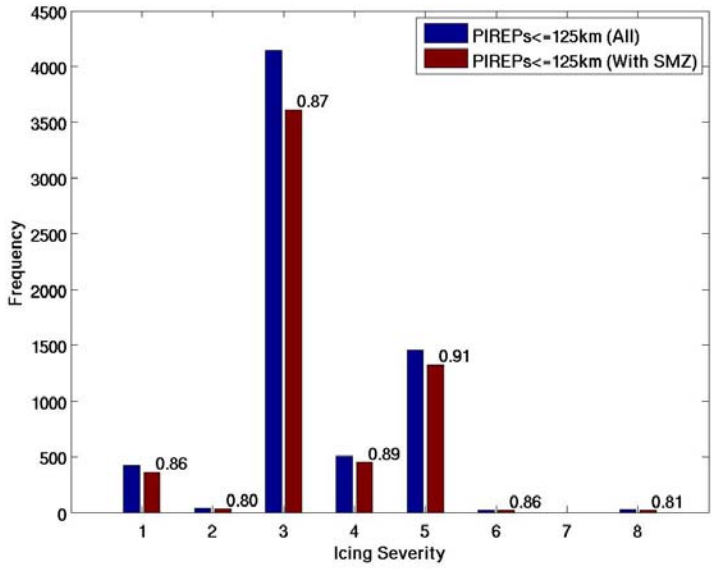

Figure B-6. Distribution of all PIREPs located within 125 km from NEXRAD sites grouped by icing severity level encountered by the pilot. The number of all PIREPs and those that contained some detectable SMZ is shown in blue and red, respectively, with corresponding relative frequency percentages displayed above the red bars.

The reflectivity results were separated further into the radar's VCP operational scan mode. Figure B-7 shows the frequency distributions of the SMZ associated with PIREPs in 5 dBZ intervals when the radar was operating in precipitation mode VCPs (upper) and clear air mode VCPs (lower). Distributions are shown for each severity level, increasing from trace icing (green) at the bottom to severe icing (red) reports at the top. The number of no detectable echo (NE) cases is shown in the far left bin in each chart. Independent of the VCP pattern, the greatest number of events had SMZ values between 0–10 dBZ. As

previously described in Section 7.3, these results show the importance of operating in clear air mode scanning during winter storms. The improved sensitivity of the radar allows detection of weaker reflectivity that would not otherwise be possible in precipitation mode VCP scanning.

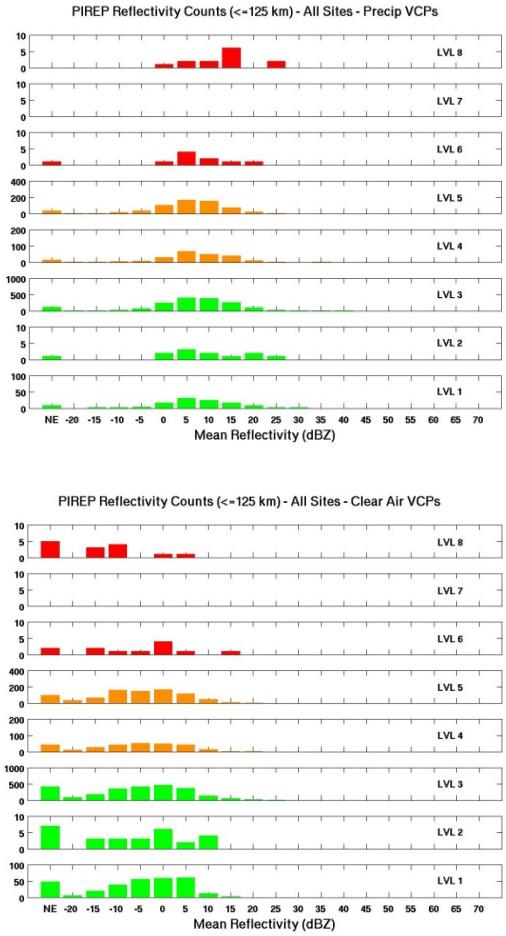

Figure B-7. Frequency distributions showing the number of PIREPs associated with SMZ for all reports within 125 km from all NEXRAD sites studied while the radar was operating in a precipitation VCP mode (upper) and clear air VCP mode (lower). SMZ values are binned into 5 dBZ intervals, and the number of reports where no detectable reflectivity was found is shown in the NE column in the far left. Distributions are separated by icing severity level from trace (green) at the bottom to severe (red) at the top.

APPENDIX C
S-BAND RADAR DETECTABILITY OF SUPERCOOLED WATER IN CLOUD DROPLET FORM

The most common manifestation of supercooled liquid water in the atmosphere is in small cloud droplet form. (This claim is substantiated by the Convair-580 observations discussed in this report.) The reason for this is simply that in natural conditions, the concentration of cloud condensation nuclei (CCN) greatly exceeds the concentration of ice nuclei. A long-standing problem in the world of operational weather radar (single or dual pol systems) is the expected absence of a radar return from regions containing supercooled water generally in cloud droplet form, and so the absence of any ability with radar to diagnose remotely the presence of an aircraft icing hazard. The well-known qualitative reason for this limitation is that the radar cross sections of liquid spheres with diameter D in the Rayleigh regime ($\lambda >> D$, typical for S-band radars like NEXRAD) is $\sim D^6$, and so the cross section for a droplet with 10 micron diameter is only 10^{-12} as large as that for a 1 mm diameter raindrop.

The relevant calculation can be made more quantitative in a scenario that is not infrequently duplicated in nature. Let the existing population of CCN in the boundary layer, in concentration N particles per cubic centimeter (cm^{-3}), serve as nucleation sites for cloud droplets as ascent proceeds. If the available supercooled water content M in g/m^3 is shared equally amongst all nucleation sites, then we have by conservation of mass:

$$M = N \rho (\pi /6) D^3 , \qquad \text{(C-1)}$$

where ρ is the density of liquid water.

The common manifestation of the optical phenomenon known as the glory in cloud tops undergoing gentle ascent is evidence that the distribution of cloud droplet sizes can remain monodisperse, with all new condensate shared equally among nucleation sites. If this were not the case, the different diffraction patterns from droplets with different sizes would overlap with each other and the organized colored rings with angular distance would get washed out, or 'whitened.' (In two of the aircraft flights in which supercooled water was documented, the glory was also documented in an over-flight segment, as shown in Figures 6-6 (for February 19, 2013) and 6-30 (for February 28, 2013)).

Solving equation (1) for the radar reflectivity ND^6 gives

$$Z = ND^6 = 36M^2/\pi^2\rho^2N , \qquad \text{(C-2)}$$

and solving (C-1) for the droplet diameter D gives

$$D = (6M/\pi\rho N)^{1/3} \qquad \text{(C-3)}$$

The log-log plot of Figure C-1 shows the behavior of radar reflectivity Z (from equation (C-2)) and droplet diameter D (from equation (C-3)) versus the CCN concentration, for two different values of supercooled water content M, 0.5 and 1.0 g/m^3. These values span the high range of LWC recorded by the Convair in winter storms. The CCN concentration varies over five decades from highly polluted continental values (10^5 cm^{-3}) at the high end, down through typical continental values of 10^3 to 10^4 cm^{-3}, down to typical maritime values (100 cm^{-3}), and further down one more decade to what we call 'ultra-clean' conditions, with a value of 10 per cm^{-3}.

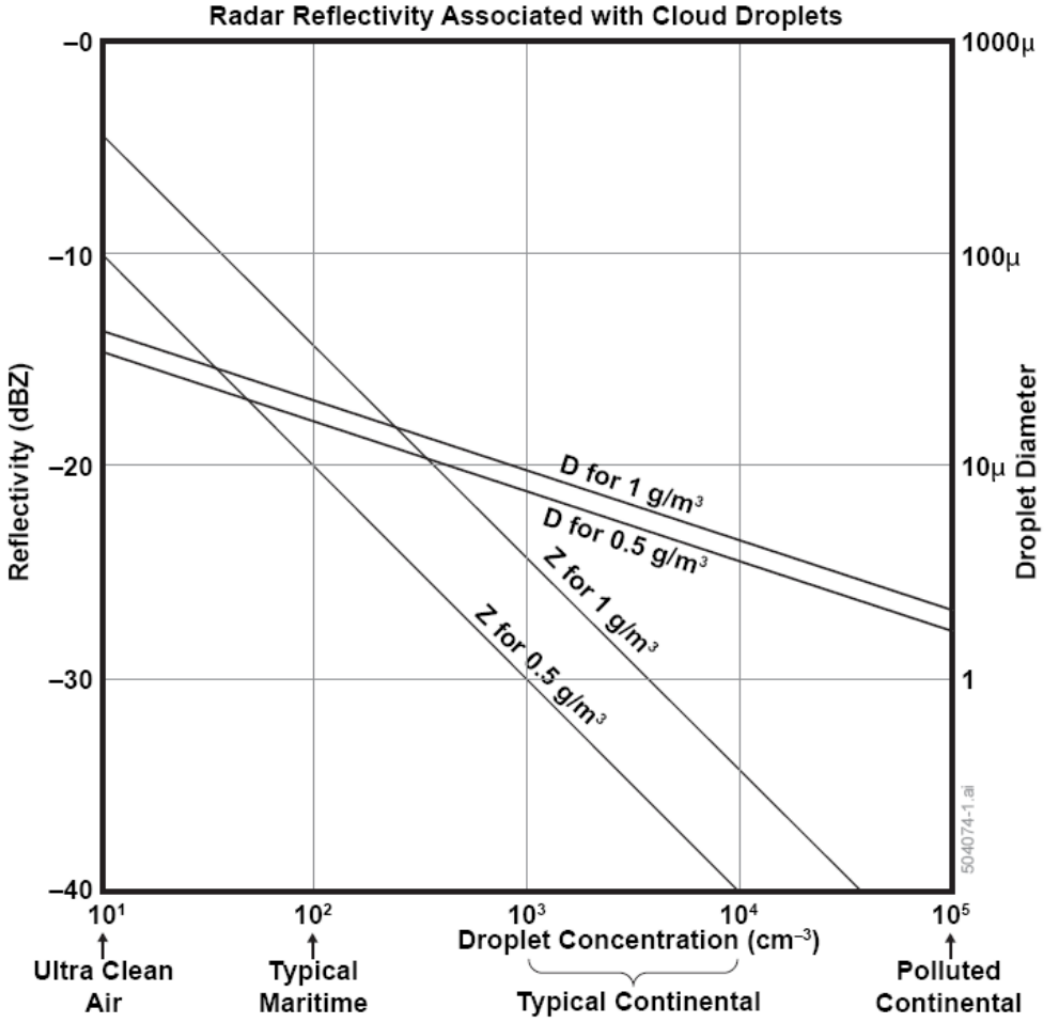

Figure C-1. Calculated radar reflectivity (Z) and cloud droplet diameter (D) based on the assumption that the available supercooled cloud water M (0.5 and 1.0 g/m^3) is shared amongst a concentration N of cloud droplets initiating on condensation nuclei.

Even with extreme assumptions in the winter storm context of 1 g/m^3 of total condensate and ultra-clean conditions, it is still not possible to achieve positive values of radar dBZ in this simple scenario. The maximum reflectivity value with these conditions is –5 dBZ. However, it should be noted that droplet diameters just reaching 40–50 microns are achieved in this case. These diameters are sufficient to make the cloud colloidally unstable by collision-coalescence (see for example: Houghton, 1985), enable the formation of SLD (supercooled large drops) and then the radar reflectivity (dBZ) could runaway to substantial positive values. It is interesting in this same context that even with ordinary maritime conditions, the expected cloud droplet diameters do not reach this expected 'runaway' threshold. In Appendix B, NEXRAD's capability to detect returns below 0 dBZ is demonstrated when the radar is operated in clear air mode.

When we address the surprising observation in this aircraft validation study that detectable S-band radar reflectivity is commonly present in regions documented to contain SLW (and hence potential icing conditions), two possible hypotheses come under consideration. The first is the possibility just discussed of runaway collision-coalescence in ultraclean conditions. (See also Cober et al., 2001.) The second hypothesis holds that the concentration of ice nuclei is sufficiently large to enable isolated ice particle growth to radar-detectable levels by an active Bergeron process. These two hypotheses will be distinguished on the basis of the available Convair observations, after the observational evidence for radar-detectable regions of SLW is presented in Appendix D.

This page intentionally left blank.

APPENDIX D
TREATMENT OF AIRBORNE X-BAND REFLECTIVITY OBSERVATIONS

Toward understanding what NEXRAD dual pol radar diagnosis was possible in regions of the atmosphere containing SLW, an extensive comparison between aircraft icing PIREPs and NEXRAD reflectivity measurements was undertaken. The results of that study (Appendix B) are summarized in Figure D-1 (reprise of Figure B-6). Here it is shown the number of icing PIREPs, in each category of icing severity, and the fraction of total reports for which some detectable NEXRAD reflectivity was found. The results shown here indicate that in 80–90% of cases, some detectable reflectivity was present. These findings are in marked contrast with the expectations in Appendix C based on the assumption that the SLW is in cloud droplet form.

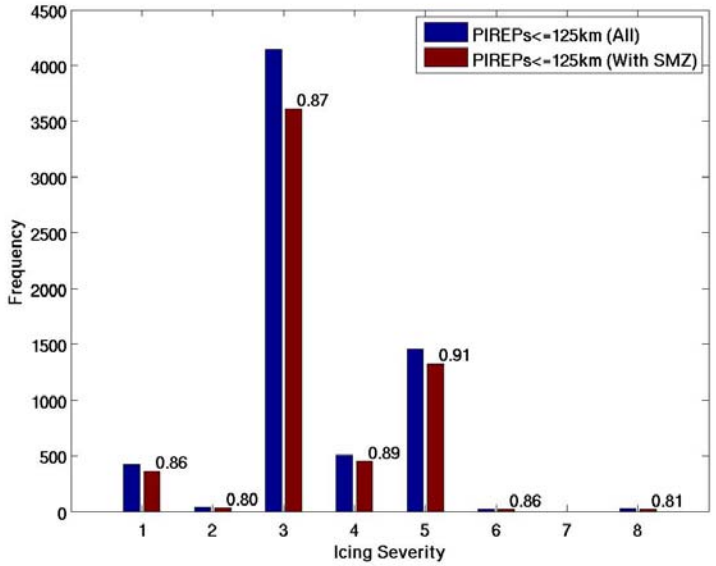

Figure D-1. Number of PIREP reports within 125 km from a NEXRAD and organized by the icing severity index (blue bar), with the red bar showing the fraction of total reports for which a detectable ground-based radar echo was present.

In routine checking of real-time NEXRAD radar displays across the U.S. by LL, a cluster of icing PIREPs was noted on May 8, 2014 south of the Ft. Worth, Texas, NEXRAD (KFWS). The four-panel display is shown in Figure D-2. The cluster of PIREPs is shown in the lower portions of all four panels as square or circle symbols (indicating age – circles older). Detectable radar reflectivity, at the level of

5–15 dBZ, is evident for the majority of PIREPs. It should be noted in this case that the more sensitive clear air scan was not in operation. If it had been, it is likely that all PIREPs would have been located in detectable reflectivity.

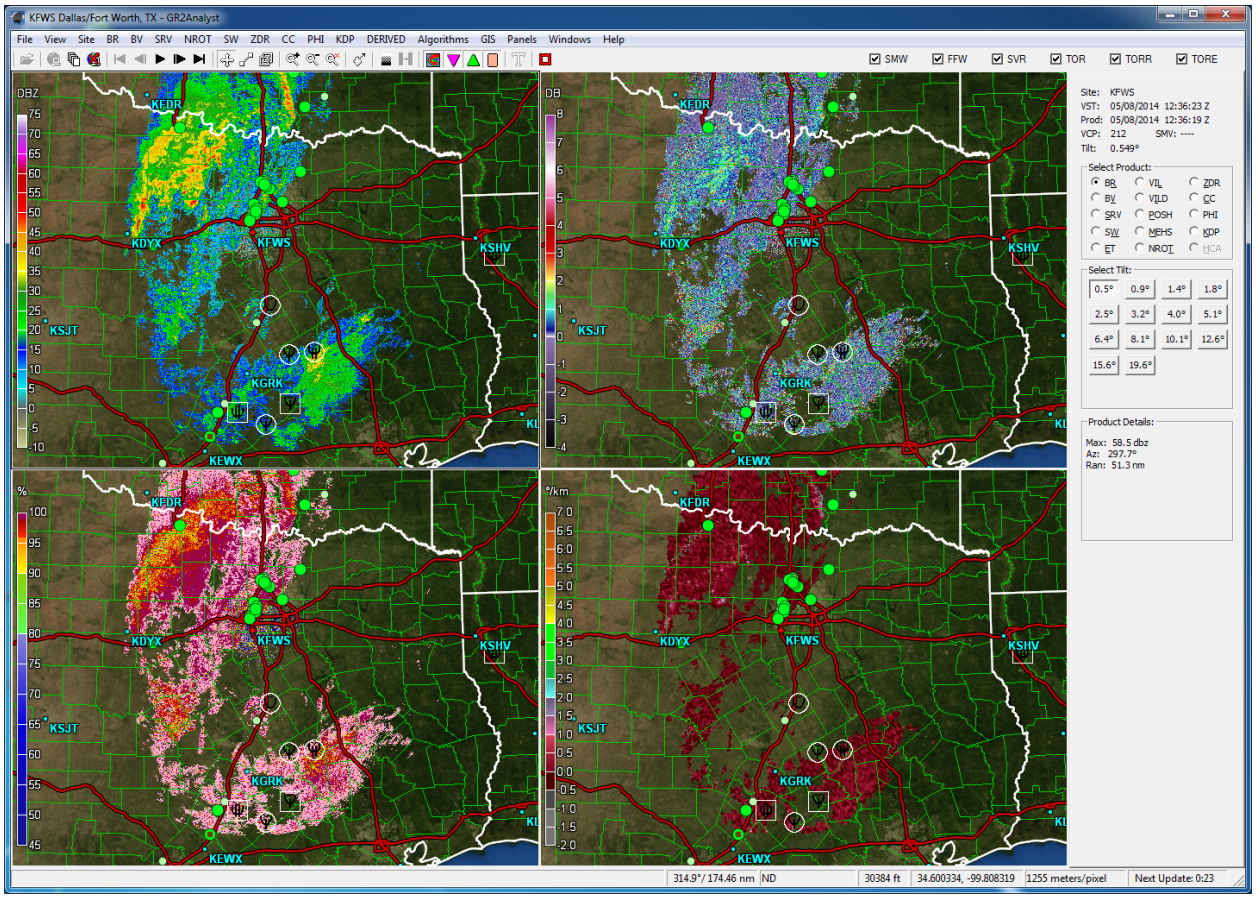

Figure D-2. Four-panel radar plot from the KFWS radar (Ft. Worth, Texas) for May 8, 2014 showing evidence for detectable radar reflectivity in the vicinity of a flurry of icing PIREPs (as symbols) south of the radar. In this Gibson Ridge display, shown are reflectivity (upper left), differential reflectivity (upper right), cross-correlation coefficient (lower left), and specific differential phase (lower right).

Despite these important hints about the relationship between icing conditions and radar reflectivity, a major limitation of the use of PIREPs for this purpose is their limited space-time resolution. When a PIREP is logged, no information is provided about exactly when the icing incident occurred relative to the time of logging. Since typical jet aircraft can travel 10–20 km in a minute, a modest offset in time of logging can result in significant uncertainty in the radar comparisons. Furthermore, the PIREP icing

severity scale is only semiquantitative and is much less desirable than a Convair measurement of LWC in g/m^3.

The onboard X-band radar data on Convair have been used to make improvements in relating radar reflectivity and the in situ icing hazard. X-band reflectivity is continuously available throughout these flights from volumes within a few hundred meters of where the SLW is documented with the Nevzorov probe, the FSSP sensors, and the Rosemount probe on the aircraft. Normally X-band data are undesirable in comparison with S-band data because of attenuation and possible Mie scattering effects, but in this application, the path length is short (~400 meters) and both the ice and liquid hydrometeors are sufficiently small that the Rayleigh regime is applicable. The nondimensional scattering parameter $2\pi a/\lambda$ at X-band ($\lambda = 3$ cm) is as small as ~0.1, even for particles with diameters (2a) of 1 mm. For hydrometeors with effective spherical diameters of many millimeters, some degradation in X-band reflectivity relative to S-band reflectivity is expected.

Toward organizing a data set on the X-band observations for comparison with the aircraft documentation on SLW, two steps were taken. In the first step, the X-band reflectivity range-binned data in the horizontal beam were studied as a function of the distance from the aircraft. (The data from the horizontal beam were used to avoid artifacts from the spatial gradients that are more prevalent in the vertical beam data.) It was found that the reflectivity estimates increased systematically from the aircraft to a range of ~400 meters and then leveled off to stable values when regions with quasi-uniform reflectivity on still larger scales were traversed by the aircraft. Thereafter, the measurements at 400 m were taken as the most appropriate estimates for comparisons with the other aircraft estimates.

The second step in the data organization was aimed at assessing the absolute calibration of the X-band reflectivity data. This was achieved by making scatter plot comparisons between the X-band reflectivity and the KBUF NEXRAD reflectivity when the latter sample was collected within a time window of ±120 seconds of the X-band sample. Figure D-3 shows the scatter plot for the flight on February 19. Despite the considerable scatter, the organized positive correlation between the two independent radar measurements supports the validity of the ground-based comparisons with the airborne data. The scatter itself in Figure D-3 can be attributed to the markedly different pulse resolution volumes at X-band (~2×10^3 cubic meters) and at S-band (2×10^5 cubic meters at around 50 km range and 1.5° elevation angle) and to the space-time mismatch in sample volumes. The strong tendency for the best fit line in Figure D-3 to run parallel with the 45-degree line of perfect match casts doubt on a leading role for Mie scattering in contributing to the discrepancy. Based on the foregoing considerations, we have concluded that the onboard X-band radar is out of calibration. For further comparisons with the airborne documentation of SLW, all X-band reflectivity measurements in Figure D-3 were corrected by a +8 dB offset resulting in comparisons that more closely resemble the 45-degree line of perfect agreement (results are shown in Figure 6-11 for the February 19, 2013 flight). The +8 dB offset correction was similarly applied to the X-band reflectivity measurements in the other flights.

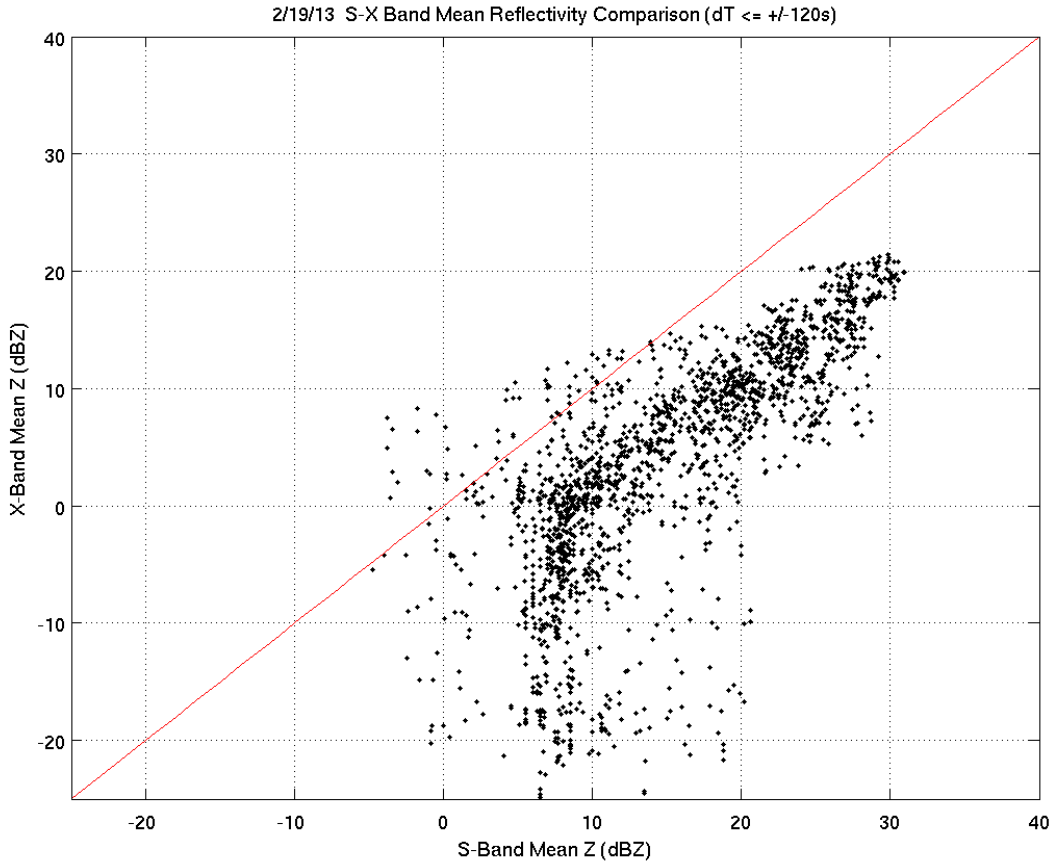

Figure D-3. Scatter plot of onboard X-band reflectivity and ground-based KBUF S-band reflectivity measured within +/- 120 seconds of the X-band measurement. These observations pertain to the flight on February 19, 2013. A +8 dB offset was used to correct the X-band data to force a match with the S-band observations, assumed to be well-calibrated (results shown in Figure 6-11).

The availability of KBUF S-band reflectivity associated with SLW was presented in Section 7.5. For each flight, the KBUF data were available for the majority of time when LWC was >0.005 g/m^3. This is somewhat expected since the flights were radar-guided and as such were biased to travel through regions with returns. A similar check for the onboard X-band radar data is presented here. On February 19, 77% (783/1015) of the five-second LWC samples >0.005 g/m^3 had coincident X-band radar data. For February 26–27 and February 28, 98% (1641/1666) and 59% (507/862) of the time the X-band radar data were coincident with significant LWC, respectively. The availability of either the X-band or S-band reflectivity was quite similar for the first two flights. However, for the last flight, X-band availability was lower.

GLOSSARY

ACARS	Aircraft Communications and Reporting System
AIRS	Alliance Icing Research Study
ARTCC	Air Route Traffic Control Center
BAIRS	Buffalo Area Icing and Radar Study
BD	Big Drops
BI	Biologicals
CASP	Canadian Atlantic Storms Program
CC	Correlation Coefficient
CCN	Cloud Condensation Nuclei
CFDE	First Canadian Freezing Drizzle Experiment Study
CIWS	Corridor Integrated Weather System
CWKR	King City Radar, Ontario, Canada
DS	Dry Snow
FAA	Federal Aviation Administration
FAR	False Alarm Rate
FIRE.ACE	Regional Experiment Arctic Cloud Experiment
FSSP	Forward Scattering Spectrometer Probe
GC	Ground Clutter
GR	Graupel
HA	Hail-Rain
HC	Hydrometeor Classification
HCA	Hydrometeor Classification Algorithm
HFP	Hexagonal Flat Plates
HR	Heavy Rain
IC	Ice Crystals
IHL	Icing Hazard Levels
ISSCP	International Satellite Cloud Climatology Project
KBUF	Buffalo, NY, NEXRAD
KCLE	Cleveland, OH, NEXRAD
KDP	Specific Differential Phase
KFWS	Fort Worth, TX, NEXRAD

KMKX	Milwaukee, WI, NEXRAD
LL	MIT Lincoln Laboratory
LWC	Liquid Water Content
MLDA	Melting Layer Detection Algorithm
MVD	Median Volume Diameter
NE	No Echo
NEXRAD	Next Generation Weather Radar
NOAA	National Oceanic and Atmospheric Administration
NRC	National Research Council of Canada
NTSB	National Transportation Safety Board
NWS	National Weather Service
OAP	Optical Array Probes
ORPG	Open Radar Product Generator
PIREP	Pilot Reports
PMS	Particle Measuring System
POD	Probability of Detection
PPI	Plan Position Indicator
QPE	Quantitative Precipitation Estimation
RA	Rain
ROC	Radar Operations Center
SLC	Supercooled Liquid Concentration
SLD	Supercooled Large Drop
SLR	Single Lens Reflex
SLW	Supercooled Liquid Water
SMZ	Smoothed Reflectivity
SNDI	Spheres, Needles, Dendrites, and Irregulars
SNR	Signal-to-Noise Ratio
UK	Unknown
VCP	Volume Coverage Pattern
WFO	NWS Weather Forecast Office
WS	Wet Snow
ZDR	Differential Reflectivity

REFERENCES

Bailey, M.P. and J. Hallett, 2009: "A comprehensive habit diagram for atmospheric ice crystals: Confirmation from the laboratory, AIRS II and other field studies," *J. Atmos. Sci*., **66**, 2888–2899.

Bechini, R., L. Baldini, and V. Chandrasekar, 2013: "Polarimetric radar observations in the ice region of precipitating clouds at C-band and X-band radar frequencies," *J. Appl. Met. Clim*., **52**, 1147–1169.

Bernstein, B.C, C.A. Wolff, and F. McDonough, 2007: "An inferred climatology of icing conditions aloft, including supercooled large drops, Part I: Canada and the Continental United States," *J. Appl. Met. Clim*., **46**, 1857–1878.

Bernstein, B.C., T.A. Omeron, F. McDonough, and M.K. Politovich, 1997: "The relationship between aircraft icing and synoptic conditions," *Weather and Forecasting*, **12**, 742–762.

Chornoboy, E.S., A.M. Matlin, and J.P. Morgan, 1994: "Automated storm tracking for terminal air traffic control," *The Lincoln Laboratory Journal*, **7**, 427–448.

Cober, S., B. Bernstein, R. Jeck, E. Hill, G. Isaac, J. Riley, and A. Shah, 2009: "Data and analysis for the development of an engineering standard for supercooled large drop conditions," DOT/FAA/AR-09/10, U.S. Department of Transportation, Final Report, March 2009.

Cober, S.G., G.A. Isaac, A.V. Korolev, and J.W. Strapp, 2001: "Assessing cloud-phase conditions," *J. Appl. Met*., **40**, 1967–1983.

Cober, S.G., G.A. Isaac, and J.W. Strapp, 2001: "Characterizations of aircraft icing environments that include supercooled large drops," *J. Appl. Met*., **40**, 1984–2002.

Evaristo, R., T. Bals-Elsholz, E. Williams, A. J. Fenn, M. Donovan, and D. Smalley, 2013: "Relationships of graupel shape to differential reflectivity: Theory and observations," *Annual Meeting, American Meteorological Society*, Austin, TX, January 2013.

FAA, 2013a: U.S. D.O.T. – FAA Library – Flight Services, Chapter 9 (FAA Weather Services) Section 2: Pilot Weather Report.

Field, P.R., R.J. Hogan, P.R.A. Brown, A.J. Illingworth, T.W. Choularton, P.H. Kaye, E. Hirst, and R. Greenaway, 2004: "Simultaneous radar and aircraft observations of mixed-phase cloud at the 100-m-scale," *Quart. J. Roy. Meteorol. Soc.,* **130**, 1877–1904.

Hallowell, R.G., M.F. Donovan, D J. Smalley, and B.J. Bennett, 2013: "Icing hazard detection with NEXRAD IHL," *36th AMS Conference on Radar Meteorology,* Breckenridge, CO, September 2013.

Hobbs, P.V., 1974: *Ice Physics*, Clarendon Press, Oxford.

Hogan, R.J., P.R. Field, A.J. Illingworth, R.J. Cotton, and T.W. Choularton, 2002: "Properties of embedded convection in warm-frontal mixed-phase cloud from aircraft and polarimetric radar data," *Q.J.R.M.S.*, **128**, 451–476.

Houghton, H.G., 1985: *Physical Meteorology*, MIT Press, Cambridge, MA.

Hubbert, J.C., "Icing Hazard Level," Final Report 2011–2012, National Center for Atmospheric Research, 10 February 2012.

Hudak, D., B. Currie, P. Rodriguez, S.G. Cober, I. Zawadzki, G.A. Isaac, and M. Wolde, 2002: "Cloud phase detection in winter stratiform clouds using polarimetric Doppler radar," *Proceedings of ERAD*, 90–94.

Kennedy, P.C. and S.A. Rutledge, 2011: "S-band dual polarization radar observations in winter storms," *J. Appl. Met. Clim.*, **50**, 844–858.

King, W.D., D.A. Parkin, and R.J. Handsworth, 1978: "A hot wire liquid water device having fully calculable response characteristics," *J. Appl. Met.*, **17**, 1809–1813.

Klingle-Wilson, D. and J.E. Evans, 2005: "Description of the Corridor Integrated Weather System (CIWS) weather products, MIT Lincoln Laboratory, Lexington, MA, Project Rep. ATC-317.

Korolev. A. and I.P. Mazin, 2003: "Supersaturation of water vapor in clouds," *J. Atmos. Sci.*, **60**, 2957–2974.

Korolev, A. and B. Sussman, 2000: "A technique for habit classification of cloud particles," *J. Atmos. Ocean. Tech.*, **17**, 1048–1057.

Korolev, A.V., J.W. Strapp, G.A. Isaac, and A.N. Nevzorov, 1998: "The Nevzorov airborne hot wire LWC-TWC probe: Principles of operation and performance characteristics," *J. Atmos. Ocean. Tech.*, **15**, 1495–1510.

Kumjian, M.R., Ryzhkov, A.V., Reeves, H.D., and Schuur, T.J., 2013: "A dual-polarization radar signature of hydrometeor refreezing in winter storms," *J. Appl. Met. Clim.*, **52**, 2549–2566.

Langmuir, I. and K.B. Blodgett, 1960: "Mathematical investigation of water droplet trajectories," *In* Suits, C.G. *(ed), Collected Works of I. Langmuir, Vol 10.* Oxford, Pergamon Press, 348–393.

Laven, P.R., 2008: "Non-circular glories and their relationship to cloud droplet size," *Appl. Optics*, **47**, H26–H30.

Nakaya, U., 1954: "Snow Crystals: Natural and Artificial," Harvard University Press, 510 pp.

Newton, D.W., 1978: “An integrated approach to the problem of aircraft icing,” *Journal of Aircraft*, **15**, 374–380.

Park, H.S., A.V. Ryzhkov, D.S. Zrnic, and K.-E. Kim, 2009: “The hydrometeor classification algorithm for the polarimetric WSR-88D: Description and application to an MCS,” *Weather and Forecasting*, **24**, 730–748.

Plummer, D.A., S. Goke, R.M. Rauber, and L. Di Girokamo, 2010: “Discrimination of mixed-phase versus ice-phase clouds using dual-polarization radar with application to detection of aircraft icing regions,” *J. Appl. Met. Clim.*, **49**, 920–936.

Ryzhkov, A., H. Reeves, T. Schuur, M. Kumjian, and D. Zrnic, 2011: “Investigation of polarimetric radar signatures in winter storms and their relation to aircraft icing and freezing rain,” *35th AMS Conference on Radar Meteorology*, Pittsburgh, PA, September 2011.

Seliga, T.A. and V.N. Bringi, 1976: “Potential use of radar differential reflectivity measurements at orthogonal polarizations for measuring precipitation,” *J. Appl. Met*., **15**, 69–76.

Sinnott, R.W., 1984: “Virtues of the Haversine,” *Sky and Telescope*, **68**, 159.

Stoelinga, M.T., Locatelli, J.T., and Woods, C.P., 2006: “The occurrence of “Irregular” ice particles in stratiform clouds,” *J. Atmos. Sci*., **64**, 2740–2750.

Thompson, E.J., S.A. Rutledge, B. Dolan, V. Chandrasekhar, and B.L. Cheong, 2014: “A dual-polarization radar hydrometeor classification algorithm for winter precipitation,” *J. Atmos. Oceanic Technol.*, **31**, 1457–1481. doi: http://dx.doi.org/10.1175/JTECH-D-13-00119.1

Williams, E., D. Smalley, M. Donovan, R. Hallowell, K. Hood, B. Bennett, E. Victoria, M. Wolde, M. Bastian, and A. Korolev, 2013: “Validation of NEXRAD radar differential reflectivity in snowstorms with airborne microphysical measurements: Evidence for hexagonal flat plate crystals,” *36th AMS Conference on Radar Meteorology*, Breckenridge, CO, September 2013.

Williams, E.R., D.J. Smalley, M.F. Donovan, R.G. Hallowell, K.T. Hood, B.J. Bennett, R. Evaristo, A. Stepanek, T. Bals-Elsholz, J. Cobb, J. Ritzman, A. Korolev, and M. Wolde, 2015: “Measurements of differential reflectivity in snowstorms and warm season stratiform systems,” *J. Appl. Met. Clim.*, in press.

Williams, E.R., D.J. Smalley, M.F. Donovan, R.G. Hallowell, K.T. Hood, B.J. Bennett, R. Evaristo, A. Stepanek, T. Bals-Elsholz, J. Cobb, and J. Ritzman, 2011: “Dual-polarized radar winter storm studies supporting development of NEXRAD-based aviation hazards products,” *35th AMS Conference on Radar Meteorology*, Pittsburgh, PA.

Wolde, M. and A. Pazmany, 2005: "NRC dual-frequency airborne radar for atmospheric research," *32nd AMS Conference on Radar Meteorology*, American Meteorological Society, Albuquerque, NM, October 2005.

Wolde, M., D. Hudak, B. Currie. S.G. Cober, P. Rodriquez, I. Zawadzki, and G.A. Isaac, 2003: "Radar signatures of winter clouds from aircraft in-situ data and ground-based radar observations," Preprints, *31st AMS Conference on Radar Meteorology*, Seattle, WA, AMS, 973–975.

Wolde, M. and G. Vali, 2001: "Polarimetric signatures from ice crystals observed at 95 GHz in winter clouds, Part I: Dependence of crystal form," *J. Atmos. Sci*., **58**, 828–841.